

*Digital Comprehensive Summaries of Uppsala Dissertations  
from the Faculty of Science and Technology 2643*

# Droplet drama – physics of emulsions

*How proteins hold it together*

ELEONORA OLSMATS



ACTA UNIVERSITATIS  
UPSALIENSIS  
2026

ISSN 1651-6214  
ISBN 978-91-513-2749-5  
urn:nbn:se:uu:diva-579847



UPPSALA  
UNIVERSITET

Dissertation presented at Uppsala University to be publicly examined in 10101, Siegbahnsalen, Ångströmlaboratoriet, Regementsvägen 10, Uppsala, Friday, 10 April 2026 at 13:15 for the degree of Doctor of Philosophy. The examination will be conducted in English. Faculty examiner: Professor Hans Tromp (NIZO & Utrecht University).

### **Abstract**

Olsmats, E. 2026. Droplet drama – physics of emulsions. How proteins hold it together. *Digital Comprehensive Summaries of Uppsala Dissertations from the Faculty of Science and Technology* 2643. 98 pp. Uppsala: Acta Universitatis Upsaliensis. ISBN 978-91-513-2749-5.

Protein-stabilized emulsions are used in many applications but their stabilization mechanisms, particularly for plant-based proteins, are only partially understood. This dissertation investigates the structural and rheological properties of emulsions stabilized with pea proteins, focused on the role of the excess present in the continuous phase. The main finding is that pea proteins contribute to the stability in two ways, both as a classical interfacial material that adsorbs to the oil-water interface, as well as being dispersed in the continuous phase where they form a hydrated fractal-like network. This network increases viscosity and induces gelation, which provides great emulsion stability across a wide range of pH, compositions and temperatures.

Systematic mapping of stable compositions revealed a previously unexplored stability region at intermediate oil concentrations (~ 10-60% v/v) and high protein concentrations (~ 5-15% w/v). Structural characterization including confocal microscopy, and X-ray and neutron scattering, revealed that most of the protein is present in the continuous phase as hydrated aggregates forming networks that extend to micrometre length scales. These networks are important for the resulting droplet size and rheological stability. The emulsions exhibit shear thinning and thixotropic behaviour, typical of colloidal systems, as well as a yield stress that restricts droplet motion and contributes to stability. The viscosity increases with protein concentration according to the Krieger Dougherty relationship when a large effective volume fraction of hydrated proteins is considered. The droplet size decreases with increases of protein concentration, oil concentration, pH and applied shear, while changes of temperature have limited effect.

Comparison with other emulsions formed with plant-based materials indicates that similar stabilization mechanisms may occur in those systems with sufficient excess biopolymer in the continuous phase. This demonstrates the broader relevance of this work, where the formation of a viscoelastic network can significantly improve emulsion stability. By introducing a new way of representing scattering data, rapid visual comparison between complex samples is simplified, which could improve efficiency in the handling of large data sets and aid automated interpretation with artificial intelligence.

*Keywords:* Pea protein, Emulsions, Scattering, SAXS, SANS, Contrast variation, Structural fingerprints, Rheology, Ternary phase map, Emulsion stability, Protein gel, Fractal network, Protein hydration, Food applications

*Eleonora Olsmats, Department of Chemistry - Ångström, Macromolecular Chemistry, Box 538, Uppsala University, SE-75121 Uppsala, Sweden.*

© Eleonora Olsmats 2026

ISSN 1651-6214

ISBN 978-91-513-2749-5

URN urn:nbn:se:uu:diva-579847 (<http://urn.kb.se/resolve?urn=urn:nbn:se:uu:diva-579847>)

*Till mamma och pappa,*



# List of Papers

This thesis is based on the following papers, which are referred to in the text by their Roman numerals.

- I. Olsmats, E. & Rennie, A. R. (2024). Understanding Stabilization of Oil-in-Water Emulsions with Pea Protein – Studies of Structure and Properties. *Langmuir*, 40(26):13386–13396.
- II. Olsmats, E., Ravindranathan, R. P., Knudsen, K. D., Kohlbrecher, J., Bonn, D. & Rennie, A. R. (2025). Emulsions stabilized by pea protein – hydration and protein distribution. *Food Hydrocolloids*, 162:110989.
- III. Olsmats, E., Rennie, A. R. & Bonn, D. (2025). What makes oil-in-water emulsions with pea protein stable? The role of excess protein in network formation and yield stress development. *Soft Matter*, 21(19): 3757–3767.
- IV. Olsmats, E., Rennie, A. R., Plomp, J., Thijs, M., Fransen, C., Duif, C. & Bouwman, W. (2026). Non-invasive multiscale characterization of protein networks and oil droplets in emulsions using spin-echo small angle neutron scattering. *Journal of Colloid and Interface Science*, 711:140071.
- V. Olsmats, E., Gouranga, M., Telli Ceccato, B., Jin, P. & Rennie, A. R. (2026). Microstructure and dynamics in protein emulsions under shear. *Submitted*.
- VI. Olsmats, E. & Rennie, A. R. (2025). From dairy to plants: Understanding their structural fingerprints with X-rays. *npj Science of Food*, 9:109.

Reprints were made with permission from the respective publishers.

## Other contributions, not included in the thesis

- I. Olsmats, E. & Rennie, A. R. (2024). Pea protein [*Pisum sativum*] as stabilizer for oil/water emulsions. *Advances in Colloid & Interface Science*, 326:103123.
- II. Ravindranathan, R. P., Olsmats, E., Telli Ceccato, B., Knaapila, M., Rennie, A. R., Fossum, J. O. & Knudsen, K. D. (2025). Pickering emulsions stabilized with  $\beta$ -lactoglobulin nanoparticles studied by small angle X-ray scattering: stability, aging and temperature effects. *Soft Matter*, 21(33):6536–6549.

# My contributions to the papers in the thesis

- I. Conceptualization, Data curation, Formal analysis, Investigation, Methodology, Writing – original draft, Writing – review & editing
- II. Data curation, Formal analysis, Investigation, Methodology, Writing – original draft, Writing – review & editing
- III. Conceptualization, Data curation, Investigation, Writing – original draft, Writing – review & editing
- IV. Conceptualization, Data curation, Formal analysis, Investigation, Visualization, Writing – original draft, Writing – review & editing
- V. Conceptualization, Data curation, Formal analysis, Investigation, Visualization, Writing – original draft, Writing – review & editing
- VI. Conceptualization, Data curation, Formal analysis, Investigation, Methodology, Visualization, Writing – original draft, Writing – review & editing

Reprints were made with permission from the respective publishers.



# Contents

1	Background.....	17
1.1	Introduction to emulsions.....	17
1.1.1	Emulsion preparation.....	19
1.1.2	Emulsifiers as stabilizing materials .....	20
1.1.3	Stabilization mechanisms .....	21
1.1.4	Destabilization mechanisms .....	21
1.2	Pea Proteins.....	22
1.2.1	Protein structures .....	22
1.2.2	Composition of pea proteins .....	23
1.2.3	Protein extraction methods .....	24
1.2.4	Materials used in this study .....	24
2	Scope of this thesis .....	25
3	Techniques to assess emulsion stability, structure and rheological properties .....	26
3.1	Physical stability during storage.....	26
3.1.1	Dynamic/Static Light Scattering (DLS/SLS) .....	28
3.1.2	X-ray Photon Correlation Spectroscopy (XPCS) .....	30
3.1.3	Zeta potential .....	31
3.1.4	Optical Microscopy .....	33
3.1.5	Confocal Laser Scanning Microscopy (CLSM) .....	33
3.2	Scattering techniques to evaluate emulsion structure.....	35
3.2.1	Ultra-Small/Small/Wide Angle X-ray Scattering (USAXS/SAXS/WAXS) .....	36
3.2.2	Ultra-Small/Small Angle Neutron Scattering (USANS/SANS) .....	39
3.2.3	Spin Echo Small Angle Neutron Scattering (SESANS) .....	40
3.2.4	Model Fitting .....	41
3.3	Rheology .....	47
3.3.1	Shear rate sweep .....	49
3.3.2	Constant shear stress.....	51
3.3.3	Strain amplitude sweep.....	52
3.3.4	Frequency sweep .....	53
3.3.5	Low strain amplitude and frequency .....	53
3.4	Techniques to assess thermal stability.....	53

3.5 Summary of challenges and opportunities in evaluating emulsion stability .....	54
3.6 Summary of challenges and opportunities in assessing emulsion structure .....	56
3.7 Summary of challenges and opportunities in assessing emulsion rheology.....	57
4. Identification of stable emulsion compositions .....	60
4.1 Mapping stability regions in pea protein stabilized emulsions .....	60
4.2 Newly identified stable compositions .....	62
4.3 Limits of interfacial coverage stabilization model .....	63
5. Distribution and network formation of proteins in emulsions .....	64
5.1 Protein location at neutral pH.....	64
5.2 Proteins form networks in the continuous phase .....	65
5.3 Effect of pH and buffer salt on protein aggregation.....	68
5.4 Temperature effects on proteins .....	69
6. Physical properties with excess protein in the continuous phase.....	71
6.1 Rheological consequences of gelation .....	71
6.2 Gelation is affected by high shear .....	72
6.3 A favourable emulsion composition.....	73
6.4 Dynamic constraints by the protein network.....	74
7. Generalization of stabilization mechanisms in plant-based emulsions.....	75
8. Data representation and comparative analysis using colour maps.....	78
9. Summary and conclusions in one paragraph.....	82
10. Populärvetenskaplig sammanfattning .....	83
11. Popular scientific summary.....	87
12. Acknowledgements.....	90
References.....	92
Appendix A.....	97

# Abbreviations

4-DASPI	<i>trans</i> -4[4-(dimethylamino)styryl]-1-methyl-pyridinium iodide
AI	Artificial Intelligence
ANSTO	Australian Nuclear Science and Technology Organisation
CI	Creaming Index
CI*	Coalescence Index
CLSM	Confocal Laser Scanning Microscopy
DLS	Dynamic Light Scattering
DSC	Differential Scanning Calorimeter
EDL	Electrical Double Layer
EA	Emulsion Activity
EC	Emulsion Capacity
ES	Emulsion Stability
ESRF	European Synchrotron Radiation Facility
FI	Flocculation Index
IEP	Isoelectric Point
KWW	Kohlrausch-Williams-Watts
LVR	Linear Viscoelastic Region
PDI	Polydispersity Index
PSI	Paul Scherrer Institute
SANS	Small Angle Neutron Scattering
SAXS	Small Angle X-ray Scattering
SDS	Sodium Dodecyl Sulphate
SESANS	Spin-Echo Small Angle Neutron Scattering
SLD	Scattering Length Density
TGA	Thermogravimetric Analysis
TSI	Turbiscan Stability Index
USANS	Ultra-Small Angle Neutron Scattering
USAXS	Ultra-Small Angle X-ray Scattering
WAXS	Wide Angle X-ray Scattering
XPCS	X-ray Photon Correlation Spectroscopy



# Equation variables and constants with SI derived units<sup>a</sup>

$\alpha$ [-]	Distribution of relaxation times
$\beta$ [-]	Coherence of the beam
$\Gamma(x)$ [-]	Gamma function
$\gamma$ [-]	Shear strain
$\dot{\gamma}$ [ $s^{-1}$ ]	Shear rate (or strain rate)
$\delta$ [m]	Spin echo length
$\delta_a$ [rad]	Phase angle
$\Delta\rho$ [ $m^{-2}$ ]	SLD difference between dispersed and continuous phase
$\Delta\rho_{cs}$ [ $m^{-2}$ ]	SLD difference between droplet core and shell
$\Delta\rho_{sm}$ [ $m^{-2}$ ]	SLD difference between droplet shell and continuous phase
$\varepsilon$ [-]	Dielectric constant
$\zeta$ [V]	Zeta potential
$\eta$ [ $kg\ m^{-1}\ s^{-1}$ ]	Viscosity
$\eta_c$ [ $kg\ m^{-1}\ s^{-1}$ ]	Viscosity of the continuous phase
$[\eta]$ [ $m^3\ kg^{-1}$ ]	Intrinsic viscosity
$\theta$ [rad]	Scattering angle
$\kappa$ [ $m^{-1}$ ]	Inverse Debye length
$\lambda$ [m]	Wavelength
$\xi$ [m]	Characteristic length scale/correlation length/cluster size
$\pi$ [-]	Pi
$\sigma$ [ $N\ m^{-1}$ ]	Shear stress
$\sigma_I$ [ $N\ m^{-1}$ ]	Stress from interfacial tension
$\sigma_T$ [ $N\ m^{-1}$ ]	Surface tension
$\sigma_V$ [ $N\ m^{-1}$ ]	Viscous stress
$\sigma_y$ [ $N\ m^{-1}$ ]	Yield stress
$\tau$ [s]	Time between images
$\tau_a$ [s]	Apparent relaxation time
$\tau_c$ [s]	Characteristic relaxation time
$\phi$ [-]	Volume fraction of dispersed phases/all scatterers
$\phi_a$ [rad]	Azimuthal angle
$\phi_m$ [-]	Maximum packing fraction

---

<sup>a</sup> Reference [1]

$\omega$ [rad s <sup>-1</sup> ]	Angular frequency
$A$ [m <sup>2</sup> ]	Plate area
$a$ [rad]	Angle between the ellipsoid axis and $\vec{Q}$
$a_1$ [s <sup>-1</sup> ]	First cumulant (mean decay rate)
$a_2$ [s <sup>-2</sup> ]	Second cumulant coefficient
Ca [-]	Capillary number
CI [-]	Creaming index
CI* [-]	Coalescence index
$D$ [m <sup>d-1</sup> sr <sup>-1</sup> ]	Porod law scale factor
$D_f$ [-]	Mass fractal dimension
$D_R$ [s <sup>-1</sup> ]	Rotational diffusion coefficient
$D_T$ [m <sup>2</sup> s <sup>-1</sup> ]	Translational diffusion coefficient
$d$ [m]	Real space distances
$d_e$ [-]	Porod exponent
$d_p$ [m]	Plate movement distance
EA [-]	Emulsion activity
EC [-]	Emulsion capacity
ES [-]	Emulsion stability
$F$ [kg m s <sup>-2</sup> ]	Force on plate
FI [-]	Flocculation index
$f(\kappa r_p)$ [-]	Henry's function
$G$ [m <sup>-1</sup> sr <sup>-1</sup> ]	Guinier scale factor
$G_E$ [J]	Gibbs' free energy
$G'$ [N m <sup>-1</sup> ]	Storage modulus
$G''$ [N m <sup>-1</sup> ]	Loss modulus
$G(\delta)$ [-]	Correlation as a function of spin-echo length in SESANS
$g_2(Q, \tau)$ [-]	Correlation function in XPCS
$I$ [m <sup>-1</sup> sr <sup>-1</sup> ]	Intensity
$I_b$ [m <sup>-1</sup> sr <sup>-1</sup> ]	Source intensity background
$I_{CSS}$ [m <sup>-1</sup> sr <sup>-1</sup> ]	Intensity given by the core shell sphere model
$I_E$ [m <sup>-1</sup> sr <sup>-1</sup> ]	Intensity given by the ellipsoid model
$I_F$ [m <sup>-1</sup> sr <sup>-1</sup> ]	Intensity given by the mass fractal model
$I_{GP}$ [m <sup>-1</sup> sr <sup>-1</sup> ]	Intensity given by the Guinier-Porod model
$I_S$ [m <sup>-1</sup> sr <sup>-1</sup> ]	Intensity given by the sphere model
$K$ [-]	Consistency index
$k_B$ [kg m <sup>2</sup> s <sup>-2</sup> K <sup>-1</sup> ]	Boltzmann constant
$H_E$ [m]	Height of upper emulsion layer in a separated emulsion
$H_S$ [m]	Height of lower layer in a separated emulsion
$H_T$ [m]	Total height of emulsions
$h$ [m]	Plate separation distance
$n$ [-]	Flow index
$p$ [-]	Decay rate (d(logI)/d(logQ))
$P(\delta)$ [-]	Polarization as a function of spin-echo length in SESANS

$P(Q)$ [-]	Form factor
PDI [-]	Polydispersity index
$Q$ [ $\text{m}^{-1}$ ]	Momentum transfer or scattering vector
$Q_1$ [ $\text{m}^{-1}$ ]	Transition in $Q$ between the Guinier and Porod regions
$R$ [m]	Radius of individual scatterer
$R_c$ [m]	Radius of droplet core
$R_e$ [m]	Equatorial radius
$R_g$ [m]	Radius of gyration
$R_H$ [m]	Hydrodynamic radius
$R_p$ [m]	Polar radius
$R_S$ [m]	Radii of droplet shells
$r_p$ [m]	Particle radius
$s$ [ $^{-b}$ ]	Sample standard deviation
$S(Q)$ [-]	Structure factor
$T$ [K]	Temperature
$t$ [s]	Time
$t_s$ [m]	Sample thickness
$U_E$ [ $\text{m}^2 \text{V}^{-1} \text{s}^{-1}$ ]	Electrophoretic mobility
$V$ [ $\text{m}^3$ ]	Volume of individual scatterer
$V_A$ [ $\text{m}^3$ ]	Volume of aqueous phase after homogenization
$V_B$ [ $\text{m}^3$ ]	Volume of aqueous phase before homogenization
$V_c$ [ $\text{m}^3$ ]	Volume of droplet cores
$V_S$ [ $\text{m}^3$ ]	Volume of droplet shells
$v$ [ $\text{m s}^{-1}$ ]	Linear velocity
$\bar{x}$ [ $^{-c}$ ]	Sample mean
$Z$ [-]	Atomic number

---

<sup>b</sup> Unit is the same as for the sample mean data

<sup>c</sup> Unit is dependent on the measured property



# 1 Background

This thesis includes a short introduction of various elementary concepts including description of emulsion systems and identification of a good emulsifier. Various ways to extract stabilizer materials, prepare emulsions and key parameters to improve emulsion stability are discussed. This is followed by a description of methods and instrument techniques used to investigate emulsion stability, microstructure and rheological properties. Challenges and how these methodologies complement each other are presented. Scientific progress throughout papers I to V are discussed in chapters 4 to 8, followed by an overall discussion (chapter 9) summarizing the complementary findings from these.

Paper I is devoted to determining a range of stable emulsion compositions with pea proteins, and gives examples of general structural and rheological properties of such emulsions. Papers II and IV investigate the emulsion structure in more detail. Paper II focuses on slightly smaller structures such as the location and folding of the proteins, and paper IV concentrates on larger structures of interacting proteins and oil droplets. Paper III gives an explanation for the excellent emulsion stability by looking deeper at the rheological behaviour. Paper V extends the rheological interpretation and links the structural changes to rheological behaviour when shear is applied. Paper VI compares different common plant-stabilized emulsions regarding structure and composition.

## 1.1 Introduction to emulsions

Oil and water do not spontaneously mix. However, under specific conditions, they can be combined into stable materials, e.g., emulsions [2]. Everyday examples include a perfectly smooth and creamy texture of an ice cream on a hot sunny day (Figure 1) or the preparation of a light and creamy mayonnaise for a summer barbecue. The success of these materials depends on the combination of two immiscible liquids. Emulsions are materials that are so familiar in everyday life, but still complex in a scientific perspective. The complexity is often first encountered when an emulsion becomes unstable, such as if a mayonnaise separates into oil and water layers, or if an ice-cream becomes coarse and icy. Social media offers various tips on how to prevent or save

these by adding extra egg yolk or adjusting the freezing temperature. While these tips often work in practise, few people are aware of the physical mechanisms governing the results (see, for example, [3]). It is therefore not only relevant from a scientific perspective to dive into this dissertation, but perhaps it can give you some practical benefits for everyday cooking. Although ice-cream is a more complex system that also contains ice crystals and air bubbles, emulsion stability remains a central factor for the creaminess and texture. This dissertation does not focus specifically on low-temperature effects in emulsions, but ice-cream is mentioned as a conceptual example of where emulsion stability and structure are important.



Figure 1. a) Ice-cream on a hot and sunny day is always a good idea. But only with the perfect creaminess and melting rate is the experience optimal. b) Busy doing business. Then it is good that someone else thought about the physics of your food.

Emulsions are metastable dispersions of two immiscible liquids, where one phase is dispersed as droplets within the other continuous phase (Figure 2a). The most common examples of liquids are oil and water, which can form oil-in-water (O/W) emulsions such as milk and mayonnaise, and water-in-oil (W/O) emulsions such as butter and margarine. In addition to the food industry, emulsions are widely used in other fields such as in pharmaceuticals for drug delivery with controlled release, in cosmetics to obtain products with desired sensory properties, in fuels such as biodiesel and in paints or other protective coatings. Emulsions are considered metastable because when droplets are formed, the total interfacial area between the two liquids increases, and hence the system is thermodynamically unstable (it is not in the lowest energy state). Therefore, emulsion stability depends on kinetic stabilization. Although emulsion formation is not the most stable form, high activation energy barriers make their destabilization slow on relevant time scales (consumption/storage). A diagram of the changes in Gibbs' free energy,  $\Delta G_E$ , of a stable and phase separated emulsion is shown in Figure 2e. The system is

thermodynamically stable in the phase-separated state, however with the addition of different emulsifiers, the energy barrier to destabilize the emulsion can be made sufficiently high to keep the emulsion stable for relevant times. For reference, in a 10 ml emulsion with 50% oil and droplets of 1  $\mu\text{m}$  radii, the total surface area is 15  $\text{m}^2$ . For a separated emulsion in two layers, this surface area would depend on the shape of the container, but for the simple case of a square block, this area would be only 0.0005  $\text{m}^2$ . It is therefore easy to understand that without applied shear to force the emulsion into a state of kinetic stability, the oil and water will spontaneously separate into two layers.

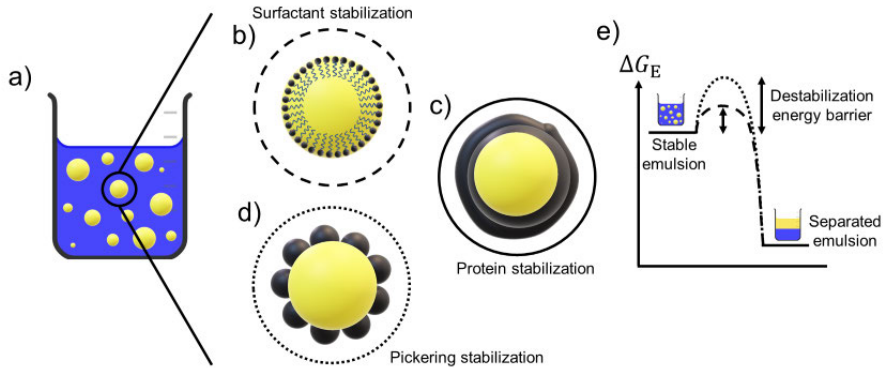


Figure 2. a) Schematic of an emulsion with oil droplets (yellow) dispersed in a continuous aqueous phase (blue). b) Surfactant stabilized oil droplet. The hydrophilic head is in the aqueous phase and the hydrophobic tail is in the oil phase. c) Protein stabilized oil droplet. Proteins adsorb to the surface and form a viscoelastic layer. d) Particle (Pickering) stabilized oil droplet. The larger volume of a single particle compared to a surfactant gives a very strong adsorption and high energy is required for destabilization. e) Energy diagram of an emulsion. Emulsions are thermodynamically unstable because the dispersed state has a higher free energy than the separated state, however, they can be kinetically stable due to an energy barrier that hinders droplet coalescence.

### 1.1.1 Emulsion preparation

Addition of mechanical energy is required to form droplets of the dispersed phase. This is typically done with high shear or high-pressure processes such as rotor-stator homogenization or blending, or high-pressure homogenization. The stress that is applied needs to be greater than the stress arising from the interfacial tension between the two materials. The size of the droplets formed is dependent on for example the applied energy, the processing conditions and the individual properties of the two liquids such as viscosity and density. Samples in this study were prepared with high shear homogenization. For the study in paper I, the emulsions prepared with a homogenizer was compared to ones prepared in a food blender to resemble the conditions in the preparation

of food materials. More details of the preparation techniques are provided in the respective papers.

### 1.1.2 Emulsifiers as stabilizing materials

Since emulsions are thermodynamically unstable, additional surface-active materials are required to reduce the interfacial tension between the two liquids and to limit droplet coalescence after breakup. Such materials are often referred to as emulsifiers and they preferably adsorb to oil-water interfaces. Various materials can act as emulsifiers, such as (low molecular weight) surfactants [4, 5] (Figure 2b), proteins [6, 7] (Figure 2c), polysaccharides [8, 9] and solid (Pickering) particles [10, 11, 12] (Figure 2d). While for example proteins stabilize emulsions through their amphiphilic nature that makes them suitable to adsorb at an oil-water interface, particle stabilized emulsions rely on the high detachment energy associated with the adsorption of large particles at the surface. The stabilization mechanisms are very different and hence properties such as detachment energy, adsorption angles, overall stability and droplet size will vary depending on the emulsifier. The energy diagram in Figure 2e shows how the destabilization energy, for example, is higher for Pickering emulsions than for conventional surfactant stabilized emulsions due to their larger particle size.

Emulsions are interesting and complex types of materials considering the broad range of length scales involved in the structure. From millimetre-scale visual properties as a homogeneous material (Figure 3a), to micrometre-sized droplets and nanometres-sized interfacial layers. A micrograph of typical emulsion droplets dispersed in a continuous phase is shown in Figure 3b. The exact structure of the material is dependent on various factors but the choice of emulsifier is indeed an important one for the resulting properties in terms of droplet size, rheological behaviour and stability.

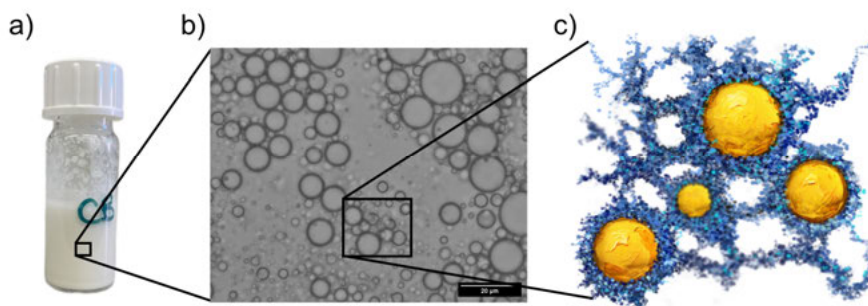


Figure 3. a) Visual appearance (macroscale) of an emulsion as prepared in the laboratory. b) Optical micrograph (microscale) of an emulsion. Scale bar is 20  $\mu\text{m}$ . c) Graphical representation of emulsion structure including oil droplets (yellow) and protein networks (blue) in a continuous water phase (white).

### 1.1.3 Stabilization mechanisms

Kinetic emulsion stability can be obtained by several different phenomena. These can broadly be divided into interfacial mechanisms acting at droplet interfaces, and continuous phase mechanisms depending on the properties of the continuous phase. Examples of different interfacial mechanisms include steric stabilization, where contact between neighbouring droplets is restricted by adsorbed interfacial layers, creating a physical barrier that prevents droplet coalescence, and electrostatic stabilization, where charged droplet surfaces lead to repulsion that prevents droplet coalescence.

In addition to these interfacial effects, properties of the continuous phase may also be important for emulsion stability. Viscosity, elasticity and network formation in the continuous phase affect the mobility of droplets and hence the stability. These effects have been less studied than pure interfacial effects, however they are relevant particularly for many biopolymers or mixed stabilizer materials, where a significant fraction of the materials are in the continuous phase rather than being adsorbed at interfaces [13].

### 1.1.4 Destabilization mechanisms

The kinetic stability is only temporary and emulsions destabilize over time. There are several mechanisms for destabilization, plotted in Figure 4, including:

- Coalescence – droplets merge and this process is irreversible
- Creaming – if the dispersed phase has a lower density than the continuous phase, the droplets tend to concentrate at the top
- Flocculation – droplets aggregate but do not merge and this process is reversible
- Ostwald ripening – smaller droplets become smaller and larger droplets become larger
- Phase inversion – the dispersed phase becomes the continuous phase and the continuous phase becomes the dispersed phase
- Sedimentation - if the dispersed phase has a higher density than the continuous phase, the droplets tend to concentrate at the bottom

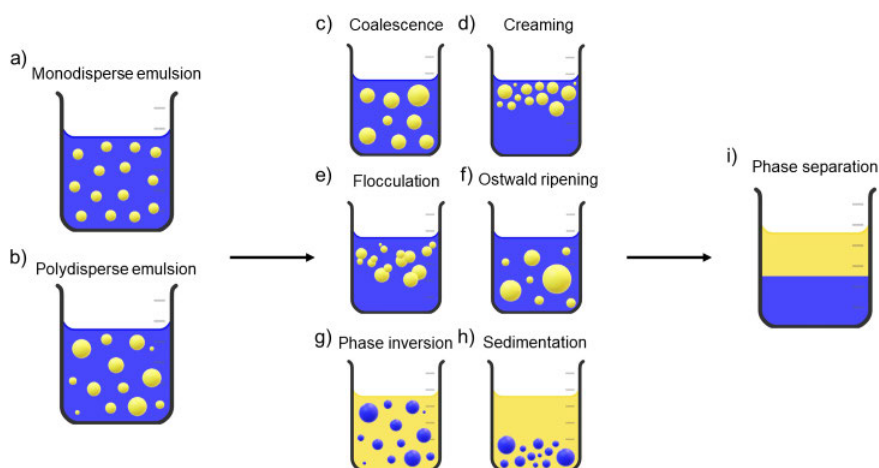


Figure 4. Graphical representations of a) monodisperse and b) polydisperse emulsions. Mechanisms of emulsion destabilization, including c) coalescence, d) creaming, e) flocculation, f) Ostwald ripening, g) phase inversion and h) sedimentation, leading to i) complete phase separation.

## 1.2 Pea Proteins

Proteins as emulsifiers are well studied due to their amphiphilic nature which makes them favourably adsorbing at oil-water interfaces. In food systems, the proteins are often complex mixtures of components as isolated fractions are difficult to obtain. The structure and functionality depend on factors such as the molecular composition and processing. Proteins from peas are examples of plant-based materials that are identified as promising emulsifiers [14], however the exact mechanisms for stability and optimal compositions have not been clearly identified. Peas have many advantages considering their good nutritional and environmentally sustainable properties [15]. In contrast to soy, they are generally considered less allergenic, and compared to animal-derived materials such as egg or dairy, they are easy to grow globally and require less resources. Pea proteins are mixtures of various components and this is one motivation for the use of this material. To advance understanding within food science, it is important to study not only simplified model materials or isolated fractions but complicated mixtures that are realistic for industrial applications.

### 1.2.1 Protein structures

Proteins are composed of amino acids held together by peptide bonds. Amino acids contain two functional groups including an amino group ( $-\text{NH}_2$ ) and a carboxyl group ( $-\text{COOH}$ ). There are 20 main naturally occurring amino acids and the sequence of these is called the primary structure [16]. The string of

amino acids folds into secondary structures such as  $\alpha$ -helices and  $\beta$ -sheets. These structures are further folded into tertiary structures describing the three-dimensional conformation of the proteins and finally composed into quaternary structures of multiple molecules (Figure 5).

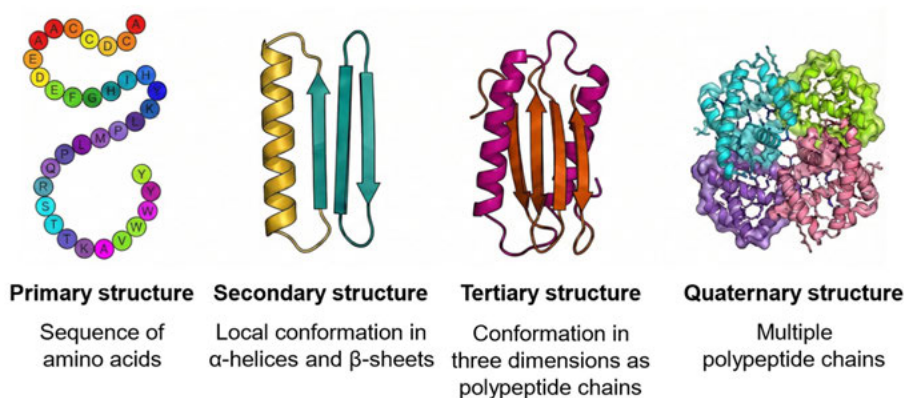


Figure 5. Graphical representation of the hierarchal structure of proteins from individual amino acids to complex structures of multiple polypeptide chains. This is an AI-generated image.

The native conformational state of proteins is typically in compact forms due to intramolecular interactions such as hydrogen bonding, electrostatic interactions and hydrophobic effects. However, external factors such as high temperatures, low pH and high ionic strengths generally denatures the protein. This is a process of unfolding, resulting in exposure of hydrophobic parts that were previously covered inside the native protein structure. Generally, denaturation causes aggregation or network formation of proteins. The degree of denaturation is important for interfacial properties as for example partly unfolded proteins could adsorb more strongly to oil-water interfaces.

### 1.2.2 Composition of pea proteins

Peas consist of 13.7-38.3% protein and 55-68% starch [17]. The variation arises due to different growing conditions, varieties and environments. The protein content of the commercial pea protein isolate used for the work in this thesis was 83% w/w [18]. The lipid, fibre and salt content were reported as 6.8, 5.3 and 2.9% w/w, respectively. The pea proteins are mainly composed on globulins (65-80%) and albumins (10-20%). The globulins are usually classified into 7S globulins which are mainly vicilin and convicilin and 11S globulins which are mainly legumin. This classification is based on the sedimentation coefficient which depends on the size, density and shape of the protein and is given in terms of Svedberg units, S [19]. My review article [17] provides a table of amino acid compositions for two different examples of pea

protein isolates. The differences in composition arise mainly from variety, extraction and processing.

### 1.2.3 Protein extraction methods

To obtain the concentrated protein isolate, the most common approach is to use alkaline extraction followed by isoelectric precipitation [20, 21]. In short, proteins are dispersed at alkaline conditions (high pH), followed by a shift in pH to their isoelectric point (pH ~ 4-5). Due to the low protein solubility at this condition, they are precipitated and can be collected.

Another approach to extract proteins is by precipitation as micelles [20, 21]. The principle is similar, however instead of varying pH, the ionic strength is controlled to induce protein aggregation. This has some similarity to salt extraction followed by dialysis that is also sometimes used, and involves aggregating proteins at sufficiently high salt concentrations to separate proteins from small salt molecules by a semi-permeable membrane [20, 21]. To avoid changes in pH and ionic strength, which may affect the conformation of the protein, dry air classification [22] is sometimes used to isolate proteins in a more careful way. This approach limits chemical modification by using air flow to separate fine protein rich fractions and coarser starch rich fractions of grounded pea flour.

### 1.2.4 Materials used in this study

The materials used in this work were chosen to be relevant for food applications. A commercial pea protein isolate was selected to represent a realistic ingredient for industrial applications rather than a highly purified protein material. The oil was a commercially available rapeseed oil, widely used in Sweden and known to contain healthy components [23, 24]. A citrate buffer [25], composed of citric acid and sodium citrate which are both suitable for food applications, was used to control pH.

For the work in paper VI, various different commercially available plant-based emulsions were compared, including samples with almond, coconut, fava bean, linseed, oat, pea, rice and soy, as well as dairy materials as references. Details about the composition and ingredient list for these emulsions are given in Table 2 and Table S3 of paper VI.

## 2 Scope of this thesis

The work in this thesis aims to relate protein concentration and location to emulsion stability, droplet size and rheological properties. Through advanced scattering techniques using X-ray and neutron beams, the study provides insights into protein behaviour at interfaces and in the continuous phase of emulsions. With simplified ways for data visualization, these techniques are opened to a broader audience and this work aims to bridge the gap between the food science community and scattering experts.

Explanations and discussions of experimental techniques are described in chapter 3. The chapter is divided by techniques that mainly assess emulsion stability (section 3.1), structure (section 3.2), rheological behaviour (section 3.3) and thermal stability (section 3.4). Sections 3.5, 3.6 & 3.7 discuss some of the challenges and my own observations related to each class of techniques.

Chapters 4 to 8 describe the evolution of understanding of emulsion structure and properties from papers I to VI. These include pea protein stabilized emulsions as a detailed case study and the findings are then expanded to other plant-based emulsifier materials.

## 3 Techniques to assess emulsion stability, structure and rheological properties

This chapter provides a summary of different techniques to assess emulsion stability, structure and rheological properties. In addition to describing the methods, the chapter also includes motivation and what type of information each technique provides, as well as some critical discussion of strengths, challenges and my own observations related to the choice of techniques. For more details about the specific instruments and exact experimental procedures used in each paper, readers are referred to the methods sections in the individual articles.

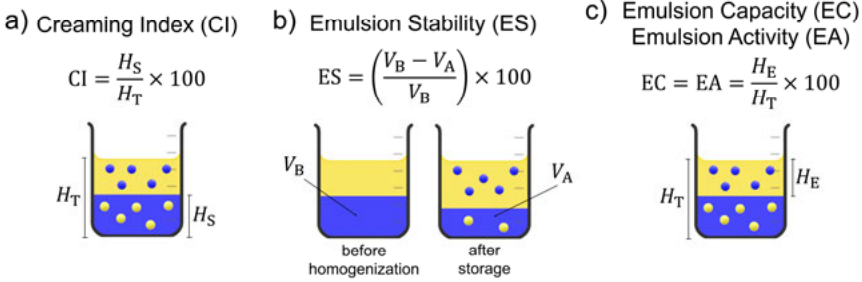
### 3.1 Physical stability during storage

There are many techniques that may be used to evaluate the physical stability of emulsions. Common approaches are to assess changes in appearance (macrolevel) and droplet size (microlevel) that occur with time. The extensive review article [17] discusses in detail the measurement concepts, potential challenges and user frequency some of the most common techniques used for this purpose.

Visual appearance of phase separation (macrolevel) is used by consumers on a daily basis in assessing for example appeal and goodness of food products, but is also frequently reported in the scientific literature. For example, macroscopic images were provided in 23% of the articles on pea protein stabilized emulsions included in the literature review [17]. This method involves monitoring the emulsions over time to detect phase separation, creaming and sedimentation. As a way of quantifying the stability, several indices are derived directly from such observations. The most frequently reported creaming index (CI) (Figure 6a) refers to the ratio between the separated lower layer to that of the total volume and can easily be measured in a straight-wall container. Emulsion stability (ES) (Figure 6b) describes similar properties and is defined as the ratio between the difference in aqueous phase volume from before homogenization to after storage, to the aqueous phase volume before homogenization. While these indices are widely used in literature, the visual observations of stability in this work have not been parametrized in this way.

If appearance is mainly relevant to stability and customer visual perception, droplet size (microlevel) affects properties such as stability, mouthfeel and creaminess. It can be determined based on light scattering experiments, and stability can be monitored by comparing changes in droplet size over time. Techniques like dynamic light scattering (DLS), static light scattering (SLS) and confocal laser scanning microscopy (CLSM) are commonly used to observe changes in structure and distribution of droplets.

**Macroscopic indices related to appearance obtained from visual observation**



**Microscopic indices related to droplet size obtained from light scattering**

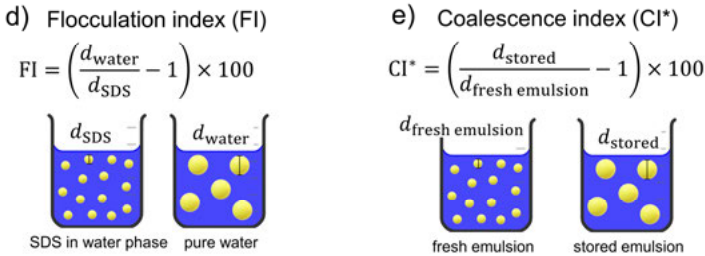


Figure 6. Various indices to quantify physical emulsion stability, including a) creaming index, b) emulsion stability, c) emulsion capacity/activity, d) flocculation index and e) coalescence index.

Assessing physical stability during storage is one aspect, however, a useful metric to predict the stability of samples is the zeta potential. In emulsions, the zeta potential represents the electrical potential difference between the droplet surface and the surrounding medium. Therefore, a higher absolute zeta potential (either positive or negative) typically indicates that droplets repel each other which corresponds to greater emulsion stability. This property is commonly measured using electrophoretic light scattering instruments.

A challenge in the attempt to evaluate storage stability is the time limitation. Globalization, long transports and long shelf-life consumer expectations put requirements on long-time storage stability, however with time limitations there is sometimes need for prediction of the long-term behaviour particularly

regarding phase separation. One approach commonly used in literature is to perform accelerated stability tests by centrifugation as a quick way to simulate long-term storage under gravitational effects. A frequently reported index to quantify the volume of the emulsified phase relative to the total sample is emulsion capacity (EC) which is sometimes also referred to as emulsion activity (EA) (Figure 6c). This measure is similar to the CI of non-centrifuged samples. This quantity was not directly measured in the present work. In the following subsections, the main techniques that have been used to gain information about emulsion stability in this dissertation will be described in more detail.

### 3.1.1 Dynamic/Static Light Scattering (DLS/SLS)

DLS, schematically seen in Figure 7a, is widely used to measure temporal correlations in the intensity of scattered light. These correlations arise from interference of coherently scattered light due to particle motion and refractive index differences in dispersions such as emulsions [26, 27]. Objects, such as droplets and particles, undergo translational Brownian motion, and therefore, the scattered light fluctuates over time (Figure 7c). Other fluctuations in scattered intensity, such as variable source intensity and mechanical vibrations of the instrument should not be measured but may cause some problems in such measurements. The rate of the fluctuations from particle motion is directly used to obtain intensity autocorrelation functions (Figure 7d). The decay rate of this function determines the translational diffusion coefficient,  $D_T$ , which is related to the hydrodynamic radius  $R_H$ , (Figure 7e) according to the Stokes-Einstein relation as:

$$R_H = \frac{k_B T}{6\pi\eta_c D_T}$$

where  $k_B$  is the Boltzmann constant,  $T$  is the temperature, and  $\eta_c$  is the viscosity of the surrounding medium (continuous phase) [28]. The hydrodynamic radius represents the effective particle radius, including hydrated layers and polymer coatings. The measurements in this thesis are performed in close to back scattering geometry ( $\theta = 173^\circ$ ) to reduce the path length and limit the effect of multiple scattering which would occur when emulsions are highly concentrated and photons are scattered more than once before reaching the detector [29, 30].

By comparing the change in droplet size during storage, DLS can be useful to monitor emulsion stability. However, a challenge with measuring samples such as emulsions is the uncertainty in the viscosity to use in the Stokes-Einstein relation. The effective viscosity experienced by the droplets on different length scales may be substantially different from the bulk viscosity. A conventional approach in these types of measurements is to dilute the emulsions.

This action needs to be performed with care, as droplet or particle size and stability in many cases are strongly dependent on emulsion composition. Another factor in the measure of non-rigid objects such as droplets, is that in addition to Brownian motion, other fluctuations such as variation in shape and membrane motion, may give rise to more complicated correlations in the scattered photons.

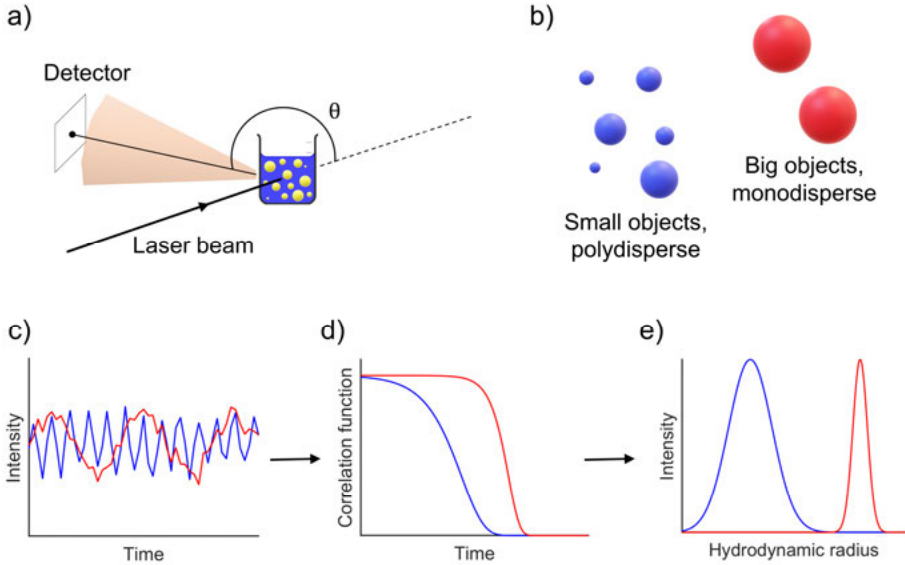


Figure 7. a) Schematic setup of the DLS technique. b) Illustration of small and polydisperse objects (in blue), and big and monodisperse objects (in red). c) Intensity fluctuations recorded on the detector for the different sized objects. Smaller objects moves faster and the intensity fluctuations have a higher frequency (blue line). d) Correlation function for the two populations. The point at which the decay starts is earlier for smaller objects (blue line), but the gradient is steeper for monodisperse populations (red line). e) Hydrodynamic diameters obtained for the two populations, where higher polydispersity is reflected by a broader distribution (blue line).

To evaluate the uniformity of droplet sizes, the polydispersity index (PDI) is a dimensionless measure of the breadth of the size distribution. This is defined by the ratios in a cumulant fit as:

$$PDI = \frac{2a_2}{a_1^2} = \frac{s^2}{\bar{x}^2}$$

where  $a_1$  is the first cumulant describing the mean decay rate,  $a_2$  is the second cumulant coefficient,  $\bar{x}$  is the mean and  $s$  is the standard deviation [31]. A value close to one corresponds to a highly polydisperse sample, which may in most cases suggest that the presence of larger droplets will cause phase

separation. For a narrow size distribution, PDI is close to zero. It is worth to mention that this is only meaningful for distributions with a single peak.

To quantify the change in droplet size over time, several indices related to different destabilization mechanisms have been introduced. For example, coalescence and flocculation of emulsions are often reported quantitatively as a flocculation index (FI) (Figure 6d) or a coalescence index (CI\*<sup>d</sup>) (Figure 6e). The FI compares the aggregated droplet size in emulsions made with pure water and individual droplets in an emulsion prepared with small amounts (usually around 1%) of sodium dodecyl sulphate (SDS), as SDS is expected to be an efficient emulsifier. The CI\* compares the droplet size in fresh and stored emulsions.

DLS can be used to investigate objects in the nanometre to sub-micrometre size range. However, as with all scattering techniques, the signal is strongly weighted toward larger objects. Rather than measuring at one angle in back-scattering mode, SLS measures the angular dependence of the scattered intensity and is typically used for larger objects. For small objects, the angular variation of the scattering is small and requires very precise measurements of relative intensity at different angles.

Another indirect technique to measure droplet size, similar to conventional light scattering techniques, is ultraviolet-visible spectrophotometry. It measures the absorbance of light, which depend on the particle size, to track changes in the scattering from droplets over time. The result can then be expressed in an emulsion stability index (ESI) that is dependent on the absorbance, cuvette path length and storage time. Another method that focuses on assessing the inhomogeneity of samples rather than changes with time, is the Turbiscan stability index (TSI) [32]. This index is obtained from a Turbiscan instrument and compares scattering from different regions of a sample to look for effects of creaming (Figure 4d) or sedimentation (Figure 4h).

### 3.1.2 X-ray Photon Correlation Spectroscopy (XPCS)

X-ray Photon Correlation Spectroscopy (XPCS) has many similarities with the previously described DLS technique, as it looks at how intensity fluctuations of scattering changes with time [33, 34]. Instead of a laser beam, this technique uses a sufficiently coherent X-ray beam. This has the advantage as due to its different values of scattered angles and times, it allows for measurements also of turbid samples with smaller risk of multiple scattering. It is possible to measure over longer timescales (larger length scales) than what is feasible with light scattering techniques. The interference from the scattered

---

<sup>d</sup> The coalescence index is typically denoted simply as CI in literature, but has been labelled as CI\* in this dissertation to distinguish it from the creaming index. The similarity between the indices that use similar approaches and differ only slightly in their definitions, is a common cause of confusion.

photons forms a speckle pattern. The speckle changes over time and is analysed to obtain information about microlevel dynamics such as diffusion, relaxation and motion of particles as well as particle size.

Two-dimensional data collection on the detector allows for measurements at a range of angles (i.e., momentum transfer,  $Q$ ). By comparing images taken at different times, separated by time  $\tau$ , it is possible to obtain the autocorrelation functions at each  $Q$  that are given by:

$$g_2(Q, \tau) = \frac{\langle I(Q, t) I(Q, t + \tau) \rangle}{\langle I(Q, t) \rangle^2}$$

These functions are often fitted with a stretching exponent,  $\alpha$ , to obtain an apparent relaxation time,  $\tau_a$ , using the Kohlrausch-Williams-Watts (KWW) equation:

$$g_2(Q, \tau) = 1 + \beta e^{-2\left(\frac{\tau}{\tau_a}\right)^\alpha}$$

$\alpha$  is a parameter allowing for a distribution of relaxation times ( $\alpha > 0$ ) and  $\beta$  describes the coherence of the beam ( $0 < \beta \leq 1$ ) [35, 36]. For the measurements in this dissertation,  $\beta$  was fixed at 0.3 based on the instrument configuration and the source at the European Synchrotron Radiation Facility (ESRF) [37]. The characteristic relaxation time,  $\tau_c$ , was obtained by normalizing to the gamma function,  $\Gamma(x)$ , and  $\alpha$ , as:

$$\tau_c = \tau_a \left( \frac{\Gamma\left(\frac{1}{\alpha}\right)}{\alpha} \right)$$

For Brownian random diffusive motion, the characteristic relaxation time is proportional to the inverse of the square of momentum transfer as  $\tau_c \propto 1/Q^2$ . The relaxation rate,  $1/\tau_c$ , can be used to distinguish between translational,  $D_T$ , and rotational diffusion,  $D_R$ , as:

$$\frac{1}{\tau_c} = D_T Q^2 + D_R$$

From the Stokes-Einstein equation described in subsection 3.1.1, the corresponding hydrodynamic radius can then also be obtained from the translational diffusion coefficient.

### 3.1.3 Zeta potential

Zeta potential represents the electrical potential difference between the surface of a dispersed particle and the surrounding medium [38]. This is a useful

metric in assessing the contribution of charge to stability and gives an indication of if systems are likely to resist droplet coalescence and particle aggregation and remain their stability over time. A high (positive or negative) zeta potential implies that particles repel each other and that the colloidal suspension is stable against aggregation.

The particles in a dispersion are surrounded by an electrical double layer (EDL), consisting of the Stern layer close to the particle surface and a diffuse layer where the counterions are more loosely associated to the particle. The distribution of ions in the diffuse layer is dependent on the ionic strength of the solution and can be described by the Poisson-Boltzmann equation, where the screening length is called the Debye length. The particle radius and the Debye length is described as the hydrodynamic radius in a DLS measurement as the EDL moves with the particle. The zeta potential is measured at a point called the slipping plane, at the interface between the edge of the EDL and the surrounding medium.

The method used to calculate the zeta potential is called electrophoresis and measures the velocity of charged particles under an electric field. The velocity is then related to the zeta potential by the Helmholtz-Smoluchowski equation. The zeta potential,  $\zeta$ , is described in terms of the viscosity of the medium,  $\eta_c$ , the electrophoretic mobility,  $U_E$ , the dielectric constant,  $\epsilon$ , and the Henry function,  $f(\kappa r_p)$ , where  $\kappa^{-1}$  is the Debye length and  $r_p$  is the radius of the particle, as:

$$\zeta = \frac{3\eta_c U_E}{2\epsilon f(\kappa r_p)}$$

If the Debye length is large compared to the particle size ( $r_p \kappa \ll 1$ ), the Henry function approaches the Hückel limit of 1 for low ionic strength solutions. If the Debye length is small compared to the particle size ( $r_p \kappa \gg 1$ ), the Henry function approaches the Smoluchowski limit of 1.5 for high ionic strength solutions [39]. For the work in this dissertation with dispersions of pea protein in water or 0.1 M citrate buffer at different pH in paper I, and with commercial products with different materials in paper VI, the Smoluchowski approximation for the Henry function was used. As expected, the zeta potential is greatly affected by the ionic strength as this determines the thickness of the diffuse layer. pH also affects the ionization of functional groups on the surface which directly affects the surface charge and hence the electrophoretic mobility and zeta potential. The condition where the zeta potential is zero is called the isoelectric point (IEP) and typically occurs between pH 4 and 5 for protein systems, depending on their specific amino acid composition. The IEP for dispersions of pea protein used in this work was found around pH 4.67 (paper I). At this condition, the particles have little electrostatic repulsion, which makes them prone to aggregation and sedimentation.

### 3.1.4 Optical Microscopy

Optical microscopy, also called light microscopy, is a common imaging technique that looks at how visible light ( $\sim 400\text{-}700\text{ nm}$  wavelength) interacts with materials in a sample. Such interactions can be absorption, reflection, fluorescence and scattering as shown schematically in Figure 8. The light is collected and magnified by objectives and ocular lenses. The technique is highly suitable for emulsions as droplets of the order micrometres are well within the resolution of these instruments. An example of a micrograph of a pea protein stabilized emulsion is presented in Figure 3b. Good contrast is essential for high quality images. In conventional microscopy, it is difficult to tune contrast. This is where more exotic techniques such as CLSM that can differentiate between different components are useful.

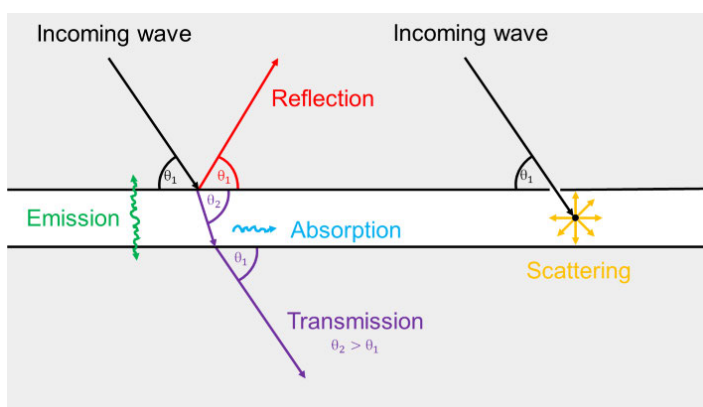


Figure 8. Schematic representation of how waves such as light or X-rays interact with matter. Reflection occurs when the incident energy is bounced off a surface. Transmission occurs when the incident energy is passed through a material. Absorption occurs when the incident energy is taken in by the material and converted to another form such as heat. Emission occurs when absorbed energy is released as radiation energy. Scattering occurs when the incident energy is spread in multiple directions when encountering particles or inhomogeneities in a material.

### 3.1.5 Confocal Laser Scanning Microscopy (CLSM)

CLSM is a fluorescence-based technique, taking advantage of energy relaxation of certain molecules (fluorophores) [40]. In this technique, a focused laser beam hits the sample and photons are absorbed so that the electrons in the molecule reach a higher energy state. Following this excited energy state is a relaxation process to return to the original ground state, where excess energy at a longer wavelength is released through for example heat, vibrational energy and radiative transitions. The radiative transitions involve photons that are being emitted which is observed as light (fluorescence). Light that is out-of-focus is blocked by a pinhole aperture and high-resolution intensity is

collected on a detector. The signal can be tuned by adjusting the wavelength of the incoming laser to decide which molecules are being excited.

Emulsion components are generally not fluorophores, however, by including fluorescent dyes in the samples, confocal microscopy is a very useful technique to distinguish between the different components. The two dyes used in this work include 9-(diethylamino)-5H-benzo[a]phenoxazine-5-one (Nile Red) [41] (Figure 9a) and *trans*-4[4-(dimethylamino)styryl]-1-methyl-pyridinium iodide (4-DASPI) [42, 43] (Figure 9b). Nile Red is a hydrophobic fluorophore with conjugated double bonds used to stain oil droplets and shows high intensity in polar environments (Figure 9c). 4-DASPI is a dye but also a molecular rotor, meaning that its fluorescence is dependent on the viscosity of the medium. A molecular rotor can relax back to the original ground state either by fluorescence or by intramolecular rotation. When the viscosity is high, the rotation is restricted and fluorescence is favoured which gives high intensity. 4-DASPI was used to label the pea protein in this work (Figure 9d).

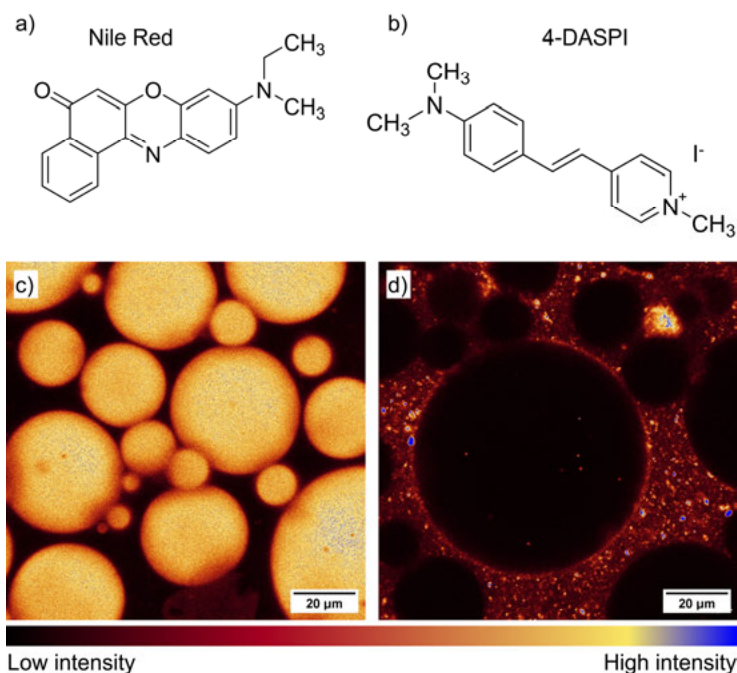


Figure 9. Chemical structure of a) Nile Red and b) 4-DASPI used as fluorescent dyes for the oil and protein, respectively. Confocal microscopy images highlighting c) oil droplets, and d) proteins in the continuous phase. The intensity is given by the colour scale at the bottom of the images.

## 3.2 Scattering techniques to evaluate emulsion structure

To investigate the microstructure of emulsion systems, scattering techniques are often useful. DLS and SLS to measure droplet and particles sizes rely on scattering of low energy photons (light) as described in subsection 3.1.1, whereas other scattering techniques based on high energy photons (X-rays) include ultra-small, small and wide angle X-ray scattering (USAXS, SAXS and WAXS) and XPCS.

Typically, oil-in-water emulsions are composed of micrometre sized droplets stabilized by smaller stabilizing materials as particles, unfolded polymer chains or small molecules in the nanometer size range. X-ray scattering techniques can cover multiple orders of length scales, which makes them useful techniques to understand emulsion structure. By comparing the slope and intensity of the scattering distribution with theoretical and physical models, quantitative conclusions about sizes, shapes and densities can be made. The extent of the analysis is dependent on background knowledge of samples such as components, volume fractions and scattering length densities (SLD). The SLD reflects how much scattering that occurs from a material [44] and has different values for X-rays and neutrons. A list of SLD values for the materials used in this study is seen in Table 1.

Table 1. Approximate SLD for X-rays [45] and neutrons [46] for components relevant to the study of emulsions in this work.

Material	X-ray SLD [ $10^{-6} \text{ \AA}^{-2}$ ]	Neutron SLD [ $10^{-6} \text{ \AA}^{-2}$ ]
D <sub>2</sub> O	9.41	6.35
H <sub>2</sub> O	9.41	-0.56
Rapeseed oil	8.40	0.10
Pea protein isolate in D <sub>2</sub> O	10.6	5.10 <sup>e</sup>
Pea protein isolate in H <sub>2</sub> O	10.6	0.13 <sup>e</sup>
Pea protein isolate powder	13.2	1.70

One way to determine SLD is to use neutron scattering techniques such as ultra-small/small angle neutron scattering (USANS/SANS) and spin-echo small angle neutron scattering (SESANS). This can only be done at large-scale facilities. Measurements with X-rays can be performed quickly in large-scale synchrotron facilities (milliseconds measurement times) and in laboratories (minutes measurement times), while neutron measurements take longer times (minutes to hours measurement times) due to the lower incident flux. However, the main advantage over X-rays is the possibility to tune the SLD of particular components of a material by mixing different isotopes without significantly changing the systems. The most common way to do this is by

<sup>e</sup> The SLD is expected to change linearly for mixtures of D<sub>2</sub>O and H<sub>2</sub>O. See details in Figure 3 in paper IV.

adjusting the ratio of D<sub>2</sub>O to H<sub>2</sub>O in the solvent and thus match the SLD of either the oil droplets or the protein structures in emulsions.

The techniques described in the following subsections have been a central part in the work described in this dissertation. They have been used complementary to gain information about structure on many length scales. The following subsections describe in more detail the concepts of these techniques, with a reference to Appendix A that describes a general procedure to collect good scattering data.

### 3.2.1 Ultra-Small/Small/Wide Angle X-ray Scattering (USAXS/SAXS/WAXS)

SAXS uses X-rays that scatter off the electron cloud of the atoms in a sample [47, 48]. With incoming X-rays with wavelengths smaller than the structures aimed to be measured, the intensity of the scattered X-rays at different (small) angles is directly related to the size, shape, density and interactions of the material. Typical length scales include for example polymer chain dimensions and lamellar spacing. A representative SAXS experimental setup is shown in Figure 10. A description of the general procedure to perform a SAXS measurement is outlined in Appendix A.

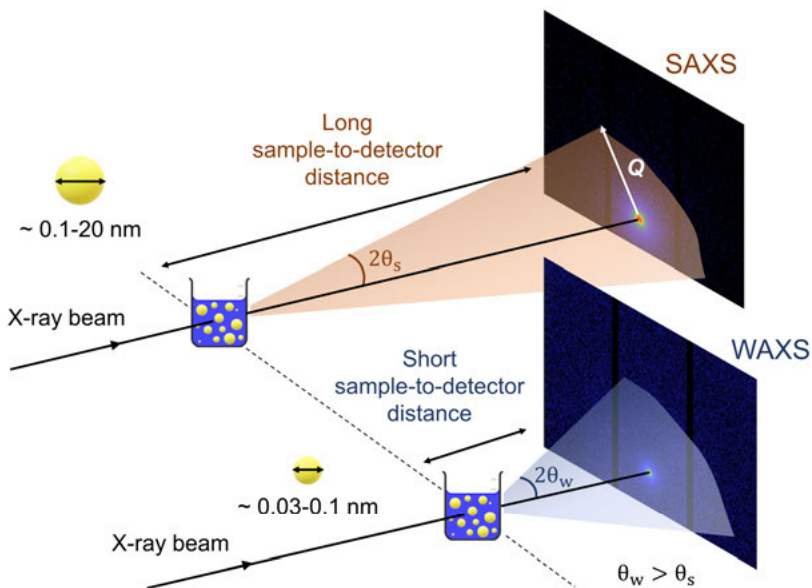


Figure 10. Schematic setup of the SAXS instrument. The sample shown is an emulsion, which shows no sharp diffraction peaks but rather broad features in intensity. In a SAXS measurement, the sample-to-detector distance is long to detect small scattering angles, and in a WAXS experiment, the distance is short to detect scattering at larger angles.

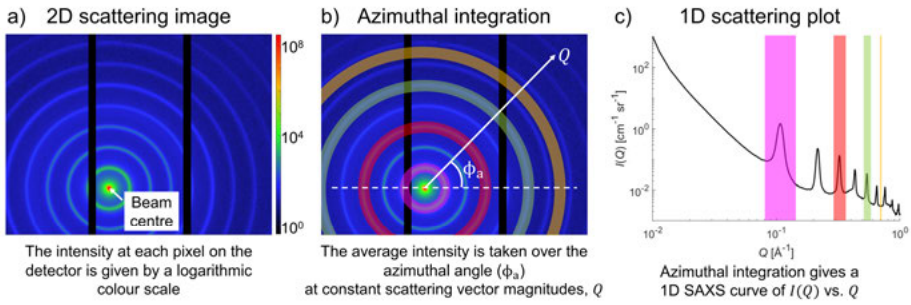


Figure 11. Example of scattering patterns for an Ag Behenate sample. a) Two-dimensional SAXS detector image with intensity between  $10^0$  to  $10^8 \text{ cm}^{-1} \text{ sr}^{-1}$ . b) Concept of azimuthal integration performed by taking the average intensity along rings centred at the beam centre. c) Final one-dimensional curve of intensity ( $I$ ) versus scattering vector ( $Q$ ).

A typical laboratory X-ray source used is Cu  $K_\alpha$  with a wavelength,  $\lambda$ , of  $1.54 \text{ \AA}$ , whereas large-scale facility sources can operate at various wavelengths. The typical scattering angles,  $\theta$ , measured are in the range  $0.1$ - $10^\circ$ , which corresponds to scattering vectors/momentum transfer,  $Q$ , in the approximate range of  $10^{-3}$  to  $10^{-1} \text{ \AA}^{-1}$ . This technique is based on elastic scattering, meaning that no change in photon energy is occurring, only in the direction of  $Q$ . The relationship between  $Q$  and  $\theta$  is given by:

$$Q = \frac{4\pi}{\lambda} \sin\left(\frac{\theta}{2}\right)$$

Intensity at a particular value of  $Q$  is related to correlations at real space distances,  $d$ , given by:

$$d \cong \frac{2\pi}{Q}$$

A two-dimensional SAXS detector image is converted to a one-dimensional scattering curve by azimuthal integration (radial averaging) according to the procedure in Figure 11. The intensity at concentric circles with constant scattering vector is averaged over the azimuthal angle,  $\phi_a$ , as:

$$I(Q) = \frac{1}{2\pi} \int_0^{2\pi} I(Q, \phi_a) d\phi_a$$

to obtain the final one-dimensional curves of  $I(Q)$  versus  $Q$ . This expression assumes that complete rings are on the detector. However, in practice, rings at large  $Q$  are only partially recorded, the beam is not necessarily at the center and the detector contains masked regions. Therefore, the averaging is slightly

more complicated as it is performed over the angular range that is available and normalized by the actual angle rather than by  $2\pi$ .

Depending on the length scales that one is interested to measure, the sample-to-detector distance can be adjusted and hence the scattering angles measured can be chosen. However, pushing a conventional pinhole SAXS geometry to ultra-small angles would require impractically long sample-to-detector distances and a fine collimation causing substantial reduction in incident intensity. To further extend the range of  $Q$  and detect smaller scattering angles down to approximately  $2 \times 10^{-4} \text{ \AA}^{-1}$  (corresponding to real structures of several micrometers), additional channel-cut Si crystals can be added in a so called Bonse-Hart USAXS configuration [49, 50]. This setup is presented in Figure 12a. The additional monochromator placed between the source and the sample is used to monochromate and collimate the beam, and the analyzer located between the sample and the detector is used to scan over very small angles to obtain the scattering intensity in only one direction at each angle. In the USAXS setup, the value of  $Q$  is thus determined by the analyzer crystal, rather than as an angle on the detector. This geometry allows for high resolution in one direction with a large beam and hence a higher incident intensity is feasible than with the pinhole SAXS collimation.

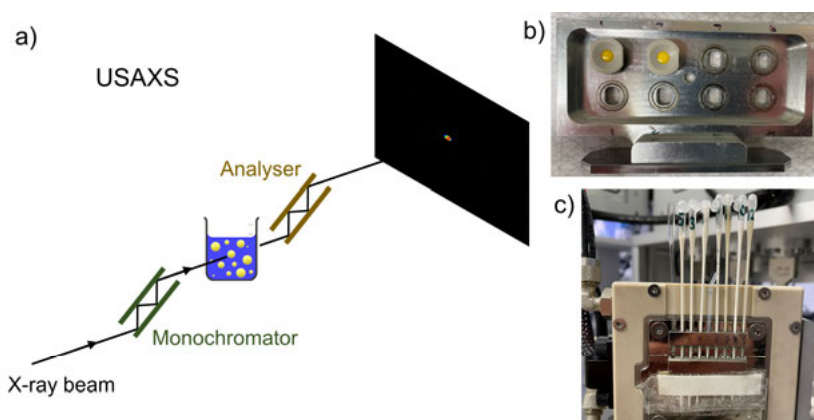


Figure 12. a) Schematic of the Bonse-Hart USAXS instrument. The monochromator crystals placed before the sample monochromate and collimate the beam, while the analyser crystals placed after the sample are rotated in very small angular steps to scan the scattering intensity. b) Picture of the gel holders most frequently used for the SAXS and USAXS experiments included in this dissertation. c) Image of the capillary holder used for the temperature controlled SAXS experiments in this work.

In both the USAXS, SAXS and WAXS modes, liquid samples are mounted in holders such as capillaries (Figure 12c), gel holders (Figure 12b) or flow through cells depending on sample properties such as viscosity, composition, required beam size, and sample volume available. A capillary (1 to 2 mm thickness) would practically require a fluid sample and although a small

volume can be advantageous for expensive materials, it restricts the flux to that of a small beam (collimation slit widths typically  $0.4 \times 0.4$  and  $0.7 \times 0.7$  mm<sup>2</sup>). Gel holders, on the other hand, are useful for more viscous samples and allows for a bigger beam (higher flux) which is required for USAXS measurements. These holders typically use Kapton windows to confine the samples. Due to the scattering from air, samples are usually placed in vacuum during the measurements to reduce background. This puts requirements on proper sealing, which is typically done with epoxy glue for capillaries and mechanical locking with O-rings in gel holders. Both capillaries and gel holders have been used for the measurements in this work.

### 3.2.2 Ultra-Small/Small Angle Neutron Scattering (USANS/SANS)

USANS and SANS rely on similar physical mechanisms as X-ray scattering techniques (USAXS and SAXS) [48]. In X-ray experiments, photons interact with the electron clouds of atoms through Thomson scattering and the scattering contrast is therefore highly dependent on the atomic number,  $Z$ , leading to different intensities for materials across the periodic table. Neutrons on the other hand, interact with the atom core and hence the scattering from a material with the same elemental composition but with different numbers of neutrons in the core (different isotopes) will show very different scattering. Despite the high cost of these types of experiments and that it is only available at large scale facilities, it is very useful in the sense that the signal from different components in a sample can be tuned by mixing different isotopes.

The most common method to “match” out different components is by using deuterated materials. In an emulsion system, useful component matching could for example be done by mixing appropriate ratios of H<sub>2</sub>O and D<sub>2</sub>O of the aqueous phase to get a similar SLD as that from the dispersed oil phase. A schematic representation of how the SLD of the continuous (water) phase is varied with D<sub>2</sub>O concentration is shown in Figure 13. The colours on a rainbow scale represent different SLD. For example, the SLD of pure H<sub>2</sub>O is  $-0.56 \times 10^{-6} \text{ \AA}^{-2}$  (red colour), whereas 10% v/v D<sub>2</sub>O in H<sub>2</sub>O has a SLD of about  $0.13 \times 10^{-6} \text{ \AA}^{-2}$  (yellow colour) which is similar to the SLD of the droplets (yellow colour). This contrast would hence enhance the scattering contribution from the stabilizer material (black colour). Instead, a higher content of D<sub>2</sub>O close to 40% v/v (black colour) would reduce the signal from this component and the scattering from droplets would dominate the scattered intensity. With neutron scattering, it is thus possible to distinguish contributions from different components without changing the behaviour or composition of the system. This is not as easily done with X-ray techniques.

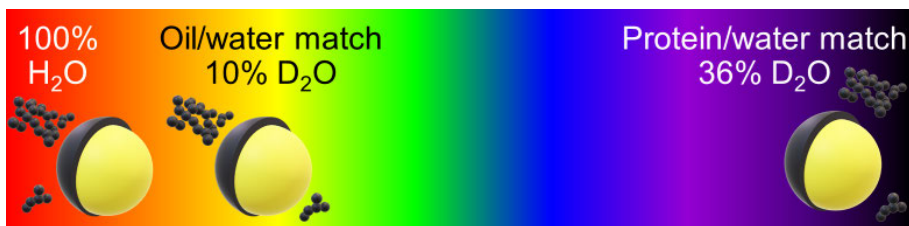


Figure 13. The concept of contrast variation in a neutron experiment. By matching the SLD of two of the components in the system, the contribution from the third component can be enhanced. The SLD is determined by the amount of deuterium in a material and in this graphical representation, the SLD is shown on a rainbow colour scale.

### 3.2.3 Spin Echo Small Angle Neutron Scattering (SESANS)

SESANS is used to investigate large structures [51], but in contrast to pinhole SANS experiments which would require very long sample-to-detector distances, a narrow wavelength spread and a low divergence to access such small angles, the incoming neutron flux can be kept high. This is because instead of resolving the scattered intensity at different angles on a detector, SESANS measures changes in the precession of the neutron spin [52]. The technique thus detects scattering angle by measuring the corresponding reduction in beam polarization.

SESANS experiments rely on the same scattering principles as conventional SANS, however there is a key difference in how the data are expressed. Instead of obtaining data as a function of  $Q$ , which is a vector in reciprocal space and perform a Fourier inversion, this technique provides results through a Hankel transform of the scattering in three dimensions to obtain the correlation function,  $G(\delta)$ , where  $\delta$  is the spin-echo length. The spin-echo length corresponds to the distance that depolarizes the neutrons in precession before and after scattered from the sample.

This real-space representation has many benefits, as it is easier to interpret features such as characteristic sizes. At zero spin-echo length ( $\delta = 0$ ), this function reduces to an expression that is only dependent on the SLD contrast between the medium and the dispersed phase ( $\Delta\rho$ ), the dispersed phase volume fraction ( $\phi$ ), and the characteristic length scale ( $\xi$ ), as:

$$G(\delta = 0) = (\Delta\rho)^2 \phi(1 - \phi)\xi$$

SESANS measurements provide a value of the polarization,  $P(\delta)$ , that is related to how much the spin echo is reduced by scattering within a sample. This is expressed by:

$$P(\delta) = e^{-t_s \lambda^2 (G(\delta) - G(0))}$$

where  $t_s$  is the sample thickness and  $\lambda$  is the neutron wavelength. The dependence on  $t_s$  and  $\lambda$  is then removed in the conventional representation using the normalized form:

$$G(\delta) - G(0) = \frac{\ln(P(\delta))}{t_s \lambda^2}$$

In plots of  $G(\delta) - G(0)$  versus  $\delta$ , one can directly observe how the correlations vary with real-space distance. Typically, a slow decay indicates larger structures and a fast decay is characteristic of smaller structures. In many ways, SESANS complements conventional SANS and is similar to USANS, as it probes much larger real-space length scales, up to tens of micrometres. Therefore, it is highly relevant to use to study emulsions that contains both big oil droplets and protein structures [51].

### 3.2.4 Model Fitting

In this subsection, the procedure used to interpret scattering data, both with X-rays and neutrons, is described. The subsection starts by describing general and model independent interpretations based on intensity and gradients and evolves to describe the analytical models used to fit the data included in this dissertation. The subsection concludes with some discussion of instrumental effects affecting the experimental data that needs to be taken into account.

In analysing scattering data, both with X-rays and neutrons, there are two things that are of main interest – the absolute magnitude of intensity,  $I$ , at particular values of  $Q$  and the  $Q$  dependence of  $I$  in a plot of the logarithm of  $I$  versus the logarithm of  $Q$ .

The intensity is related to the volume fraction of the scatterer and the SLD contrast between the scatterer and the surrounding medium. The SLD is what differs between X-ray and neutron scattering (see Table 1). To deduce such parameters without introducing arbitrary scale factors, it is therefore essential to obtain data on an absolute scale by accounting for the sample thickness and transmission, knowing the direct beam intensity and the solid angle of the instrument and to subtract background scattering from empty holders.

The  $Q$  dependence is typically described by the form factor,  $P(Q)$ , representing the scattering of individual objects. Characteristic length scales may give rise to oscillations, however in certain  $Q$  ranges, a power-law behaviour,  $I \propto Q^p$ , can be observed. Different shapes and structures of the scatterer give different values of  $p$  that can often be found in tables [53, 54]. Examples of scattering patterns of spheres, cylinders and mass fractal shapes are shown in Figure 14. Those have values of  $p$  that are -4 for spheres, -1 and -4 for cylinders and between -3 and -1 for mass fractals.

The intensity can typically be described as the product of  $P(Q)$ , describing the shape and size of a single scatterer such as an atom, a molecule or a particle, and a structure factor,  $S(Q)$ , describing how multiple scatterers are arranged relative to each other. The structure factor adds correlation peaks or oscillations arising from interference to this smooth curve. However, it is important to note that this division into factors is an approximation assuming that the shape of the objects is not affected by their positions.

Model independent fitting by simply looking at intensities and gradients in scattering curves can often be helpful in understanding overall shapes and sizes before attempting to fit more complicated models directly. As such analyses are based mainly on the form factor, it is important to take the gradient over a significant range of  $Q$  to exclude local oscillations arising from correlations between objects. Scattering curves are often divided into different parts such as in Guinier and Porod regions [47, 55]. A Guinier region is seen as a turnover at the lowest  $Q$  at the condition when  $QR \ll 1$ , and this describes the overall size and radius of gyration of an object. This is for example seen as a flat level ( $I \propto Q^2$ ) at low  $Q$  for monodisperse spheres in Figure 14a. The intensity in a region of  $Q$  that follows the Porod law,  $I \propto Q^{-4}$ , gives a measure of the specific surface area (area per volume) of an object and is, for example, seen at  $Q > 0.05 \text{ \AA}^{-1}$  for the sphere models in Figure 14a.

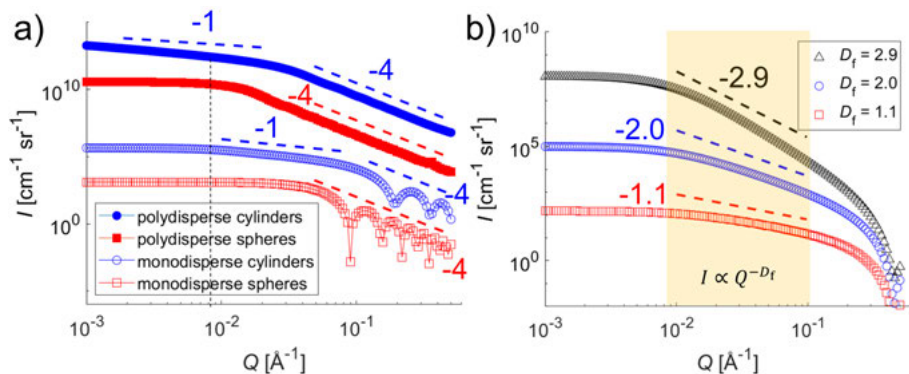


Figure 14. Scattering patterns for typical particle shapes and corresponding decay rates ( $p$ ). a) Polydisperse populations of cylinders (blue filled circles) and spheres (red filled squares) show characteristic  $p$  of -1 and -4. Monodisperse populations (open symbols) show the same form factor decay rates but with clear local minima and maxima caused by the structure factor. b) Mass fractal models with fractal dimensions and corresponding  $p$  of 1.1 (red squares), 2 (blue circles) and 2.9 (black triangles). Here, the Teixeira model [56] has been used with radius of building blocks  $10 \text{ \AA}$  and cut-off length  $100 \text{ \AA}$ . The curves are shifted in intensity for visibility in both a) and b).

In the following subsections, some of the analytical models that have been used to represent the emulsions and protein dispersions in this work will be

described. Graphical representations of these models are presented in Figure 15.

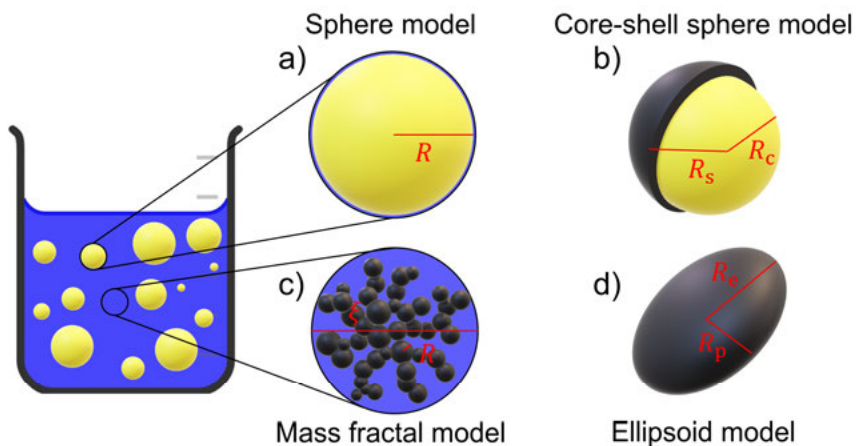


Figure 15. Graphical representation (not to scale) of models used for the work on emulsions and protein structures in this dissertation. These include a) sphere, b) core-shell sphere, c) mass fractal and d) oblate ellipsoid models.

### 3.2.4.1 Spheres and core-shell spheres

Sphere models are among the most frequently used in scattering experiments, as many objects can be approximated as spherical. This includes for example oil droplets, nanoparticles or micelles. The scattering from spheres is given by:

$$I_S(Q) = \frac{\phi}{V} \times \left[ 3V(\Delta\rho) \times \frac{(\sin(QR) - QR\cos(QR))}{(QR)^3} \right]^2 + I_b$$

where  $\phi$  is the total volume fraction of all scatterers,  $R$  and  $V$  are the radius and volume of a single scatterer,  $\Delta\rho$  is the SLD contrast between the scatterer and the surrounding medium, and  $I_b$  is the source background [55]. For a perfect monodisperse population, this function shows clear minima and maxima as seen in Figure 14a. However, for polydisperse systems, these features are broadened to show only the overall envelope.

To evaluate systems where, for example, oil droplets consist of a shell of adsorbed emulsifiers or of spherical particles with a dense inner core surrounded by a shell that has a different SLD, the core-shell sphere model is an extension of the sphere model. The model sums the scattering amplitudes from the regions that scatter coherently (core and shell) and takes the square to obtain the combined intensity as given by:

$$I_{\text{CSS}}(Q) = \frac{\phi}{V} \times \left[ 3 \left( V_c(\Delta\rho_{\text{cs}}) \times \frac{(\sin(QR_c) - QR_c \cos(QR_c))}{(QR_c)^3} + \frac{V_s(\Delta\rho_{\text{sm}}) \times (\sin(QR_s) - QR_s \cos(QR_s))}{(QR_s)^3} \right) \right]^2 + I_b$$

where  $V_c$  and  $R_c$ , and  $V_s$  and  $R_s$  are the volumes and radii of the spherical cores and shells, respectively, and  $\Delta\rho_{\text{cs}}$  and  $\Delta\rho_{\text{sm}}$  are the SLD contrasts between the core and the shell, and the shell and the surrounding medium, respectively. The core-shell sphere model was used early in this work (paper I) to represent emulsions consisting of oil droplets covered by a layer of adsorbed proteins at the surface.

### 3.2.4.2 Ellipsoids and polydispersity

An ellipsoid describes an object with anisotropic shape, that have different dimensions along its axes. In the rotationally symmetric case, an ellipsoid can be described by two different radii, the equatorial radius,  $R_e$ , and the polar radius,  $R_p$ . This model was used in paper I to represent the scattering from dispersed proteins. For randomly oriented ellipsoids, the model is given by:

$$I_E(Q) = \frac{\phi}{V} \times \int_0^{\pi/2} \left( \left[ 3V(\Delta\rho) \times \frac{(\sin(QR_E) - QR_E \cos(QR_E))}{(QR_E)^3} \right]^2 \sin a \, da \right) + I_b$$

and  $R_E$  is given by:

$$R_E = \sqrt{R_c^2 \sin^2 a + R_p^2 \cos^2 a}$$

where  $a$  is the angle between the ellipsoid axis and  $\vec{Q}$ . In many ways, the scattering described by this model is similar to the scattering from polydisperse spheres despite the structural models being different. Both anisotropy, polydispersity and poor resolution cause broadening of the minima in the oscillations characteristic for perfect monodisperse spheres. In practice, the ellipsoid model is often used to model, for example, polydisperse populations of spheres, where the extra radial parameter is introduced to fit the data. As long as there is no alignment of the ellipsoids by, for example, applying a magnetic field or high shear that may cause an anisotropic scattering pattern, it is not trivial to distinguish between the two types of models. It is also not so far off to think about both of them as describing objects with different radii, either as viewed from different directions (ellipsoids) or as viewed as different objects (polydisperse sphere population).

### 3.2.4.3 Mass fractal structures

Mass fractal structures [56] are characterised by self-similarity in structure over a range of length scales and have been used to model the protein dispersed in an aqueous phase in this work (papers II & IV). This model is common to describe for example porous networks, aggregates and gels. The model can be thought of as spheres as individual scatterers (building blocks), forming a hierarchical structure up to a cut-off length (cluster size), and is mathematically described as:

$$I_F(Q) = \phi V(\Delta\rho)^2 P(Q) S(Q) + I_b$$

with form and structure factors given by:

$$P(Q) = \left( \frac{3(\sin(QR) - QR \cos(QR))}{(QR)^3} \right)^2$$

$$S(Q) = 1 + \left( \frac{D_f \Gamma(D_f - 1)}{\left(1 + \frac{1}{(Q\xi)^2}\right)^{(D_f - 1)/2}} \right) \times \frac{\sin\left((D_f - 1) \tan^{-1}(Q\xi)\right)}{(QR)^{D_f}}$$

where  $D_f$  is the mass fractal dimension,  $\xi$  is the correlation length or cut-off length (i.e. cluster size), and  $\Gamma(x)$  is the gamma function.

The mass fractal dimension is in the range  $1 < D_f < 3$ , describing how the mass of a structure scales with its size. A value of  $D_f = 1$  corresponds to elongated string-like objects such as needles or polymer chains in a solution. A value of  $D_f = 2$  corresponds to diffuse networks such as polymer gels or flat objects such as sheets. A value of  $D_f = 3$  describes fully space-filling objects such as compact spheres. The  $D_f$  was about 2.75 for the protein network investigated in this work.

This model shows a turnover at low  $Q$  where  $Q \sim 1/\xi$ , a power law of  $I(Q) \propto Q^{-D_f}$  at  $1/\xi \ll Q \ll 1/R_p$ , and at high  $Q$ , the scattering is dominated by the form factor of the individual scatterers. This is seen in Figure 14b. This model is in many ways similar to the sum of multiple models of spheres of different sizes. Therefore, it is not strange to think about this model as a good representation of a polydisperse distribution or materials of irregular shapes.

### 3.2.4.4 Guinier-Porod model

The Guinier-Porod model is a less structurally specific model compared to the previously mentioned ones, and is used mainly when the morphology is less well-known. Rather than a physical model describing real structural properties, it is an arbitrary model that provides parameters related to size and structure. It connects regions in  $Q$  space with Guinier (low  $Q$ ) and Porod (high  $Q$ ) behaviour to obtain information about the radius of gyration,  $R_g$ , and the Porod

exponent (dimensionality or roughness of surface),  $d_c$ . The model does not assume self-similarity as in the fractal model in subsection 3.2.4.3, however it is sometimes used to model systems with multiple structural levels. This would be reflected as multiple Guinier-Porod regions at different  $Q$  and could be similar to a mass or surface fractal model describing particles (building blocks) within a cluster (correlation length). The Guinier-Porod model in one structural level is given mathematically by:

$$I_{\text{GP}}(Q) = \begin{cases} G \times e^{-\frac{(QR_g)^2}{3}}, & Q \leq Q_1 \\ \frac{D}{Q^{d_c}}, & Q \geq Q_1 \end{cases}$$

where  $D$  and  $G$  are the scale factors for the Porod and Guinier models and  $Q_1$  is the transition point, making a smooth transition in intensity and gradient between the Guinier and Porod regions. This point is given by:

$$Q_1 = \frac{1}{R_g} \sqrt{\frac{3d_c}{2}}$$

The Guinier-Porod model has been used in paper IV to describe the scattering from proteins dispersed in a medium at pH below neutral.

### 3.2.4.5 Smearing of models

The scattering patterns given by the model calculations deviates from real measurements due to finite instrumental resolution, so called smearing. Finite resolution in  $Q$  leads to broadening of sharp features in intensity, for example broadening of the sharp minima in the form factor.

In scattering, there are two common instrumental geometries for beam collimation – pinhole and slit collimation. The pinhole collimation is used for SAXS/SANS measurements and gives an isotropic beam on the detector. The pinhole smearing arises mainly from the finite beam divergence. The slit collimation is used in the Bonse-Hart USAXS/USANS setups and uses channel-cut crystals that have specific angular acceptance of the beam and gives a slit smeared resolution function [57]. This gives a very good resolution in the narrow direction but very poor resolution in the long direction. The intensity from slit smeared measurements is calculated by the integral over the long slit direction [58]. The integration causes data that have been measured in a slit smeared collimation to have a gradient in a plot of  $I$  versus  $Q$  to decrease by one (Figure 16a).

Usually, it is preferable to smear the models to comply with the resolution of the instruments rather than trying to desmear data directly. Desmearing of USAXS data [59] may cause artefacts such as oscillations and often some algorithms are required to smoothen the desmeared curves. There are certainly

challenges with desmearing of data and smearing of models, particularly to determine the instrumental resolution. The effective slit lengths, that depend on the geometry of the crystals and the beam divergence, are typically not easy to determine but some values have been estimated for various instruments [60, 61, 62]. Figure 16b shows an example of how the slit length affects the shape and intensity of a curve of the sum of a sphere and a fractal model.

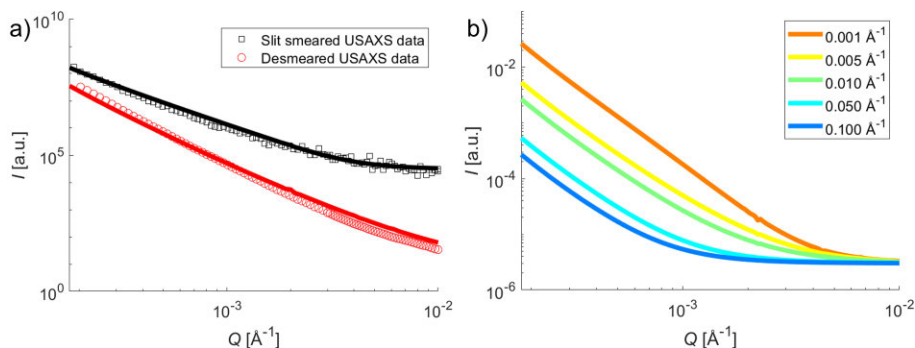


Figure 16. a) Slit smeared (black squares) and desmeared USAXS data (red circles) of an emulsion with 50% v/v oil and 7.5% w/v protein. The lines represent model fits of a sphere model combined with a fractal model. Smearing of models is usually preferred over desmearing of data, as it avoids the introduction of additional noise or oscillations. The difference in gradient between the data sets comes from the integration in the calculation of the intensity in the slit smeared configuration. b) Sphere and fractal models that have been smeared with different slit lengths of 0.001 to 0.100  $\text{\AA}^{-1}$  in SasView version 5.0.6 [63].

Similarly, as for the difficulty in distinguishing between ellipsoids and poly-disperse spheres described in subsection 3.2.4.2, smearing typically gives similar effects, causing structural information such as sharp minima to vanish. Fitting of the USAXS and SAXS data sets in this work have been performed separately without desmearing. Desmearing of the USAXS data has been done only for visual purposes to plot them on the same graph as the SAXS data.

### 3.3 Rheology

In addition to the thorough work with X-ray and neutron scattering techniques, substantial results have been obtained from rheological measurements. The word 'rheology' is composed of the Greek words 'logia' and 'rheo' which means the 'study of flow' [64]. Intuitively, rheology can be related to everyday properties such as the 'creaminess' of ice cream, 'pourability' of yoghurt, 'spreadability' of a paint, 'stability' of a salad dressing, or the "twistability" of an Oreo cookie [65]. Direct measures of viscosity and deformation can be

obtained, which would relate directly to for example mouthfeel in foods and indirectly to gelation mechanisms and internal structure of soft matter systems. The technique is used widely in a range of applications, including both fundamental structural characterization and industrial applications.

Rheology is a common area of study to understand the flow and elastic properties of many different types of complex fluids and soft materials. These often have behaviours that are a combination of those of viscous liquids and elastic solids. The behaviours of such materials are also likely to depend on the deformation history of the sample which could give rise to time-dependent effects such as thixotropy [66]. Thixotropy refers to a process of a decrease in viscosity with time at a constant shear, with a recovery when the shear is removed.

To understand the basic concept of this technique, it is useful to introduce the definitions of shear stress,  $\sigma$ , and shear strain,  $\gamma$ , that determines the viscosity,  $\eta$ . In an idealised rheological setup, one considers two horizontal parallel plates with the material to study in between. Each plate has an area,  $A$ , and are separated by a distance,  $h$ . The upper plate is subjected to a force,  $F$ , in the horizontal direction that moves the plate a distance,  $d_p$ , measured from the original position. The shear stress can be expressed as the force per unit area:

$$\sigma = \frac{F}{A}$$

The shear strain is the ratio of displacement to the separation distance:

$$\gamma = \frac{d_p}{h}$$

The shear rate,  $\dot{\gamma}$ , sometimes referred to as the shear strain rate, is the derivative of the shear strain with respect to time:

$$\dot{\gamma} = \frac{d\gamma}{dt}$$

With an applied shear stress, the viscosity is then the resistance to deformation with time:

$$\eta = \frac{\sigma}{\dot{\gamma}}$$

Variations to the geometry do occur depending on the type of sample that is to be measured. The three most common geometries are plate-plate (Figure 17a), cone-plate (Figure 17b) and concentric cylinder/Couette geometries (Figure 17c). For low viscosity fluids, the concentric cylinder geometry is preferred to prevent the material from flowing out during measurements. This

setup was used for SAXS measurements with *in situ* rheology in paper V. The motivation for the Couette geometry in this case was to access two different planes of the flow field, including the flow-vorticity (tangential position) and the shear-gradient-vorticity (radial position) planes with sufficiently short path lengths [67]. The Couette was made of polycarbonate which does not greatly absorb or scatter X-rays. A schematic of the rheo-SAXS experimental setup is presented in Figure 1 of paper V.

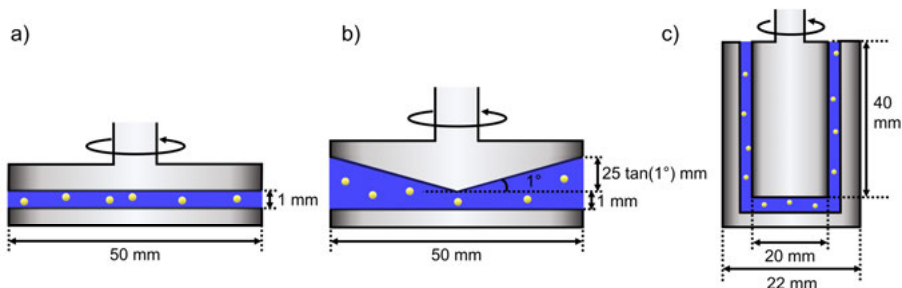


Figure 17. Rheological geometries (not to scale) including a) plate-plate, b) cone-plate and c) concentric cylinder/Couette.

A rough cone-plate geometry was used for the remaining work in this dissertation. This geometry consists of a static plate at the bottom and a rotating cone with a small angle at the top. The angle is necessary to provide a uniform shear rate across the sample, rather than one that varies with the radial distance from the centre, as in the plate-plate geometry. The minimum gap size was set to 0.1 mm in the centre, with a cone angle of  $1^\circ$ . This gives a larger gap at the edges, much larger than the individual emulsion droplets in this work.

In this dissertation, five different types of tests have been performed. They include: shear rate sweeps (papers I, III & V), constant shear stress (papers III & V), strain amplitude sweeps (papers I & III), frequency sweeps (papers I & V), and low strain amplitude and frequency (paper III). The following subsections will describe in more detail the purpose and possible interpretations of the results in each test.

### 3.3.1 Shear rate sweep

Two of the most frequent ways to represent rheological results are by so called flow curves of shear stress versus shear rate (Figure 18a) and of viscosity versus shear rate (Figure 18b). These data are often obtained by performing a series of steady-shear measurements in either controlled shear rate mode (shear rate sweep) or controlled stress mode (stress-controlled flow curve). The difference between shear-thinning, Newtonian and shear-thickening materials are clearly visible in such plots. Emulsions are typically shear-thinning

fluids as the viscosity decreases for higher applied shear rates. Pure water or air would be typical examples of Newtonian fluids that have viscosities that are independent of applied shear. A common example of a shear-thickening fluid is a dispersion of corn starch in water, that becomes more difficult to steer the more force you apply.

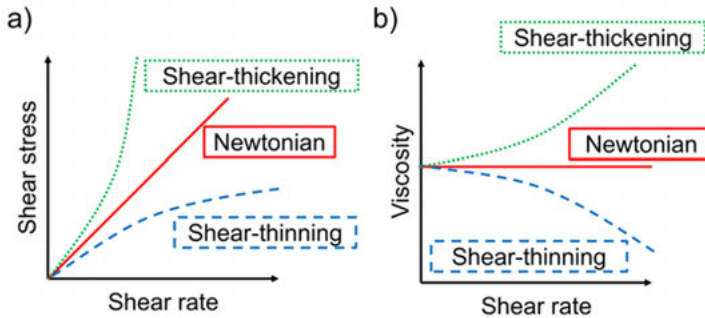


Figure 18. Typical flow curves for shear-thinning (blue dashed lines), Newtonian (red solid lines) and shear-thickening (green dotted lines) materials. Emulsions are usually found to be shear-thinning fluids as they start to flow (viscosity decrease) when more stress is applied (higher shear rate).

In the shear rate sweep, the applied steady shear rate is varied, in this study between  $0.01$  and  $1000 \text{ s}^{-1}$ . This is done to obtain flow curves, relating the shear stress and viscosity to the shear rate. The measurements in this study have been performed mainly as quick sweeps, where each shear rate is held for only a short time of the orders of seconds. This was done to study short-time and transient yield behaviour, reducing thixotropic (time-dependent shear thinning) effects and structural evolution of the protein network with time. It is not uncommon to see that the flow curve varies depending on the time that you wait, and also going from high to low or low to high shear rates typically impacts the curve. For example, Wang and Ewoldt [68] studied the hysteresis of the time-dependent dynamics for thixotropic, antithixotropic and viscoelastic materials and saw that the hysteresis is decreasing at higher ramping rates.

Some analysis of the data in this dissertation was done by evaluating the yield stress,  $\sigma_y$ . This is the minimum stress at which the systems start to flow and can be thought of as the shear stress in the limit of zero shear rate [69]. This quantity can be obtained by fitting flow curves to the Herschel Bulkley model, which describe yield-stress materials such as concentrated emulsions:

$$\sigma = \sigma_y + K\dot{\gamma}^n$$

$n$  is flow index and  $K$  is consistency index. For shear-thinning materials, the flow index is less than 1, for shear-thickening materials it is greater than 1 and

for Newtonian materials it is equal to 1. By fitting this equation to data for emulsions and protein dispersions in paper III, values of the yield stress were found to be of the order 0.01 to 20 Pa depending on the oil concentration.

Additional analysis of how volume fraction of the dispersed phase affects the viscosity can be done by considering the viscosity at zero or low shear rates. The viscosity is related to the volume fraction,  $\phi$ , by the Krieger-Dougherty equation:

$$\eta = \eta_c \left(1 - \frac{\phi}{\phi_m}\right)^{-[\eta]\phi_m}$$

where  $[\eta]$  is the intrinsic viscosity which was taken as 2.5 for hard spheres, and  $\phi_m$  is the maximum packing fraction [70]. The maximum packing fraction for randomly distributed monodisperse hard spheres is 0.64, and typically increases for polydisperse size distributions. The Krieger-Dougherty relationship explains how the viscosity increases as the dispersion becomes more concentrated, and particularly the clear upturn in viscosity as the material approaches the maximum packing fraction. This was particularly seen as the high viscosity in emulsions with 50-60% v/v oil compared to 20-40% v/v oil.

### 3.3.2 Constant shear stress

The constant shear stress measurements, as a steady rheological treatment with a constant applied shear stress, is similar to the shear rate sweep described in subsection 3.3.1, but the purpose was to investigate the yield stress behaviour and structural changes at much longer time scales of several hours rather than of the orders of seconds. The test was similar to a conventional creep test where a constant shear stress is applied and the deformation is recorded over time. However, in this case, the shear rate is monitored over time to investigate how the emulsion transitions from a solid to a liquid-like state.

If a shear stress is applied that is below the yield stress, the viscosity increases over time, showing a more solid like behaviour, and hence the shear rate will decrease as given by the relationship in section 3.3. On the other hand, if the shear stress is above the yield stress, there is constant breakage of the structure and the viscosity and shear rate will remain approximately constant over time due to a more fluid-like behaviour.

The long-term yielding behaviour of two representative emulsions with 7.5% w/v protein, and 40% and 60% v/v oil, were analysed in paper III. These are seen in Figure S5 (paper III) and gave yield stresses of 1 to 70 Pa. These values are slightly higher than the ones obtained from quick shear rate sweeps described in subsection 3.3.1. This is due to the thixotropic behaviour of these systems.

### 3.3.3 Strain amplitude sweep

Strain amplitude sweep, is a type of oscillatory measurement where a shear strain is applied as a sinusoidal curve (positive and negative) with a fixed angular frequency,  $\omega$ , and where the amplitude (absolute value) is varied (increased). The shear stress is recorded over time and by using a Fourier transform, that expresses the signal as a sum of sinusoidal curves with different frequencies, the phase of the main harmonic can be determined. The phase angle,  $\delta_a$ , between the applied shear strain and the recorded shear stress describes the behaviour of the material. Immediate response ( $\delta_a = 0^\circ$ ) is characteristic of an elastic solid with no energy loss. Delayed stress response ( $\delta_a = 90^\circ$ ) describes a viscous fluid with complete energy dissipation to heat. Viscoelastic materials, such as emulsions, have a combination of elastic and viscous behaviour and show  $0^\circ < \delta_a < 90^\circ$ .

This type of oscillatory measurement is typically plotted as the storage modulus,  $G'$ , and the loss modulus,  $G''$ , as functions of the strain amplitude (Figure 19a). These moduli are directly related to the phase angle as:

$$\tan(\delta_a) = \frac{G''}{G'}$$

At the condition  $G' > G''$ , the material is typically described as behaving more like a solid than a liquid, whereas  $G'' > G'$  describes a more liquid-like behaviour. For a representative emulsion with 40% v/v oil and 7.5% w/v in paper I, the cross-over point ( $G' = G''$ ), where the sample starts to behave more like a liquid, was found around 70% strain for a frequency of  $1 \text{ rad s}^{-1}$ .

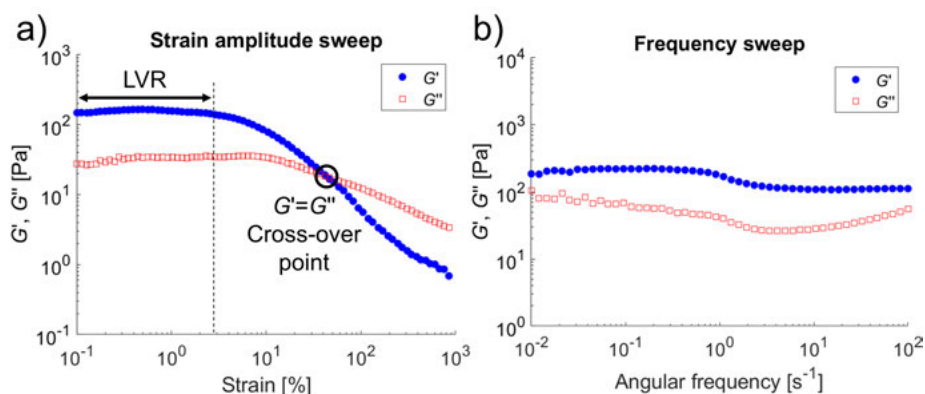


Figure 19. Typical plots of a) an amplitude sweep and b) a frequency sweep for an emulsion with 50% v/v oil and 7.5-10% w/v protein. The storage ( $G'$ ) and loss moduli ( $G''$ ) are plotted. The cross-over point ( $G' = G''$ ) in the amplitude sweep characterizes yielding or structure breakdown. The frequency sweep performed at 1% strain (within the LVR) demonstrates that the elastic component is higher than the viscous component at all frequencies and that the sample shows good gel stability.

Strain amplitude sweeps are primarily used to identify the linear viscoelastic region (LVR) over which values of strain that  $G'$  and  $G''$  remain constant. In this region, the response is reversible and this information is used in other measurements such as that explained in subsection 3.3.4.

### 3.3.4 Frequency sweep

A frequency sweep is another type of oscillatory measurement, with a constant strain amplitude but with varying frequency of the sinusoidal curve. The strain amplitude is generally taken within the LVR as obtained from a strain amplitude sweep measurement described in the previous subsection. The value of strain was taken as 1% in this work. The frequency was varied between 0.01 and 100  $\text{rad s}^{-1}$ . This type of measurement is used to investigate the time scales at which changes occur in a sample. The relatively flat  $G'$  and  $G''$  curves and the comparably higher value of  $G'$  for a typical emulsion in Figure 19b, show that this sample is stable over a range of timescales and behaves more like a solid at this strain amplitude.

### 3.3.5 Low strain amplitude and frequency

Low shear strain of 1% and angular frequency of 1  $\text{rad s}^{-1}$  as oscillatory measurements were applied to assess network formation over time. At such low shear, the viscoelastic network formation dominates rather than flow-induced changes over time. This is well within the LVR, so the microstructure is not disrupted. The response of  $G'$  and  $G''$  was plotted over time to observe the role of elastic and viscous contributions. The results for a dispersion with 7.5% w/v protein, as well as for three emulsions with 40, 50 and 60% v/v oil and 7.5% w/v protein are presented in Figure 4 in paper III. Characteristic behaviour observed for these samples are increases in both storage and loss moduli with time.

## 3.4 Techniques to assess thermal stability

Thermal analysis techniques were used to assess the thermal stability and composition of the protein by investigating their properties as a function of temperature. Thermo gravimetric analysis (TGA) [71] was used as a minor technique in this work to estimate the water content in the pea protein isolate (Figure 20a). This technique monitors the change in mass as a function of temperature and time. In this experiment, there was a ramp in temperature from 25 to 150  $^{\circ}\text{C}$  (15  $^{\circ}\text{C min}^{-1}$ ) with 50  $\text{ml min}^{-1}$  flow of nitrogen gas, followed by a fixed temperature at 150  $^{\circ}\text{C}$  for 360 min. In a TGA experiment, the change of mass compared to the initial state can be due to different

physical processes such as thermal degradation, oxidation, decomposition of the sample or moisture evaporation, and these are taking place at different temperatures and times. The water loss in this experiment was determined as 2.92 mg, corresponding to 5% w/w of the initial protein isolate. The small initial apparent rise in mass of the sample is due to buoyancy effects when the density of the surrounding gas decreases as the temperature is raised [72].

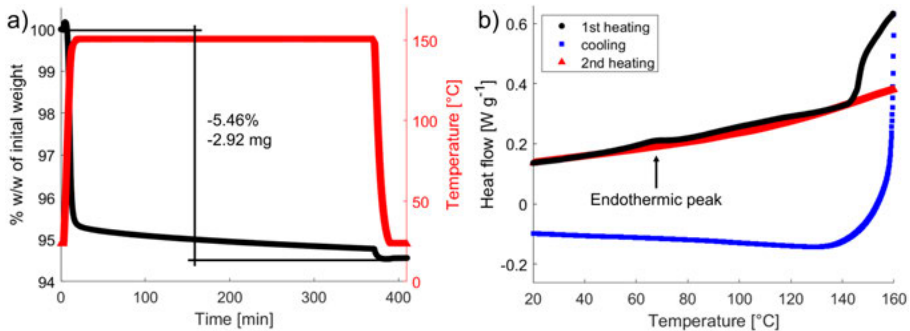


Figure 20. a) Typical TGA curve for the pea protein isolate used in this work. The weight decreased by 5% upon heating at 150 °C for 360 min, suggesting that this is the approximate fraction of water. b) DSC curves with 10 °C min<sup>-1</sup> heating rate for the same pea protein isolate. Endothermic is up. A denaturation peak was observed at approximately 70 °C.

Differential Scanning Calorimeter (DSC) [71] measures the heat flow (absorption or release) in a sample as a function of temperature. A typical experiment is performed as a ramp of temperatures, in this work from 20 to 150 °C at a rate of 10 °C min<sup>-1</sup>, while monitoring the heat flow (Figure 20b). Different physical phenomena such as melting (endothermic), glass transition (endothermic), crystallisation (exothermic) and cross-linking (typically exothermic) involve different thermal transitions which are visible as local maxima (endothermic) or minima (exothermic) in a plot of heat flow versus temperature. The results from the measurements in this study were used particularly to identify the denaturation temperature of the dry protein isolate material. This was found as an endothermic peak at approximately 70 °C, and the process was irreversible as seen by the lack of features in the repeated temperature cycle.

### 3.5 Summary of challenges and opportunities in evaluating emulsion stability

Regarding the methods in section 3.1, they are all complementary approaches to assess physical stability by examining key factors such as droplet size, phase separation and droplet charge. Care is needed in the understanding of each parameter. I see a strong tendency to create “non-meaningful” indices

to quantify the differences between samples and to relate them to different behaviours. If such indices are being used it is necessary to understand what they represent and their physical interpretation.

As I point out in my review article [17], such indices could be useful for comparison between samples. However, as they are not direct measures of stability, they should not be applied and compared among different studies with different conditions. There are great room for improvements for increased standardization. Some issues that are particularly problematic are for example different storage times for assessing CI, ES, EC and CI\*, different SDS concentrations when evaluating FI, and volume average or surface average diameters in the measure of droplet sizes. Most prominent are DLS measurements. There are many occasions where a single value for hydrodynamic droplet size is reported without taking into account polydispersity and size distributions, non-spherical shapes, mixes of materials (such as different proteins) or multi component systems (such as oil and protein) with different scattering contrasts, measurement errors such as multiple scattering or even specifying if the size is a radius or diameter. Figure 21a shows an example of how one can plot the same data in three different ways based on number, intensity or volume weighted distributions of hydrodynamic radius.

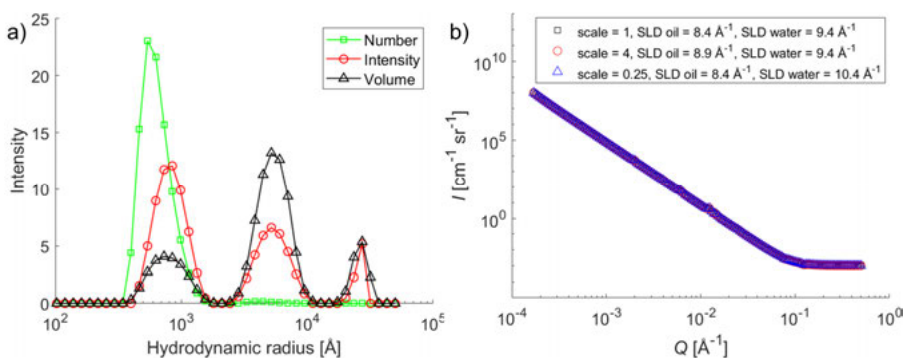


Figure 21. a) Results from dynamic light scattering experiments of a dispersion with pea protein isolate. Size distributions vary depending on how the averaging has been done. These data are an example of how quoting a single number for hydrodynamic radius can sometimes be misleading. Note that the hydrodynamic radius is in Ångström, whereas most DLS results are reported in nanometres. b) Plot of a scattering model, showing that the intensity is proportional to both the scale factor and SLD contrast between components. This highlights the importance of absolute intensity in model fitting.

The intensity weighted distribution is the primary result obtained from a DLS measurement and is, to first order, proportional to the sixth power of the particle radius ( $I \propto r^6$ ). Therefore, it highlights the larger particles. The number weighted distribution is the relative proportion of the number of objects of different sizes and emphasizes the smallest particles. The volume weighted

distribution is the relative proportion of the total volume of different sized objects and is typically a compromise of the number and intensity distributions. It is also important to remember that although the number and volume weighted distributions are very useful to understand the material, they are based on some assumptions about for example sphericity.

It is often also not clear how to interpret the indices, for example  $CI^*$  and  $FI$  are both concerned with changes of droplet size but not directly with the physical process that is causing the change. It is not always intuitive how to interpret the indices, as for apart from a value of zero ( $CI$ ,  $FI$ ,  $CI^*$ ) or one ( $ES$ ,  $EC/EA$ ) that is a “stable” sample, it is not clear how a different value would translate to stability. The main limitation is the difficulty to compare values between different samples, instruments and experimental procedures. These techniques are therefore best suited to acquire knowledge of the qualitative picture of a system and to obtain an initial understanding of the structure.

Particularly with microscopy, it is easy to obtain a qualitative understanding of the system but more difficult to quantify exact structures and stabilization mechanisms. Since microscopy data is collected for only a small part of a sample, single micrographs containing only a few objects may be misleading if not compared with other images, particularly for polydisperse samples. Nonetheless, such techniques are useful to restrict the choice of models for other quantitative techniques or to communicate findings to a broad audience as the visuals are good.

### 3.6 Summary of challenges and opportunities in assessing emulsion structure

Measurements of SAXS and USAXS were made with a laboratory instrument from Xenocs in Uppsala, Sweden, but also compared to results from an instrument by Anton Paar in Graz, Austria. The accessibility to the instrument in Uppsala has been of great importance for this study. The main drawback with a laboratory instrument is the relatively long measurement times (a few hours) particularly for the USAXS measurements and the limitation of sample environments.

Additional synchrotron X-ray measurements with *in situ* rheology were performed at the ESRF in Grenoble, France. The measurement times of fractions of seconds are greatly advantageous to measure a large number of samples. Neutron scattering is only accessible at such large-scale facilities. Not only is it necessary to apply for beamtime long time (months) in advance, it is an expensive technique and the measurement times are longer than for X-rays due to the lower neutron flux. Despite these challenges, the benefit of neutron scattering techniques to use contrast variation is of great importance. Neutron scattering has been performed at the Paul Scherrer Institute (PSI) in Zurich,

Switzerland, at the Australian Nuclear Science and Technology Organisation (ANSTO) in Sydney, Australia, and at Delft University of Technology (TUD), Delft, the Netherlands.

During synchrotron beam time, one can easily obtain large volumes of data. This is good, however, requires both a good file structure and log book and the analysis can sometimes be overwhelming with a large number of data sets. There is a possibility for the future to integrate artificial intelligence (AI) tools more widely in analysis of scattering data and planning of experiments. However, there are some apparent issues that needs to be resolved in order to take this route. First, improvements are needed regarding file formats, data reduction procedures and data treatment. The scattering community is working collaboratively to resolve these issues, however, there seems to be a slight tendency within the field to align with one's own ideas and write new software. It is not trivial for a non-expert to enter this field or to use AI for standardised data processing. There is motivation to work on both a standardized data presentation and to find systems to work with large volumes of data.

Another field where AI has great potential is in the assistance with model fitting. However, as with the standardization of data, the quality of measurements varies and many times data are not presented on an absolute scale, even in peer-reviewed journals, which makes calculation of volume fractions and contrasts very difficult and hinders validation of model fits. A simple example of how the scattering from a sphere is proportional to the scale factor,  $\phi$ , in the same way as to the square of the scattering contrast,  $\Delta\rho$ , according to the equation in subsection 3.2.4.1, is shown in Figure 21b.

When it comes to model fitting, correct estimation of error bars and resolution are of great importance and these are sometimes difficult to quantify. Different types of errors may arise from experimental setup, sample preparation and detector elements. Similarly, the resolution functions are not always easy to measure directly but require some estimates. For example, desmearing of USAXS data causes unrealistic error bars and slit smearing resolution depends strongly on slit length, beam divergence and beam profile. There is a lot of on-going work to address these issues, and there is room for improvements to fully use the potential of these techniques.

### 3.7 Summary of challenges and opportunities in assessing emulsion rheology

Conducting rheology experiments requires careful consideration of instrumental factors. For example, the gap size in a plate-plate or a plate-cone geometry needs to be chosen as to be significantly greater than the characteristic length scales of the components in the material investigated. Droplets of micrometre sizes in emulsions would typically require a gap of the order one

millimetre. Another challenge in rheological measurements is wall slip, which can occur in different measurement geometries and may effectively lead to an underestimation of the true stress. To avoid this effect, the experiments in this work were carried out with rough surfaces. The measurement conditions are important to report, as it is not always possible to compare results measured with different setups even for the same sample. An additional concern in long measurements is water evaporation, which effectively increases the sample concentration and hence change the rheological properties. This problem is commonly solved by using a water trap around the sample providing a controlled humidity environment.

It is easy to understand the motivation to study rheological properties of materials, as these properties are highly relevant for material performance and perception of end consumers in various fields. Several quantities such as viscosity, elastic and viscous moduli, yield stress and phase angle can be measured directly, and rheological experiments can also generate indirect scientific knowledge of for example structures of materials. This is one reason for defining various indices and dimensionless parameters to be able to compare the rheological properties of different systems.

For emulsions and particularly the emulsion gels studied in this work, the rheological behaviour is determined by both the droplets, the interfacial phenomena and the viscoelastic properties of the continuous phase. One common dimensionless index relevant to this system is the capillary number,  $Ca$ , describing the ratio between viscous stresses on the droplets and the stress associated with the interfacial tension,  $\sigma_T$ . One of the definitions of this index is given by [73]:

$$Ca = \frac{\eta_c \dot{\gamma} R_o}{\sigma_T}$$

where  $\eta_c$  is the viscosity of the continuous phase,  $\dot{\gamma}$  is the applied shear rate and  $R_o$  is the droplet radius. A value less than one corresponds to a sample where stresses from interfacial tension is dominant ( $\sigma_I = \sigma_T/R_o$ ), and a value greater than one favours viscous stresses ( $\sigma_V = \eta_c \dot{\gamma}$ ). This index can be written in many different ways, as seen in a review that reports 41 different capillary numbers [74]. While such indices are easy to report, their interpretation requires understanding of assumptions made and the definitions of the parameters, which is not always trivial.

Similar challenges arise in models to fit the data. Many models contain parameters that lack direct physical interpretation and can be tuned to match the data, and sometimes additional scale factors are also introduced. For example, the Hershel Bulkley equation (subsection 3.3.1) includes a consistency index tuneable to match data, and the Krieger-Dougherty model (subsection 3.3.1) assumes rigid spheres dispersed in a medium with uniform viscosity.

For systems with a protein network in the continuous phase, it is not trivial to determine an appropriate value for the continuous phase viscosity.

Overall, there are many ways to report rheological results. There are a wide variety of measurement protocols and measurable quantities, which makes direct comparison between studies challenging. Many quantities such as stress, strain, viscosity, storage and loss moduli and phase angle are related and can often be obtained from the same original data. Choosing which values to present can strongly influence how one perceives the properties of a material.

## 4. Identification of stable emulsion compositions

### 4.1 Mapping stability regions in pea protein stabilized emulsions

The review article [17] investigated the majority of the published work on pea protein stabilized emulsions up to 2022. Different studies were compared and two regions of stability for different emulsion compositions (water, oil, protein) were identified, as seen in the ternary diagram in Figure 22a. In this analysis, a sample was classified as stable when the authors reported stability based on comparative observations over time. This could include techniques such as light scattering (subsection 3.1.1), macroscopic and microscopic visual observation (subsections 3.1.4 & 3.1.5) or measurements of sample turbidity (subsection 3.1.1). The time range could vary significantly between a few hours to multiple weeks. The corner points in the ternary diagram represent samples with 100% v/v oil (left), 100% v/v water (right), and (100% of a dispersion with) 25% w/v protein in water (top). The “protein” corner is defined as 25% w/v protein in water (25 g/100 mL). This concentration was chosen simply as a graphical reference point to provide an appropriate axis scaling to improve the visual position of compositions in the ternary plot. It does not imply that emulsions were prepared by first preparing such dispersions of proteins, but is used only for plotting purposes. Each point contained within this triangle represents a sample that contains a mixture of oil, water and this reference protein/water dispersion, and hence the effective protein concentration for any point is obtained by scaling relative to the 25% w/v corner. The green area in the lower left corner in Figure 22a corresponds to high internal phase samples with 60-90% v/v oil and total protein concentrations less than 2.5% w/v. The second, larger area of stable compositions, is located in the lower right corner and corresponds to 5-30% v/v oil and protein concentrations up to 9% w/v. The red squares in this diagram represents emulsions that were reported as unstable over various time periods.

These results caught my attention, suggesting that pea protein is a promising emulsifier, but also raised questions about stability mechanisms and the stability in unexplored areas of this phase map. First, the wide range of stability in two separate regions implied that perhaps different stabilization mechanisms dominate depending on composition. The literature search

presented in the review article [17] also found that protein history, such as extraction methods and processing, was important. These treatments were observed to have a greater impact than type of vegetable oil or homogenization method.

A broad compositional area at intermediate oil and high protein concentrations remained unexplored. This observation motivated the work presented in paper I, which systematically investigated emulsion stability across a wider range of compositions using a single pea protein material.

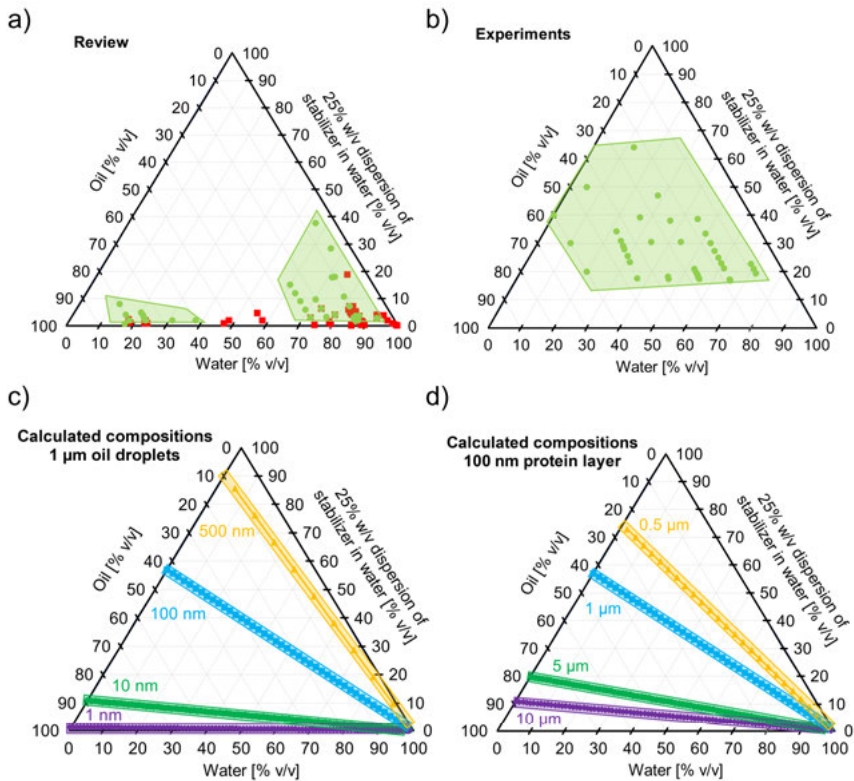


Figure 22. Stability ternary diagrams. a) Stable (green circles) and unstable (red squares) compositions reported in literature [17]. b) Additional stable compositions found in my experiments reported in paper I. c) Calculated compositions assuming 1  $\mu\text{m}$  droplet radii for various thicknesses of protein at the droplet surface of 1 nm (purple diamonds), 10 nm (green circles), 100 nm (blue squares) and 500 nm (yellow triangles). d) Calculated compositions assuming 100 nm protein layer thicknesses for various droplet radii of 0.5  $\mu\text{m}$  (yellow triangles), 1  $\mu\text{m}$  (blue squares), 5  $\mu\text{m}$  (green circles) and 10  $\mu\text{m}$  (purple diamonds).

## 4.2 Newly identified stable compositions

Paper I is devoted to investigating the range of stable emulsion compositions made with the commercial pea protein isolate described in subsection 1.2.2. Emulsions with various oil concentrations from 5 to 90% v/v and protein concentrations from 0.5 to 17% w/v were prepared. Visual observation of phase separation was monitored during seven days of storage and a region of stability that was previously unexplored was identified, as seen in Figure 22b. This region includes samples with approximately 10-60% v/v oil and 5-15% w/v protein.

The stable emulsions have a white, homogenous appearance after storage (Figure 3a). At lower protein concentrations, they showed quick phase separation into multiple layers within minutes to hours (Figure 23b), whereas at higher protein concentrations, sample preparation was not feasible due to the high volume fraction and viscosity in such concentrated systems. The identified region of stability was similar across a range of pH and for different mixing protocols, indicating that the stability was independent of both pH and mixing processes within the range investigated. Paper I includes ternary diagrams for samples at acidic (pH 3.0), isoelectric (pH 4.6) and neutral conditions (pH 7.0) (Figure 4 in paper I), as well as for samples prepared using either a homogenizer or a food blender (Figure S2 in paper I). The identification of this new stability region suggests that stabilization cannot be explained solely by interfacial adsorption of proteins.

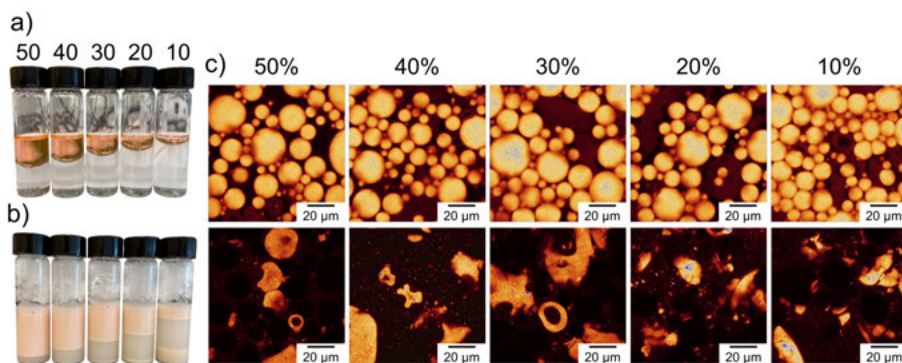


Figure 23. a) The initial fractions of oil (top layer) and water (bottom layer) before addition of protein and homogenization. From left to right 50 to 10% v/v oil. b) Phase-separated emulsions with 3% w/v protein after 48 h of storage in 19 °C. c) Confocal images of the upper creaming phase. Upper panel shows oil droplets, and lower panel shows proteins.

### 4.3 Limits of interfacial coverage stabilization model

The requirement of protein concentrations of 5% w/v or higher for stability in the newly identified region of stability is significantly more than required for a layer to cover droplets which would be the typical way of thinking about a simple emulsion stabilized by surface active materials (Figure 2). Even for relatively small droplets of 1  $\mu\text{m}$  that would have a large amount of surface area, a protein layer of 1-10 nm would require less than 3% protein for complete surface coverage. This is illustrated in Figure 22c.

If interfacial absorption was the sole determinant for stability, the boundary of the stable compositions would extend along a straight line in the ternary diagram representation with different gradients depending on the thickness of the interfacial layer. An example of this for droplets with 1  $\mu\text{m}$  radii and various layer thicknesses are seen in Figure 22c. Calculated compositions for a thick protein layer of 100 nm with various droplet sizes are seen in Figure 22d. Stability is observed in a broader area and with protein concentrations well above those required for even a thick layer at the surface. This cannot be described solely by a wide distribution of surface layer thicknesses or droplet sizes. The finding suggests that there are other stabilization mechanisms that are important for these systems and that excess protein plays a major role in determining emulsion stability. These mechanisms will be discussed in the following chapters.

## 5. Distribution and network formation of proteins in emulsions

### 5.1 Protein location at neutral pH

The understanding from paper I that only a fraction of the proteins is required to stabilize the oil-water interface and that substantial amounts of excess proteins are necessary for stability, drove further investigation of protein location within the emulsions. In papers II & III, the protein and oil droplets were stained with different fluorescent dyes and observed with CLSM to obtain a qualitative idea of where the protein is located. The images consistently showed that a large proportion of the proteins remain dispersed in the continuous aqueous phase, with only a thin interfacial layer at the droplet interfaces. Examples of confocal microscopy images of an emulsion are presented in Figure 9c & d.

Models to scattering data could give a more quantitative idea of both the distribution of proteins in the different locations (adsorbed to the surface, dispersed in the continuous phase, and aggregated in clusters) and the hydration. Initial interpretations based on SAXS and USAXS data in paper I suggested that thick and dense protein layers surround large polydisperse droplets. In these models, droplets with radii of the order  $16\ \mu\text{m}$  (SLD  $8.68 \times 10^{-6}\ \text{\AA}^{-2}$ ) were surrounded by protein layers with an apparent thickness of several hundred nanometres (thickness  $\sim 700\ \text{nm}$ , SLD  $12.0 \times 10^{-6}\ \text{\AA}^{-2}$ ). The additional approximately 70% of the total protein volume was described as a dispersion of polydisperse ellipsoidal aggregates with mean polar and equatorial radii of 4.1 and 24.0 nm, respectively. These had a slightly lower SLD than the protein adsorbed to the droplet surfaces. Both light scattering and optical microscopy results, presented in paper I, confirmed that proteins and droplets were highly polydisperse.

While such models with thick interfacial layers are physically plausible, both as a Pickering type stabilization, where the thickness of the adsorbed layer at the interface is aggregates of proteins, or as a more diffuse and hydrated layer of proteins with overlapping contributions from both interfacial and other aggregates close to the surface, CLSM images presented in paper II (Figure 5) & paper III (Figure 2) did not support the presence of a thick interfacial layer. Contrast variation in SANS experiments in paper II was used to refine the scattering model.

## 5.2 Proteins form networks in the continuous phase

By using contrast variation in SANS experiments (paper II), additional insights were gained regarding the contributions from oil and proteins alone to the scattering patterns. Seven different SLD of the solvent from 4.5 to 37.9% v/v D<sub>2</sub>O were measured, which are shown in Figure 24a.

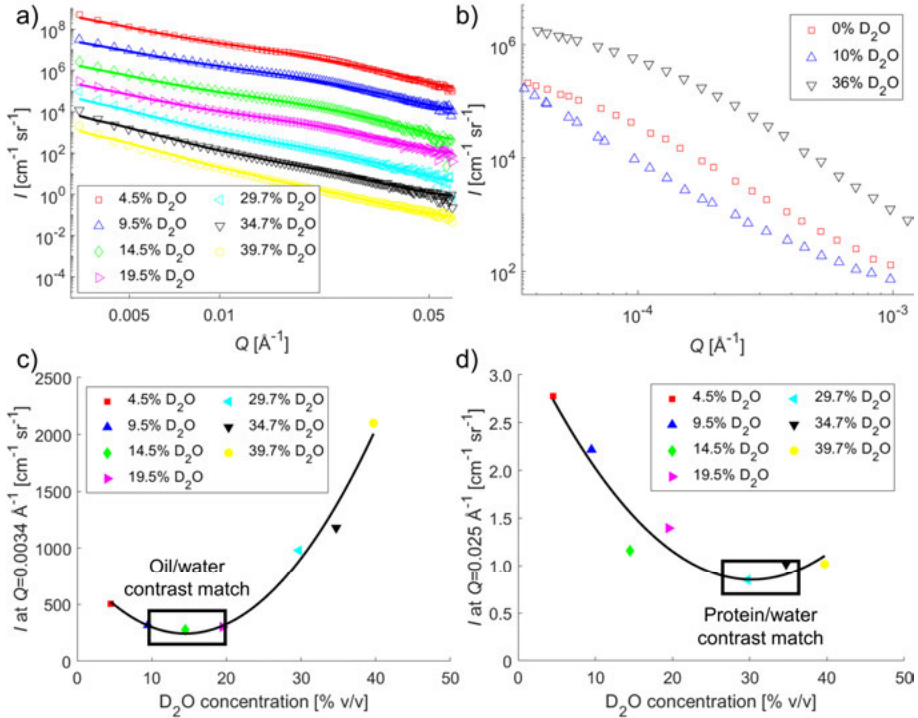


Figure 24. a) SANS data from PSI of an emulsion with 40% v/v oil and 7.5% w/v protein at seven different solvent SLD (4.5 to 39.7% v/v D<sub>2</sub>O). The curve with 39.7% D<sub>2</sub>O is to scale, the other curves are shifted by factors of 10<sup>1</sup> to 10<sup>6</sup> for visibility. The solid lines are fractal and sphere model fits from paper IV. b) Smear USANS data from ANSTO of an emulsion with 50% v/v oil and 10% w/v Smeared at three different solvent SLD (0 to 36% v/v D<sub>2</sub>O). c) Estimation of the oil/water contrast match point by comparing the intensity at  $Q = 0.0034 \text{ \AA}^{-1}$  for the samples with different solvent SLD in a). d) Estimation of the protein/water contrast match point by comparing the intensity at  $Q = 0.025 \text{ \AA}^{-1}$  for the samples with different solvent SLD in a).

The oil/water contrast match point could be estimated by a minimum in intensity at a low value of  $Q$  (Figure 24c). However, even at conditions where the SLD of water (9.5% v/v D<sub>2</sub>O) is closely matched to that of oil (SLD  $\sim 0.1 \times 10^{-6} \text{ \AA}^{-2}$ ), the intensity around the lowest  $Q$  values measured in this experiment (extending down to  $3.4 \times 10^{-3} \text{ \AA}^{-1}$ ) remains high. Combined with the observations from CLSM, which showed an extended protein network within the continuous phase, this indicated that the excess protein could be more

accurately described as a fractal system extending to large network structures, rather than existing as isolated ellipsoidal aggregates. The fractal model in paper II consists of individual protein building blocks (radius  $\sim 6.1$  nm) self-repeating to large aggregates (characteristic sizes) of at least  $0.1 \mu\text{m}$ . However, due to the limitation in  $Q$ , the aggregate size was seen as a lower limit of size that could be larger, and this was one motivation for the SESANS studies in paper IV.

Model fits to SANS data at the seven different solvent contrasts ( $\text{D}_2\text{O}/\text{H}_2\text{O}$  ratios between 0.05 to 0.66) showed that the SLD of the protein changed linearly with  $\text{D}_2\text{O}$  concentration (Figure S2 in paper IV). The change was significantly greater than that expected from the exchange of hydrogen to deuterium in the solvent alone [44]. The gradient of how the SLD of the protein vary with the SLD of the solvent suggests that the protein in the continuous phase is highly hydrated ( $\sim 75\text{-}80\%$  water).

Scattering in the intermediate  $Q$  region where  $0.01 < Q < 0.05 \text{ \AA}^{-1}$ , showed a shoulder. The intensity of this feature scales with protein concentration and was observed in both emulsions (Figure 25a) and dispersions. This was also seen in SAXS experiments (Figure 7b in paper I). The scattering patterns of emulsions and protein dispersions without oil were nearly identical when normalized to the protein volume fraction (Figure S3 in paper II). This confirmed that the signal in this region of  $Q$  originates from contributions from dispersed proteins in the continuous phase rather than from protein adsorbed at the oil-water interface.

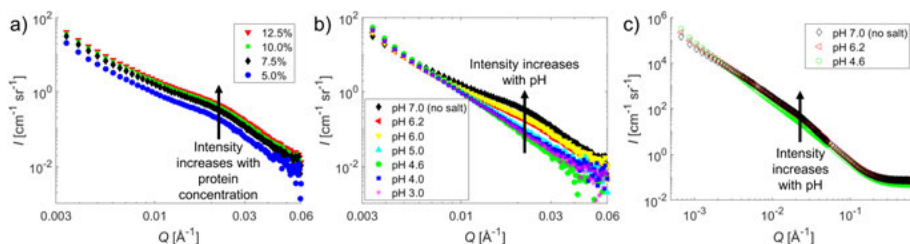


Figure 25. a) SANS data measured at PSI of various pea protein concentrations for emulsions with 40% v/v oil and 10% v/v  $\text{D}_2\text{O}$  in the solvent. The intensity is proportional to the protein concentration in the continuous phase. b) SANS plots of data collected at PSI of emulsions with 40% v/v oil, 7.5% w/v protein and 10% v/v  $\text{D}_2\text{O}$  in the solvent at various pH. The intensity around  $Q = 0.025 \text{ \AA}^{-1}$  increases with higher pH. c) SANS data measured at ANSTO of 15% w/v pea protein dispersions at various pH with 100%  $\text{D}_2\text{O}$  in the solvent. The intensity around  $Q = 0.025 \text{ \AA}^{-1}$  increases with higher pH.

Scattering data in this region were well described by a model based on an average form factor for the proteins. The lack of pronounced features from structure factors indicates that contributions from interparticle correlations are not significant in this  $Q$  range as these would give rise to (broad) maxima. The protein/water contrast match point was estimated based on the scattered

intensity in this region as can be seen in Figure 24d. A further example of where different contrasts were used to match out the contributions of oil (10% v/v D<sub>2</sub>O) and proteins (36% v/v D<sub>2</sub>O), respectively, is shown in Figure 24b. In this USANS region of small  $Q$ , the protein/water contrast match condition gives a significantly higher intensity as expected for scattering dominated by oil droplets than at the oil/water contrast match condition where mainly contributions from clusters of proteins are seen.

SESANS experiments on both emulsions and dispersions in paper IV were performed to complete the structural picture of the systems. This technique probes length scales beyond those accessible by SAXS and SANS, similar to those in USANS. A dispersion with 15% w/v protein was measured at two different contrasts of 100% H<sub>2</sub>O and 100% D<sub>2</sub>O in the water (Figure 2 in paper IV). A continuous increase in the magnitude of the measured signal confirmed that protein networks extending to several micrometres are present. The emulsions can be described as oil droplets dispersed within a gelled matrix, i.e., a continuous aqueous phase containing a high concentration of non-adsorbed proteins. Increasing the protein content gives higher concentrations of protein in the continuous phase, which gives rise to a denser network that effectively prevent droplet-droplet contact. This is associated with smaller droplets and results in greater stability against phase separation. The SESANS results shown in Figure 26a for emulsions with various oil concentrations show that the signal is clearly weaker for samples with higher oil fractions that have smaller droplets. For these systems, the stability is not determined by the interfacial layer thickness, but rather the protein network elasticity and viscosity in the continuous phase. The rheological properties of the continuous phase are crucial in limiting creaming, coalescence and phase separation.

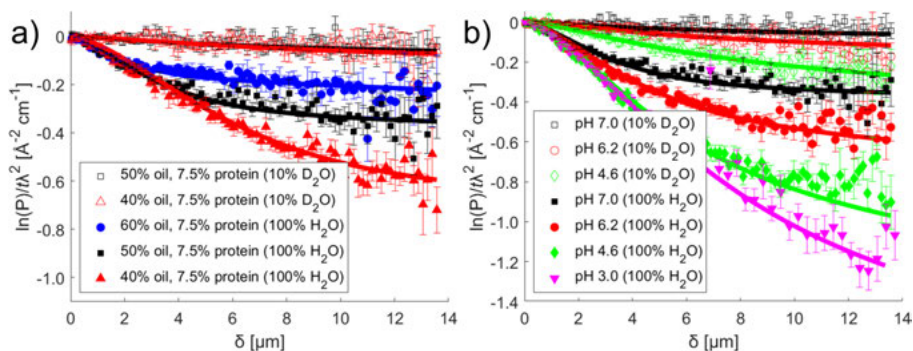


Figure 26. SESANS results of emulsions at two different solvent contrasts of 10% D<sub>2</sub>O + 90% H<sub>2</sub>O (oil/water SLD match) and of 100% H<sub>2</sub>O. a) Samples with 40-60% v/v oil and 7.5% w/v protein at pH 7.0. b) Samples with 50% v/v oil and 7.5% w/v protein at pH 3.0 to 7.0. The stronger signal for the samples at lower oil fractions and lower pH for the same contrast indicates that larger structures are formed in these samples.

### 5.3 Effect of pH and buffer salt on protein aggregation

Expanding the scope to cover emulsions prepared with a continuous phase that contains sodium citrate buffer (0.1 M) at pH 3.0 to 6.2, the protein behaviour is observed to change. This is particularly prominent in the scattering region  $0.01 < Q < 0.05 \text{ \AA}^{-1}$  of both dispersions (Figure S1b in paper II) and emulsions (Figure 3 in paper II). Plots of how the intensity decreases at lower pH for emulsions and dispersions are presented in Figure 25b & c. The contribution to the intensity in this region arises from the dispersed proteins (individual building blocks in the fractal model). Initially, the lower intensity at acidic pH was assumed to be related to unfolding of the proteins from the more compact and folded state at neutral pH. The fraction of proteins showing unfolding (which would lead to consequent aggregation) was proposed to be related to the intensity in this region (Figure S3 in paper II), although no direct modelling was performed at this stage. Confocal microscopy images of dispersions and emulsions are presented in Figure 27 and show that larger protein structures are present at low pH.

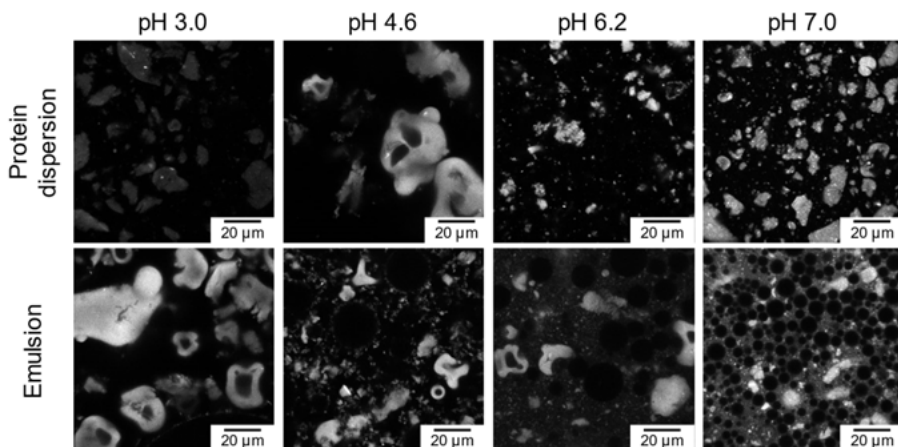


Figure 27. Confocal micrographs of 15% w/v protein dispersions (upper panel) and emulsions (lower panel) with 50% v/v oil and 7.5 w/v protein are shown, where 4-DASPI is used to visualize the signal from proteins. Intensity is given on a gray-scale from black to white. The proteins show more aggregation at pH 3.0 and 4.6 compared to near neutral pH.

In paper IV, the change with pH was further explored. A Guinier-Porod model was used to describe the scattering from protein aggregates in samples at acidic pH. It is possible that the dominant factor for the aggregation occurring at acidic pH could be related to reduced protein solubility in a citrate buffer rather than protein unfolding. Citrate ions are multivalent, hydrated anions

that may act as kosmotropes, reducing the solubility of the protein, and promoting protein aggregation. However, the change in pH combined with added citrate buffer makes it difficult to distinguish between the effects of pH and specific ion effects. The SESANS technique was able to detect substantially greater aggregates with rough surfaces for the samples at lower pH, including both dispersions (Figure 6 in paper IV) and emulsions (Figure 26b). In the emulsions, this was associated with larger droplets at lower pH, which contributed to the greater SESANS signals for these samples. Both droplet and overall protein aggregate size hence increased upon lowering the pH. Despite the differences in droplet size and protein behaviour, the stability remained remarkably consistent across pH as shown in Figure 4 in paper I.

In USANS experiments, dispersions at acidic pH showed similar shapes in scattering patterns but consistently higher intensities than samples at neutral pH. This confirms that they contain a higher fraction of large aggregates, consistent with the findings from SESANS. Emulsions, on the other hand showed interesting behaviour depending on the contrast matching conditions in USANS experiments. When the protein and water were contrast matched, the intensity was greater for samples at neutral pH, whereas when the oil and water were contrast matched, the intensity was greater for samples at lower pH. These observations give clear evidence that droplets have a larger size (less specific surface area) and that the fraction of protein aggregates is greater (higher volume fraction) at lower pH.

## 5.4 Temperature effects on proteins

Temperature effects on protein structure and emulsion stability were generally small for both emulsions and dispersions of protein up to the investigated temperature of 90 °C (Figure 28). The main change in scattering pattern occurred around the broad shoulder ( $Q \sim 0.025 \text{ \AA}^{-1}$ ). This signal was attributed to the protein in the continuous phase. Increasing temperature showed a slight decrease in intensity at this peak and a shift towards lower  $Q$  (Figure 28b). This response is qualitatively similar to the observations when the pH is reduced (Figure 25b & c), but the magnitude is smaller. The shift in peak position corresponds to a small increase in characteristic lengths in real space. This effect was non-reversible when the temperature was readjusted back to 22 °C. In contrast, samples prepared at acidic pH showed no change in scattering profiles in this region upon heating, indicating that the low solubility and protein aggregation are affected more by pH than by thermal treatment.

In the USANS region, corresponding to larger correlation lengths, temperature induced changes were more difficult to interpret. For dispersions of protein without oil, heating from 22 to 80 °C gave no change in scattering patterns, suggesting that the protein aggregates in a continuous phase are not significantly changed by an increase in temperature. The emulsions showed

some change with temperature as seen in Figure 28a, but more work is needed to resolve the details of this process.

On a macroscopic scale, no phase separation was observed after a cycle of heating to 90 °C and cooling back to 22 °C. Within this investigated temperature range, the thermal stability was very promising for food processing applications, as this cycle of heating and cooling did not induce phase separation. Thermal energy did not substantially change the protein interactions forming the aggregate and network structure in these systems. For real-world applications, this would effectively mean that cooking with pea protein stabilised emulsions does not change the protein structure, the oil droplet size or the overall stability. The limited response to heating indicates that thermal effects do not play a major role compared to pH and protein concentration in regards network formation and emulsion stability. However, this could be specific to the processing conditions of this particular pea protein isolate. The thermal stability is also consistent with the conclusions that the properties of the continuous phase with dispersed proteins are most important for emulsion structure and stability.

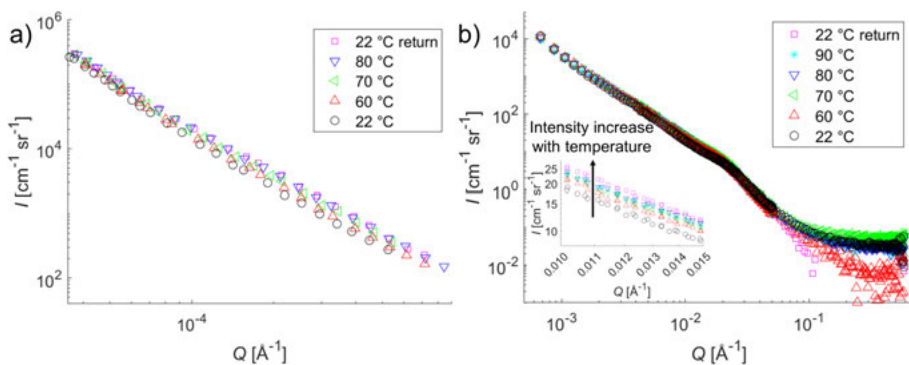


Figure 28. Temperature effects on an emulsion with 50% v/v oil and 10% w/v protein at pH 6.2. a) USANS plot with a temperature ramp between 22 and 80 °C and back to 22 °C. b) SANS plot with a temperature ramp between 22 and 90 °C and back to 22 °C. The intensity around  $Q \approx 0.013 \text{ \AA}^{-1}$  is increasing due to a shift in the broad shoulder with higher temperatures and the process is irreversible.

## 6. Physical properties with excess protein in the continuous phase

### 6.1 Rheological consequences of gelation

The combined results in papers I to V show that emulsions with high pea protein concentrations contain a substantial amount of protein in the continuous phase. This protein is effectively governing the physical properties in terms of viscosity and stability. The emulsions showed typical shear-thinning behaviour (Figure 29a).

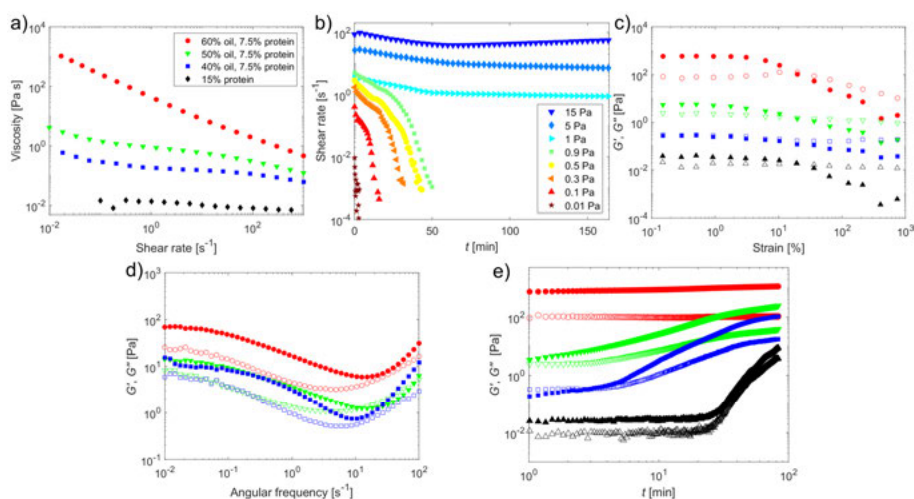


Figure 29. Rheological behaviour of emulsions and dispersions of proteins. a) Flow curve of how the viscosity vary with applied shear rate (measurement protocol described in subsection 3.3.1). b) Constant applied shear stresses between 0.01 to 15 Pa where the shear rate is monitored over time (subsection 3.3.2) for an emulsion with 40% v/v oil and 7.5% w/v protein. c) Strain amplitude sweep (subsection 3.3.3) of the response of the storage and loss moduli with varying strain. d) Frequency sweep (subsection 3.3.4) of the response of the storage and loss moduli with varying angular frequency. e) Constant applied low strain amplitude and angular frequency, and the storage and loss moduli are measured with time (subsection 3.3.5). Filled symbols represent  $G'$  and open symbols are  $G''$  in c), d) and e). Samples in a), c), d) and e) are given by the legend in a).

The hydrated fractal protein clusters act as fillers surrounding the oil droplets and strongly increase the overall viscosity. According to the findings in paper I (Figure 8b & c in paper I), the relative increase in viscosity with protein concentration is approximately twice as that expected from the Krieger Dougherty equation due to the added volume of dry protein isolate. This finding is important to understand the great emulsion stability. The high viscosity suggests that the interacting proteins form a network structure and occupy more effective space than simply the volume added. This is consistent with the high protein hydration described in papers II & IV.

A thorough investigation of the rheological properties in paper III revealed a yield stress even at concentrations below the maximum packing fraction (Figure 29b). A yield stress was observed also for protein dispersions in pure water without oil and this confirmed that gelation was due to protein interactions rather than clusters of oil droplets. This behaviour was observed above a critical gel forming protein concentration. The presence of a yield stress explains why such high protein concentrations of more than  $\sim 5\%$  w/v is required for good emulsion stability. A high viscosity slows down the motion of droplets, but does not completely prevent rearrangements from small stresses such as gravity. When a yield stress is present, it hinders the movement of droplets below a certain applied stress, and thus strongly aids in the long-term stability.

Further rheological characterization using strain amplitude sweep, frequency sweep and low strain amplitude and frequency tests (Figure 29c-e) provided additional evidence of the viscoelastic nature of the protein network structure. An LVR was observed at low strain amplitudes in Figure 29c and a crossover point between  $G'$  and  $G''$  was seen at higher strain amplitudes. In the frequency sweep in Figure 29d,  $G'$  was consistently higher than  $G''$ , confirming the network structure.

## 6.2 Gelation is affected by high shear

Excess protein in the continuous phase is crucial for emulsion stability as it gives rise to gelation and a yield stress, however, some changes to the gelled network occur when shear is applied. Paper V investigates how the emulsion structure and rheology, and particularly the droplet size, is affected when shear is applied. Application of a continuous high shear rate ( $1000 \text{ s}^{-1}$ ) leads to a reduction in shear stress and viscosity over time (Figure 4a in paper V), indicative of partial network disruption. By simultaneous SAXS measurements, droplet elongation and alignment of proteins could be investigated, however, even at such high shear rates, the emulsion droplets and protein structures remained isotropic (Figure 5 in paper V). In fact, the only changes in scattering with shear were an increase in intensity with time at low  $Q$  and a curvature at the lowest  $Q$ . Without noticeable anisotropy, the mechanism for these effects,

in a  $Q$  range dominated by surface scattering (Porod region) and overall shape (Guinier region), is breakage of large droplets that creates more surface area. The increased intensity was not fully reversible when the shear rate was reduced ( $0.01 \text{ s}^{-1}$ ). This observation is consistent with the increase of viscosity and shear stress when the shear rate was reduced (Figure 6a in paper V).

The exceptional shear stability and lack of significant droplet elongation is attributed to the high interfacial tension and low stress under high shear. This combination gives a low capillary number, which is characteristic of droplets remaining intact rather than elongating in the flow direction. A high shear rate can be thought of as similar to the preparation process such as homogenization of a sample, where the droplet size is being reduced. At a low shear rate, or at rest, a sample is stable against droplet coalescence and emulsion separation, and therefore, the process of breakage of droplets under high shear is irreversible.

### 6.3 A favourable emulsion composition

The emulsions that showed complete phase separation at rest were characterized by a creamed top layer and an aqueous bottom phase (Figure 23b). A fascinating observation was that the creamed phase had a similar internal composition regardless of the initial water/oil/protein fractions. This phase was investigated by CLSM (Figure 6 in paper III), SAXS/USAXS (Figure 7 in paper III) and density measurements (Figure S14 in paper III). Example microscopy data of the upper creaming phase for phase separated emulsions are presented in Figure 23c. The oil fraction was approximately 50% v/v despite the original concentration that varied between 10 and 50% v/v. The findings indicate that there is almost a state of equilibrium giving rise to the fixed composition rather than only kinetic stability. This observation is explained by the ideas from papers II, III & IV that the stability is highly dependent on the properties of the continuous phase. With sufficiently high concentrations of excess protein in the upper phase, a protein network is formed that gives a yield stress even below the maximum packing fraction. This prevents rearrangement and coalescence of droplets.

The value of 50% v/v oil fraction appears to be almost an equilibrium when oil droplets are trapped within the protein network. At lower oil concentrations, the buoyant force of oil droplets of lower density compared to the water and protein continuous phase drives the creaming. This state is perhaps best described as a mechanically stable packing rather than a true thermodynamic stability. Nonetheless, it strengthens the argument that much of the stability is governed by the rheological consequences of gelation in the continuous phase rather than interfacial coverage alone.

## 6.4 Dynamic constraints by the protein network

The dynamics of the emulsions on microscale were investigated by XPCS. In paper V, this technique was used to determine which constraints the protein network imposes on the oil droplets in a sample at rest. The intensity auto-correlation functions, fitted by the KWW equation, decay faster at higher  $Q$  (Figure 7a in paper V), meaning that smaller structures relax quicker than larger ones. For purely diffusive motion, the relaxation rate is expected to scale as  $1/\tau_c = D_T Q^2$ . However, the relaxation rate could not be described by a single translational diffusion coefficient over the full  $Q$  range (Figure 7b in paper V). It did not show simply a clear diffusion process but the relaxation likely arises from some other fluctuations in the gel network or interfacial membranes. At small  $Q$ , corresponding to large distances, the gradient was shallow ( $D_T \approx 4.7 \times 10^{-14} \text{ m}^2 \text{ s}^{-1}$ ), and at large  $Q$ , the diffusion coefficient was larger ( $D_T \approx 150 \times 10^{-14} \text{ m}^2 \text{ s}^{-1}$ ). The exact values depend strongly over which range of  $Q$  these gradients were taken. It is likely that the gradient at small  $Q$  is related to some fast motion of droplets that is constrained by the protein network.

The different mobility on different length scales could be related to the hierarchical nature of the protein network, or at least to the heterogeneity of the network. A stretching exponent was fitted in the KWW equation and it is found to decrease with increasing  $Q$  (Figure 7c in paper V). This means that the distribution of relaxation times is broader at smaller length scales (larger  $Q$ ). The heterogeneities vary more at smaller scales, and one can speculate that this is because of different types of proteins with different behaviour such as hydration and aggregation. The XPCS studies on this system provide some interesting results, confirming the constraints in mobility that the protein imposes on the oil droplets. Further experiments and data analysis, particularly at shorter relaxation times and for a range of samples, both emulsions and protein dispersions, would be useful to understand the exact dynamics and diffusion processes in these types of samples.

## 7. Generalization of stabilization mechanisms in plant-based emulsions

This dissertation is primarily focused on emulsions stabilized by pea proteins, but an interesting question is whether the stabilization mechanisms, the structural features and the scattering patterns identified are unique to emulsions with pea proteins or if the knowledge can be transferred to other plant-based systems containing excess biopolymers in the continuous phase. Paper VI addresses this question by comparing the composition, structure and characteristic features of X-ray scattering of 29 commercially available emulsions prepared with different plant-based materials in comparison to dairy products used in similar applications. The plant-based materials investigated include almond, coconut, fava bean, linseed, oat, pea, rice and soy. Examples of an oat based 'cream' product, a soy based 'milk' product and a dairy cream used in similar applications are shown in Figure 30d. This study shifts the focus from the idea of investigating pea proteins as a specific case to determining if the findings can be applied more generally to a broader range of materials.

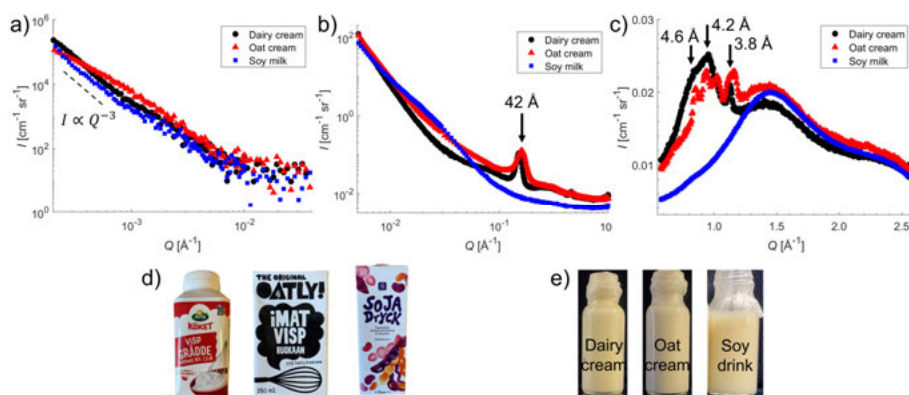


Figure 30. Examples of samples studied in paper VI, including dairy cream, oat cream and soy milk. a) Slit smeared USAXS data showing a gradient close to  $Q^{-3}$ . b) SAXS data showing a first order lamellae peak at  $Q$  of  $0.15 \text{ \AA}^{-1}$  corresponding to  $42 \text{ \AA}$ . c) WAXS data showing correlation peaks at several  $Q$  values. d) Images and e) visual appearance of the commercial products investigated.

In the samples investigated, the total content of biopolymers (carbohydrates and proteins) ranged between  $0.1\% \text{ w/w}$  and  $15.3\% \text{ w/w}$ , with a mean of  $7.3\%$

w/w (Table 2 in paper VI). These values are of the same order as those in the work on pea protein stabilized emulsions in papers I to V. However, the total fat content ranged between 1.0 and 36% w/w, which is significantly lower than for the emulsions discussed in previous chapters.

X-ray scattering (USAXS, SAXS & WAXS) was used to investigate these systems. Plots for selected samples are presented in Figure 30a-c. Correlations were seen between intensity in particular regions of  $Q$  and both total fat content and carbohydrate content. For example, a correlation between the carbohydrate content and the intensity at  $Q = 0.10 \text{ \AA}^{-1}$  was identified (Figure 2d in paper VI). At higher concentrations, carbohydrate and proteins are located mainly in the continuous phase and this characteristic size is not very different from that of the material giving rise to the intensity in the broad shoulder that was observed in the pea protein stabilized emulsions around  $Q \sim 0.025 \text{ \AA}^{-1}$ . However, it is not possible to fully conclude whether the stabilization mechanism for these samples is dominated by the non-adsorbed materials in the same way as for the pea protein stabilized emulsions in papers I to V as the rheological properties of these samples were not measured. This was identified as a future area of interesting work.

Directly observable in SAXS as a peak at  $Q = 0.15 \text{ \AA}^{-1}$  (Figure 30b) was scattering from crystalline fats and the intensity was proportional to the fat content (Figure 2c in paper VI). A high fraction of solid fats, derived mainly from hydrogenated fats, was only found in products with creamy textures, such as those designed for 'cream' or 'yoghurt' applications. The addition of solid fats is an alternative approach to increase viscosity, rather than adding extra protein as in the pea protein stabilized emulsions in papers I to V. The consumption of large amount of solid fats are debated as nonbeneficial through a health perspective [75, 76]. The finding of network stabilization in the pea protein stabilized emulsions described in previous chapters could lead the way for simply increasing carbohydrate and protein contents to achieve similar rheological properties while, at the same time, decreasing the solid fat content.

An indication that the stabilization mechanism, to some extent, is different in these systems is the increase in droplet radii with total fat content (Figure 2a & b in paper VI). This is consistent with the conventional behaviour of interfacial mechanisms contributing to stability that is typical for emulsions. With limited emulsifier materials that can only cover a finite droplet interfacial area, higher fat content would lead to larger droplets. In contrast, for the pea protein stabilized emulsions, the stability is dependent on the continuous phase mechanisms.

One difficulty that was identified with pea protein stabilized emulsions, particularly by comparing a range of studies from the literature [17], was the variety in stability despite similar emulsion compositions (Figure 22a). Differences between the emulsions in paper VI prepared with the same raw material showed larger structural differences than what was observed between

different classes of materials. The observation confirmed the idea from the review [17] that droplet size, protein aggregation and structure in the continuous phase are strongly influenced by the environment, extraction method and thermal treatment. According to published literature [17], the protein history has a greater influence on emulsion stability than type of oil or mixing preparation, and it supports the idea that the findings from the pea protein system could be applied to a broader group of plant-based materials.

Excess biopolymers, such as proteins and carbohydrates, were present in the continuous phase for samples in paper VI, however did not always contribute in the same way as in the pea protein stabilized emulsions. To mimic the gelled systems produced with pea proteins, a higher effective concentration of these materials would likely be required to create a network in the continuous phase. This could be an interesting route forward to shift the focus from interfacial coverage as the primary stabilization mechanism and concentrate on the mechanical properties of the continuous phase. By careful choice of materials, nutritional balance and content could also be tuned.

## 8. Data representation and comparative analysis using colour maps

Paper VI contained scattering data from many different materials, not only to provide a database of plant-based materials to be able to compare to the pea protein system in papers I to IV, but also to use it as an example of how large numbers of data sets can be presented and compared. With the broad range of length scales measured (USAXS, SAXS and WAXS), conventional presentation of the scattering data as intensity versus momentum transfer becomes hard to visualize and compare for a large number of data sets. To address this, I presented the data as fingerprint plots of two-dimensional colour maps where the intensity,  $I$ , and the gradient of intensity,  $d(\ln(I))/d(\ln(Q))$ , are represented by pixel colours on a logarithmic scale (Figure 31 & 32). In this representation, in addition to the axis of  $Q$ , one axis could be used for the different samples.

For reliable presentation of the results in the colour map representation, some criteria regarding the binning of data in  $Q$  space and in the calculation of gradients are necessary. For the plots of intensity, the approach was to normalise the values to the highest and lowest values for each sample. This was done for uniformity between samples, however, this process could be adjusted depending on the purpose of the comparison. For some purposes it might be more efficient to normalise the values to high and low values across a range of samples.

Logarithmic binning in  $Q$  is used with sufficiently large steps to maintain a good signal-to-noise ratio. In the representations of gradients (Figure 32), this was taken as linear interpolations to the chosen points in  $Q$ , however, the protocol could easily be adjusted based on mathematical criteria to optimize display of information while minimizing noise. The colours were chosen as the modulus of the gradient that could have lower and upper limits depending on the low and high gradient of the individual sample, in a particular range of  $Q$ , or as the maximum and minimum gradients for a set of data.

Essentially, all information is preserved in this format, and characteristic features such as peaks and scaling of intensity is seen over a full  $Q$  range. An important advantage of this approach is how easy it is to see similarities and differences between samples, rather than using it to fit absolute model parameters. The representation is a complement to existing representations when data volumes are large and a visual overview is useful for initial interpretation

and sample comparison. It is particularly useful for complex systems such as these types of food materials that contain many different components and where direct model fitting is a challenge. The structural features are often broad and distributed over a range of  $Q$  rather than showing sharp peaks. Instead of comparing values of intensities directly in diffuse peaks or as parameters in model fits, this representation allows for intercomparison between samples in a more general approach.

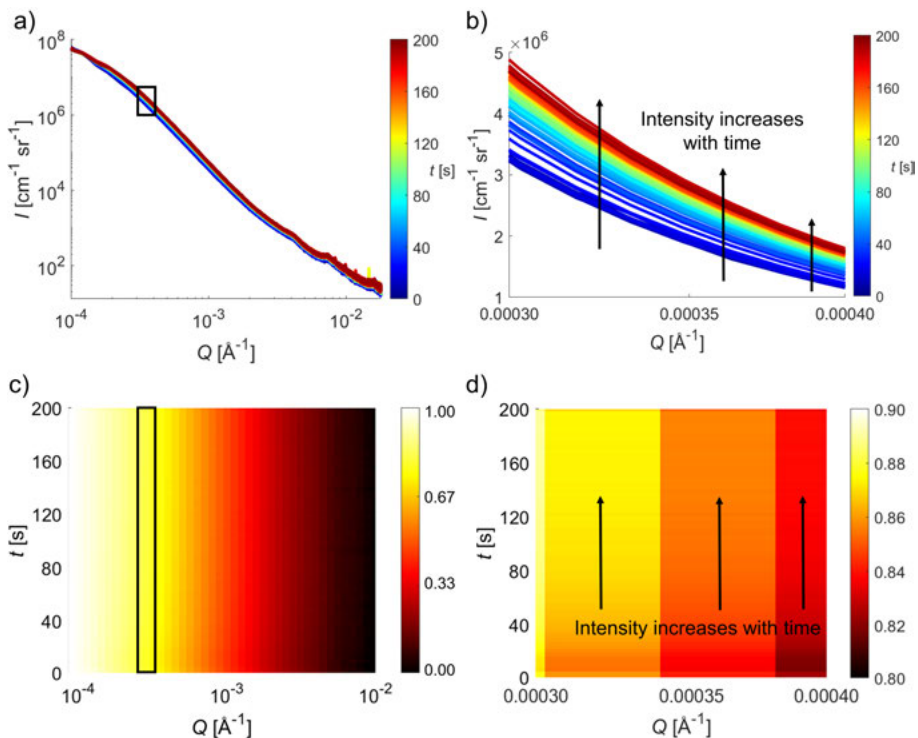


Figure 31. a) SAXS pattern of an emulsion with 60% v/v oil and 7.5% w/v protein measured at ESRF at a constant applied shear rate of  $1000 \text{ s}^{-1}$ . The colour scale from blue to red represents the time from start to end of measurement after 200 s. b) Zoomed in region of a) at  $0.0003 \leq Q \leq 0.0004 \text{ \AA}^{-1}$  with a linear scale in intensity. The intensity is clearly observed to increase with time. c) Colour map representation of intensity of the same data as in a). The intensity is normalized to the highest and lowest values over the entire  $Q$  range and given on a colour scale from black to red to white. d) Colour map representation of the same data and with the same  $Q$  range as in b). Also in this representation, the increase in intensity with time is clearly visible by the shift in colour.

In addition to helping in visual human interpretation, this format of data representation could have potential for more automated analysis of large data sets with artificial intelligence. Particularly with the enormous amounts of data that can easily be collected at large-scale facilities, it is necessary to introduce

such methods for optimal efficiency. For example, the rheo-SAXS experiments performed at ESRF during 2 days of beam time, only partly presented in paper V, produced data of the order Terabytes. An example of how the increase in intensity with time at a constant applied shear rate can be seen in normal representation and in this colour plot representation in Figure 31.

Both intensity and gradients of how the intensity varies with momentum transfer are presented in paper V. Combining the observations from these colour maps of intensity and gradients of intensity, provides a lot of information relevant to material structure at different length scales. An example of how the representation of gradient can be used for the SANS study of emulsions at various temperatures (section 5.4) is presented in Figure 32.

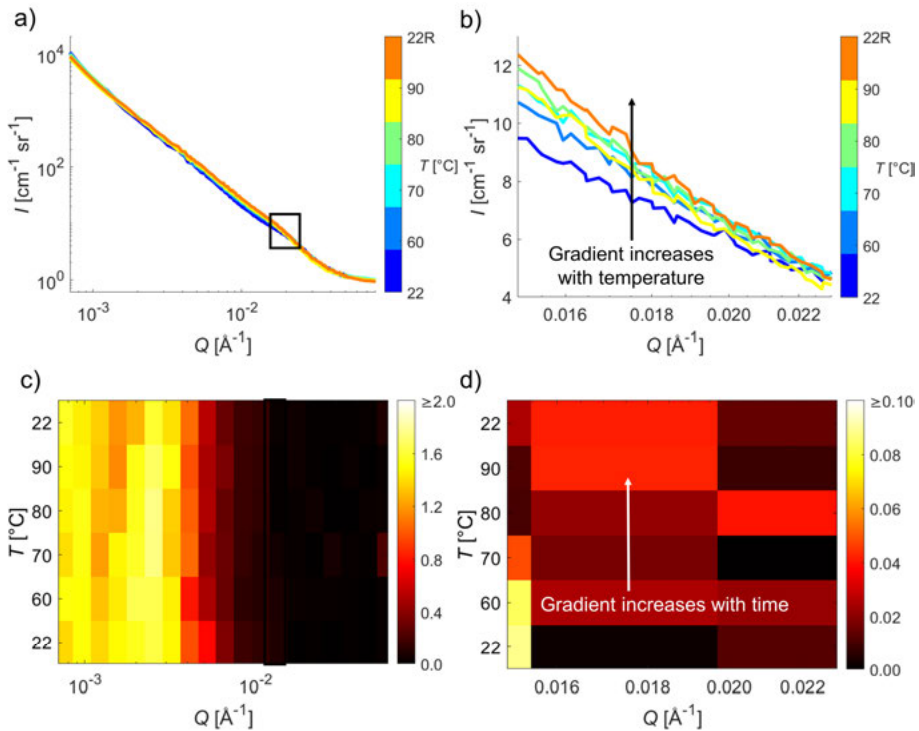


Figure 32. a) SANS pattern of an emulsion with 50% v/v oil and 10% w/v protein at different temperatures measured at ANSTO. The colour scale from blue to orange represents the temperature from 22 °C to 90 °C and back to 22 °C (22R). b) Zoomed in region of the graph in a) at  $0.015 \leq Q \leq 0.025 \text{ \AA}^{-1}$  with a linear scale in intensity. The intensity is clearly observed to increase with temperature and the process is irreversible. c) Colour map representation of gradient of the same data as in a). The gradient is given on a colour scale from black to red to white. d) Colour map representation of the same data and with the same  $Q$  range as in b). Also in this representation is the increase in gradient clearly visible with temperature, particularly the shift in gradient between 22 °C and 60 °C.

The colour map representation should be viewed as a complement to conventional scattering analysis. Instead of replacing model-based interpretations, it provides an easier way to organize and compare large volumes of data that are not easily represented by simple models. This representation could be viewed as a way of bridging a gap between the food science community and scattering experts. For people not as acquainted to interpret scattering patterns, this is a route to open this type of experimental techniques and communicate results to a broader audience. Clear and accessible communication of scientific results is essential for both ensuring reproducibility, but also for collaboration between disciplines and for progressing science in a transparent way.

## 9. Summary and conclusions in one paragraph

The main finding from this dissertation regarding protein stabilized emulsions, and with pea proteins specifically, is the dual role of the proteins both as adsorbed to oil-water interfaces as in classical emulsions, and as structuring agents in the continuous phase. The excellent stability, both thermally and with different pH, arises as a combination of interfacial coverage and protein interactions in the continuous phase leading to network formation. The protein both increases viscosity and hinders creaming and coalescence of droplets. The properties of the pea protein stabilized emulsions are dependent on both oil concentration, protein concentration, pH, applied shear and temperature. Table 2 summarizes how the droplet size is affected by these factors.

Table 2. Summary of effects on droplet size in pea protein stabilized emulsions. Droplet size decreases with increasing pH, shear rate, protein concentration and oil concentration, while temperature shows no clear effects. The range is taken over the stable emulsions that have been investigated in this work.

<b>Variable</b>	<b>Range</b>	<b>Effect on droplet size</b>
Protein [% w/v]	5 → 15	Decreases with higher content
Oil [% v/v]	10 → 60	Decreases with higher content
pH	3 → 7	Decreases with higher pH
Temperature [°C]	4 → 90	No change
Shear [ $s^{-1}$ ]	0 → 1000	Decreases with higher shear

## 10. Populärvetenskaplig sammanfattning

Har du någonsin funderat på hur det går till när läkemedel frisätter sina aktiva ämnen på ett långsamt och kontrollerat sätt i kroppen? Eller på hur raketbränslen, smörjmedel, färger och andra avancerade ytbeläggningar fungerar även när de utsätts för extrema förhållanden som hög värme, högt tryck, eller kraftiga vibrationer. Och vad har egentligen dessa exempel på högteknologiska produkter gemensamt med maten i ditt kylskåp?

Skillnaderna mellan dessa användningsområden kan verka stora till en början, men faktum är att de egentligen är ganska lika ur ett vetenskapligt perspektiv eftersom de är gjorda av samma typ av material, nämligen **emulsioner**. Emulsioner är blandningar av material som egentligen inte vill blandas, det mest klassiska exemplet är olja och vatten. I dessa material är oljedroppar utspridda i en kontinuerlig vattenfas (den sammanhängande vätskan som omger oljedropparna). Eftersom vatten och olja naturligt separerar sig i två lager krävs det att man tillsätter ett tredje ämne, ett så kallat **emulgeringsmedel**, som fäster vid gränssytan mellan oljedropparna och vattnet för att de ska blanda sig.

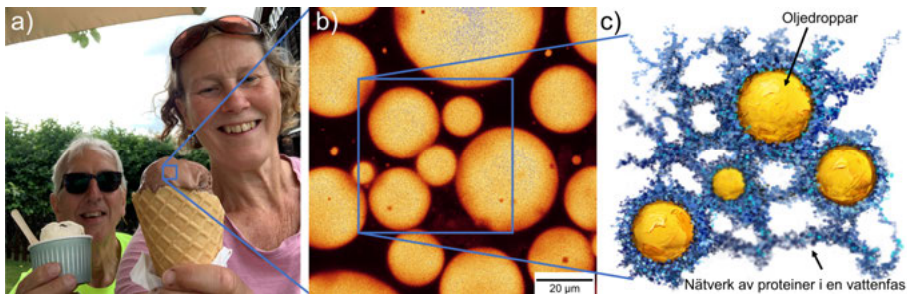


Figure 33. a) Glass är ett typiskt exempel på en emulsion inom livsmedel. b) Tittar man riktigt nära på en emulsion ser man oljedroppar som är omringade av en vattenfas. Det kan man till exempel se genom att använda ett mikroskop. c) En schematisk representation av hur ärtproteiner stabiliserar emulsioner genom att både binda till oljedropparna samt även att bilda ett nätverk i den omgivande vattenfasen.

Emulsioner används inom olika industriella sektorer, allt från läkemedelsutveckling och kosmetika till flyg- och rymdteknik, energisystem och livsmedel. Mjölk, majonnäs, glass (Figure 33a), salladsdressingar och choklad är några exempel på livsmedel som innehåller både olja och vatten. Den här

avhandlingen undersöker **ärtprotein** som ett växtbaserat alternativ till ägg- och mjölkbaserade proteiner som emulgeringsmedel inom livsmedelsapplikationer. I Figure 33b kan man se en mikroskopbild av en stabil emulsion där oljedroppar är omgivna av en vattenfas.

Ärtproteiner är, i likhet med många andra växtbaserade material, en komplex blandning av olika typer av proteiner med olika egenskaper. Några av dessa proteiner fäster vid oljedropparna liksom klassiska emulgeringsmedel, medan resten sprids ut i den omgivande vattenfasen. Arbetet i den här avhandlingen visar att det här "överskottsprotein" i vattenfasen är avgörande för att öka emulsionernas stabilitet.

Emulsionerna som har undersökts i det här arbetet innehåller oljedroppar som är några mikrometer, medan proteinstrukturerna sträcker sig på en skala från nanometer upp till klumpar som är flera mikrometer. Som jämförelse kan man tillägga att dessa är åtminstone tio gånger mindre än tjockleken på ett mänskligt hårstrå. För att kunna studera så pass små strukturer krävs avancerade metoder. Tekniker som används i detta arbete är exempelvis reologi, som beskriver hur material flyter och ändrar form, röntgen- och neutronstrålning, som undersöker materialstrukturer (Figure 34), samt avancerade mikroskop, där droppar och proteiner avbildas direkt. Resultaten från dessa har sammantagits till slutsatser om dropparnas och proteinernas rörelse, storlek, form och placering. En av fördelarna med valet av just dessa tekniker är att flera olika storlekar av objekt har kunnat undersökas parallellt. Stabiliteten i dessa emulsioner kan således sammanfattas av två mekanismer:

- Proteinerna som fäster till oljedropparnas yta bildar ett **skyddande lager** som **hindrar att dropparna flyter ihop**
- Resten av proteinet, som befinner sig i vattenfasen, binder till varandra och bildar ett **nätverk** som **hindrar att dropparna rör på sig**

Det här betyder att ärtproteinerna inte bara omringar enskilda droppar, utan även bygger upp en övergripande struktur i emulsionen, liksom ett skelett, som man kan se i den schematiska representationen i Figure 33c. Nätverkets egenskaper och funktion beror på yttre faktorer såsom de relativa mängderna av olja, vatten och protein, pH (surhet), temperatur och hur kraftigt emulsionen rörs om (skjuvning).

När det kommer till livsmedel är dessa faktorer direkt kopplade till praktiska moment som val av ingredienser/recept, mekanisk blandning, tillagning/upphettning, och tuggning/konsumtion. Ingrediensvalet påverkar både sammansättningen och surheten. Blandning ger upphov till mekanisk påverkan. Upphettning ökar temperaturen, och tuggning innebär ytterligare förändring av temperaturen och mekanisk påverkan. Emulsionerna som har undersökts i den här avhandlingen visar en god stabilitet över ett brett spann av yttre

förhållanden, med viss förändring av droppstorleken. Generellt sett ger mindre droppar en stabilare emulsion. För de studerade emulsionerna leder högre koncentrationer av protein och olja till att systemet blir mer trögflytande (högre viskositet), vilket leder till att dropparna håller sig mindre eftersom de inte flyter ihop lika lätt. Lågt pH-värde påverkar proteinernas struktur och leder till större oljedroppar. Temperaturen har inte så mycket effekt på droppstorleken, medan kraftig omrörning leder till att droppar splittras och blir mindre.



Figure 34. Schematisk representation av hur röntgenstrålning kan användas för att studera emulsioner och andra material. En röntgenstråle riktas mot provet och när fotonerna kommer i kontakt med materialet ändras riktningen som de färdas. Genom att mäta var de träffar på en detektor, det vill säga hur mycket de sprids, kan man räkna ut t.ex. storleken och vilken form som dropparna har i en emulsion.

Även om ärtprotein är huvudfokuset i den här avhandlingen, inkluderar arbetet även andra liknande material från plantbaserade råvaror. Emulgeringsmedel baserade på mandel, kokos, bondböna, linfrö, havre, ris, soja, och även mejeriprodukter har undersökts. I avhandlingen presenteras strukturella ”fingeravtryck” av dessa som ett nytt sätt att visualisera och jämföra röntgendata från många prover samtidigt. Den här metoden är inte begränsad till livsmedel, utan kan användas inom andra områden där struktur är viktigt och kanske främst för att jämföra olika sammansättningar eller typer av material.

Inom läkemedel används emulsioner till att långsamt och kontrollerat frisätta aktiva substanser genom att emulsionen destabiliseras när pH och temperatur ändras eller över tid. Inom till exempel flyg- och rymdteknik, smörjmedel, färger och beläggningar är det tvärtom, där måste materialen vara stabila även under extrema förhållanden. Emulsionernas värld är mycket större än vad man kan tro, och det är användningsområdet som styr vilka egenskaper som är önskvärda och hur de ska stabiliseras eller reagera på förändringar i omgivningen.

Min forskning bidrar specifikt till att besvara frågor som 'Vad är det som gör att mejeribaserade livsmedel upplevs som krämiga, visuellt tilltalande och med bra struktur?' och 'Hur kan vi återskapa dessa egenskaper med andra (växtbaserade) alternativ?'. Så nästa gång som du njuter av en perfekt krämig glass som bara smälter i munnen på en varm sommardag kan du tänka på att det ligger en hel del vetenskap bakom. Och kanske, om du har tur, så märker du inte ens att den är gjord av ärtprotein eller andra växtbaserade råvaror.

## 11. Popular scientific summary

How do medicines release their active ingredients in a controlled and even rate? How can rocket fuels, lubricants, paints or coatings keep their functionality under extreme conditions such as high heat, pressure and vibrations? And what do these high-tech products have in common with the everyday foods in your kitchen?

Although the first impression is a clear difference between these applications, they share one scientific challenge. The challenge is how to keep oil and water (or other immiscible ingredients) mixed in a stable way. Such mixtures, known as **emulsions**, are used in applications ranging from drug delivery, cosmetics, aerospace, energy systems and foods. Milk, mayonnaise, ice cream (Figure 35a), dressings and chocolate are some examples of food emulsions, where droplets of oil are dispersed in an aqueous continuous phase (water). With the addition of **emulsifiers**, i.e., molecules or particles, adsorbing to the interface between oil droplets and the surrounding water, emulsions can be kept stable for long times. This dissertation focuses on **pea protein** as a plant-based emulsifier to replace conventional egg or dairy derived ingredients to stabilize emulsions for food applications. A microscope image of a stable emulsion where oil droplets are dispersed in an aqueous phase is seen in Figure 35b.

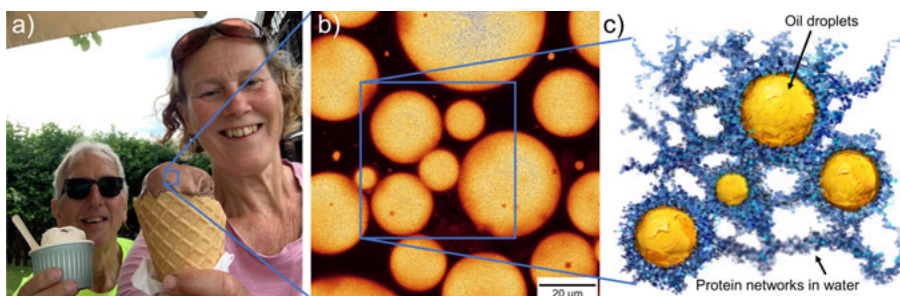


Figure 35. a) Ice-cream is a well-known example of a food type emulsion. b) A closer look of an emulsion shows oil droplet dispersed within an aqueous water phase. This can for example be seen with microscopes. c) A schematic representation of how pea protein stabilizes emulsions by attaching to the oil-water interface and creating a network in the aqueous phase.

Pea proteins, similarly to many other plant-based materials, are a complex mixture of proteins that have different properties, that can interact, and that behave in different ways. Some fraction of the proteins attach to the oil droplets like conventional emulsifiers, however, some are located in the surrounding water. The work presented in this dissertation describes how this “extra” protein in the continuous phase is used to improve emulsion stability.

The oil droplets in these systems are a few micrometres in size, and the protein structures ranges from nanometres up to aggregates of several micrometres. For reference, these structures are at least an order of magnitude smaller than the thickness of a piece of human hair. To “see” structures of this size requires advanced techniques. Methods used in this work is for example rheology which describes how a material flows and deforms, small angle X-ray and neutron scattering that investigates material structures (Figure 36), and confocal microscopy that can image proteins and droplets directly. These have been used to understand the behaviour, size, shape and location of the proteins and oil droplets inside the emulsions. A powerful thing with this work is the study of the components on several length scales to obtain not only a picture of individual protein behaviour or droplet size but how they are related.

The stability of these emulsion systems can be described as a combination of two different mechanisms:

- Proteins attach to the oil droplet surface and create a **protective layer** that **prevents droplet coalescence**
- Excess proteins connect to each other, forming a **network** in the surrounding water that **prevents motion of droplets**

That means that the pea proteins do not only cover individual droplets, but also build a supporting network within the emulsion as shown schematically in Figure 35c. The structure of this network depends on factors such as the relative fractions of individual components of oil, water and protein, pH (acidity), temperature and shear.

Examples of where this is relevant for foods are in the ingredient selection (recipe), mixing, cooking and chewing/consumption processes. The choice of ingredients affects both the composition and pH. The mixing causes shear. The cooking gives a raise in temperature and the chewing causes additional shear and temperature increase. The system studied in this dissertation showed stability over a range of conditions and treatments, with some change in droplet size. In general, smaller droplets, mean a more stable system. A higher concentration of proteins and oil produces smaller droplets due to a higher viscosity. A lower pH changes the conformation of the proteins and increases the droplet size. The temperature has limited effect on droplet size and stability and high shear causes breakage of droplets.

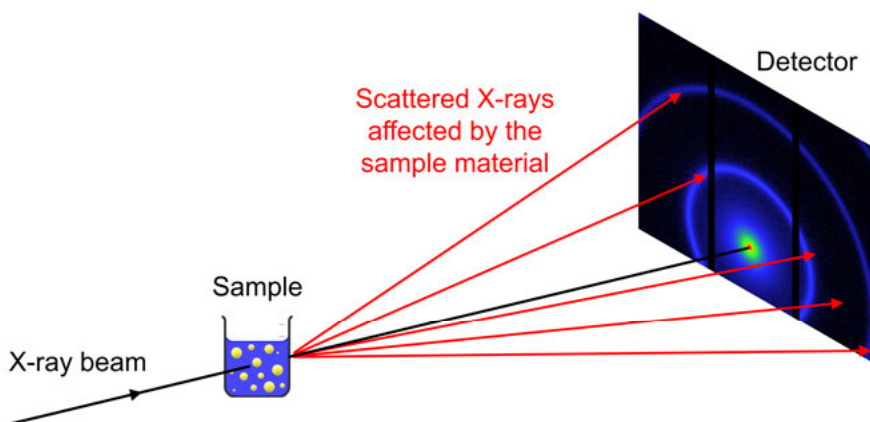


Figure 36. Schematic representation of how X-ray scattering can be used to study emulsions and other materials. A beam of X-rays hit the sample, and change direction upon contact with the sample. By recording the intensity on a detector of how much they scatter, it is possible to calculate for example the size and shape of the oil droplets in an emulsion.

While proteins from peas are the main material investigated, the scope in this dissertation goes beyond this specie. I compare emulsions based on almond, coconut, fava bean, linseed, oat, rice, soy and even dairy materials. The work identifies structural “fingerprints” of each material and proposes a new way of presenting results obtained from scattering experiments. This method is relevant not only for food applications but also for other industrial areas where the material structure is important, particularly in the comparison of different formulations or between different types of materials.

Medicines release their active ingredients by a slow process of emulsion destabilization where the encapsulated active ingredients get released. Rocket fuels, lubricants, paints and coatings are formulated to remain stable and retain their structure at extreme conditions such as high temperatures and under shear. In the first case, destabilization is crucial upon change in pH, temperature or with time, but in the other cases, materials need to remain both thermally and long-term stable. The world of emulsions is greater than you first may think and it is the application that will determine the desired properties and response to external factors.

This research helps to answer questions such as 'What makes the (dairy-based) food that we appreciate in terms of creaminess, visual appearance and texture be that way?' and 'How do we recreate the same properties with other (plant-based) materials?'. The next time that you enjoy a smooth, perfect, melting-in-the-mouth ice-cream on a hot summer day, you should remember that a lot of science has been involved in this formulation and if you are lucky, you will perhaps not even notice that it is made with pea proteins or other plant-based materials.

## 12. Acknowledgements

I would like to thank the people that in various ways have contributed both to me on a personal level and more directly to the scientific work during these last four years in my life as a PhD student.

I first want to thank my supervisor **Adrian Rennie** for guiding me on this journey from the beginning to the end, for your availability, your stories from a remarkably long time devoted to research, your lunch time running related talks and for your deep scientific discussions throughout my PhD time. I will never meet someone with such deep scientific knowledge and I am grateful to have had you as my mentor, supervisor and friend. You have contributed not only to improve my scientific writing, chemistry knowledge, presentation strategies but also to my personal growth, and interest in and curiosity to research. I will always remember the smallest things such as the double space after punctuation, the non-italics of Greek letters in equations and the correct use of minus signs in my texts. I am very grateful to have had you as my supervisor.

I am grateful for the funding and beamtime facilities that made this project possible. I specifically thank the beamline scientists **Joachim Kohlbrecher** at PSI, **Theyencheri Narayanan** and **Gouranga Manna** at ESRF, **Wim Bouwman**, **Chris Duif**, **Jeroen Plomp**, **Coen Fransen** and **Michel Thijs** at TUD, and **Jitendra Mata** at ANSTO. A special thanks to **Johan Gråsjö** and **Per Hansson** for support and access to the USAXS/SAXS instrument in Uppsala. Thank you, Johan, for everything that you have shown me in the SAXS lab and our scientific discussions about the USAXS resolution and beam divergence.

I acknowledge PICKFOOD for funding this project. The people within this network that have been collaborators and co-authors during this time include **Rini Padinjakkara Ravindranathan**, **Bruno Telli Ceccato**, **Matti Knaapila**, **Jon-Otto Fossum**, **Kenneth Knudsen**, **Daniel Bonn** and **Panlin Jin**. Special thanks to Daniel and his group for a warm and welcoming environment during my secondment at UvA in Amsterdam that gave the inspiration for the title of this dissertation. Thank you to Matti and Jon-Otto for the hospitality during my secondment at NTNU in Trondheim. I also thank the

Macromolecular Chemistry Group at Uppsala University for providing a good research environment. Thank you **Njelama Sanga**, **Shima Tavakoli**, **Hamidreza Mokhtari**, **Adriana Saldivar**, **Patrick Shakari**, **Norein Norein**, **Christos Leliopoulos**, **Rohith Pavan Parvathaneni**, **Anjali Vijayan**, **Oommen Varghese**, **Valentina Guccini** and **Jöns Hilborn**. Thank you also to my co-supervisor **Tim Melander Bowden**. It has been a pleasure to work with all of you, both to hear about your research and to have the fika gatherings, Monday meetings and the journal club.

Some people involved in the measurements included in this dissertation and in the learning to operate new instruments include **Patrick Shakari** with the DSC, **Christos Leliopoulos** with the TGA, and **Marie Corpart**, **Paul Kolpakov** and **Elham Mirzahosseini** with the rheology and confocal microscopy. I thank **Lars Ahlberg** for the design (with help from **Johan Ahlberg** and **Pontus Ahlberg**) of the image on the front cover.

Thank you to all teachers and mentors during my education at University of New Hampshire, Mora Gymnasium, Engelbrektskolan and Ekebyskolan, that encouraged my interest in research and science. The gratefulness goes further to the training coaches and teammates over the years that have contributed to my life and personal growth also outside of work.

The most important thank you goes to my family – my parents **Lena** and **Carl Olsmats**, my sister **Caroline Olsmats**, my grandparents **Anette** and **Bengt Wallman** and all other family. You are my inspiration and my steady place. Thank you for encouraging me to grow and for shaping me to the person that I am today. Thank you, dad, for paving the way with your career in academia. Thank you to my grandfather, **Mats Olsmats**, who spent his life at Uppsala University. You would have been proud of this. Thank you everyone. I could not have done this without your support.

Last but not least, I thank **Johan Ahlberg**, my fiancé, that I met early in my PhD. Thank you for being my best friend, my running bestie, my adventure partner and for your support and many discussions along the way. I apologize for the too detailed explanations of how pea protein stabilizes emulsions, for my complaints about delayed reviewer comments, and for my scientific commitment sometimes after normal working hours. It would not have been the same without you and I am forever grateful for your support, positive engagement and love.

And finally, thank you to everyone who has taken the time to read about the work in my dissertation.

# References

- [1] Bureau International de Poids Mesures (2019). *The International System of Units (SI)*. 9th ed.
- [2] Tadros, T. F. (ed.) (2013). *Emulsion Formation and Stability*. Wiley-VCH Verlag GmbH & Co. KGaA.
- [3] Clark, C. (2012). *The Science of Ice Cream*. 3rd ed. Royal Society of Chemistry.
- [4] Leal-Calderon, F., Bibette, J. & Schmitt, V. (eds.) (2007). *Emulsion Science: Basic Principles*. 2nd ed. Springer.
- [5] McClements, D. J. (2015). *Food Emulsions: Principles, Practices, and Techniques*. 3rd ed. CRC Press.
- [6] zhang, M., Fan, L., Liu, Y., Huang, S. & Li, J. (2022). Effects of proteins on emulsion stability: The role of proteins at the oil-water interface. *Food Chemistry*, 397:133726.
- [7] McClements, D. J. (2004). Protein-stabilized emulsions. *Current Opinion in Colloid & Interface Science*, 9(5):305–313.
- [8] McClements, D. J., Bai, L. & Chung, C. (2017). Recent Advances in the Utilization of Natural Emulsifiers to Form and Stabilize Emulsions. *Annual Review of Food Science and Technology*, 8:205–236.
- [9] Shao, P., Feng, J., Sun, P., Xiang, N., Lu, B. & Qiu, D. (2020). Recent advances in improving stability of food emulsion by plant polysaccharides. *Food Research International*, 137:109376.
- [10] Pickering, S. U. (1907). Emulsions. *Journal of the Chemical Society, Transactions*, 91:2001–2021.
- [11] Ramsden, W. (1904). Separation of solids in the surface-layers of solutions and ‘suspensions’ (observations on surface-membranes, bubbles, emulsions, and mechanical coagulation). - Preliminary Account. *Proceedings of the Royal Society of London*, 72(477-486):156–164.
- [12] Binks, B. P. (2002). Particles as surfactants - similarities and differences. *Current Opinion in Colloid & Interface Science*, 7(1–2):21–41.
- [13] Dickinson, E. (2012). Emulsion gels: The structuring of soft solids with protein-stabilized oil droplets. *Food Hydrocolloids*, 28(1):224–241.
- [14] Burger, T. G. & Zhang, Y. (2019). Recent progress in the utilization of pea protein as an emulsifier for food applications. *Trends in Food Science & Technology*, 86:25–33.
- [15] Ge, J., Sun, C. X., Corke, H., Gul, K., Gan, R. Y. & Fang, Y. (2020). The health benefits, functional properties, modifications, and applications of pea (*Pisum sativum* L.) protein: Current status, challenges, and

- perspectives. *Comprehensive Reviews in Food Science and Food Safety*, 19:1835–1876.
- [16] Zaccai, N. R., Serdyuk, I. N. & Zaccai, J. (2017). *Methods in Molecular Biophysics Structure, Dynamics, Function for Biology and Medicine*. 2nd ed. Cambridge University Press.
- [17] Olsmats, E. & Rennie, A. R. (2024). Pea protein [*Pisum sativum*] as stabilizer for oil/water emulsions. *Advances in Colloid and Interface Science*, 326:103123.
- [18] Superfruit Scandinavia AB. Pea protein. EAN 7350039931268.
- [19] Campbell, M. K. (1991). *Biochemistry*. 3rd ed. Saunders College Publishing.
- [20] Tanger, C., Engel, J. & Kulozik, U. (2020). Influence of extraction conditions on the conformational alteration of pea protein extracted from pea flour. *Food Hydrocolloids*, 107:105949.
- [21] Yang, J., Zamani, S., Liang, L. & Chen, L. (2021). Extraction methods significantly impact pea protein composition, structure and gelling properties. *Food Hydrocolloids*, 117:106678.
- [22] Pelgrom, P. J., Vissers, A. M., Boom, R. M. & Schutyser, M. A. (2013). Dry fractionation for production of functional pea protein concentrates. *Food Research International*, 53(1):232–239.
- [23] Chu, C. C., Neo, Y. P., Teng, S. K. & Chew, S. C. (2025). Nutritional insights into rapeseed oil: biochemical composition, refining process and health implications. *Food Science and Biotechnology*. (Accepted) doi: 10.1007/s10068-025-02027-2
- [24] Ellegård, L., Andersson, H. & Bosaeus, I. (2005). Rapeseed oil, olive oil, plant sterols, and cholesterol metabolism: an ileostomy study. *European Journal of Clinical Nutrition*, 59(12):1374–1378.
- [25] Gomori, G. (1955). Preparation of Buffers for Use in Enzyme Studies. *Methods in Enzymology*, 1:138–146.
- [26] Schmitz, K. S. (1990). *An Introduction to Dynamic Light Scattering by Macromolecules*. Academic Press, Inc.
- [27] Brown, W. (ed.) (1993). *Dynamic Light Scattering: The method and some applications*. Oxford University Press.
- [28] Einstein, A. (1905). Über die von der molekularkinetischen Theorie der Wärme geforderte Bewegung von in ruhenden Flüssigkeiten suspendierten Teilchen. *Annalen der Physik*, 322(8):549–560.
- [29] Koňák, Č., Jakeš, J., Štěpánek, P., Petráš, F., Kárská, M., Křepelka, J. and Peřina, J. (1991). Effect of multiple light scattering on transmitted and scattered light. *Applied Optics*, 30(33):4865–4871.
- [30] Maret, G. & Wolf, P. E. (1989). Multiple Light Scattering: Weak Localization and Dynamic Fluctuations. *Physica Scripta*, 1989:223–225.
- [31] International Organization for Standardization (2017). *Particle size analysis - Dynamic light scattering (DLS) (ISO 22412:2025)*.
- [32] Formulation. (2023). *Turbiscan Stability Index (TSI)*. <https://formulation.com/solutions/turbiscan-stability-index-tsi/> (Accessed 2023-10-20).

- [33] Sutton, M. (2008). A review of X-ray intensity fluctuation spectroscopy. *Comptes Rendus Physique*, 9(5–6):657–667.
- [34] Livet, F. (2007). Diffraction with a coherent X-ray beam: dynamics and imaging. *Acta Crystallographica A*, 63(2):87–107.
- [35] Zinn, T., Narayanan, T., Kottapalli, S. N., Sachs, J., Sottmann, T. and Fischer, P. (2022). Emergent dynamics of light-induced active colloids probed by XPCS. *New Journal of Physics*, 24:093007.
- [36] Bouchaud, J.-P. (2008). Anomalous relaxation in complex systems: from stretched to compressed exponentials. In Klages, R., Radons, G. & Sokolov, I. M. (eds.). *Anomalous Transport: Foundations and Applications*. Wiley, pp. 327–345.
- [37] Zinn, T., Homs, A., Sharpnack, L., Tinti, G., Fröjdh, E., Douissard, P.-A., Kocsis, M., Möller, J., Chushkin, Y. & Narayanan, T. (2018). Ultra-small-angle X-ray photon correlation spectroscopy using the Eiger detector. *Journal of Synchrotron Radiation*, 25(6):1753–1759.
- [38] Delgado, A., González-Caballero, F., Hunter, R., Koopal, L. & Lyklema, J. (2007). Measurement and interpretation of electrokinetic phenomena. *Journal of Colloid and Interface Science*, 309(2):194–224.
- [39] Hunter, R. J. (1981). *Zeta Potential in Colloid Science: Principles and Applications*. Academic Press.
- [40] Sheppard, C. J. R. & Wilson, T. (1981). The theory of the direct-view confocal microscope. *Journal of Microscopy*, 124(2):107–117.
- [41] Greenspan, P., Mayer, E. P. & Fowler, S. D. (1985). Nile red: a selective fluorescent stain for intracellular lipid droplets. *The Journal of Cell Biology*, 100(3):965–973.
- [42] Kim, J. & Lee, M. (1999). Excited-State Photophysics and Dynamics of a Hemicyanine Dye in AOT Reverse Micelles. *The Journal of Physical Chemistry A*, 103(18):3378–3382.
- [43] Velandia, S. F., Bittermann, M. R., Mirzahassein, E., Giubertoni, G., Caporaletti, F., Sadtler, V., Marchal, P., Roques-Carmes, T., Meinders, M. B. J. & Bonn, D. (2023). Probing interfaces of pea protein-stabilized emulsions with a fluorescent molecular rotor. *Frontiers in Soft Matter*, 3:1093168.
- [44] Jacrot, B. (1976). The study of biological structures by neutron scattering from solution. *Reports on Progress in Physics*, 39(10):911–953.
- [45] Henke, B., Gullikson, E. & Davis, J. (1993). X-ray Interactions: Photoabsorption, Scattering, Transmission, and Reflection at  $E = 50\text{--}30,000$  eV,  $Z = 1\text{--}92$ . *Atomic Data and Nuclear Data Tables*, 54(2):181–342.
- [46] Sears, V. F. (1992). Neutron scattering lengths and cross sections. *Neutron News*, 3(3):26–37.
- [47] Glatter, O. & Kratky, O. (eds.) (1982). *Small Angle X-ray Scattering*. Academic Press Inc. Ltd.
- [48] Svergun, D. I., Koch, M. H. J., Timmins, P. A. & May, R. P. (2013). *Small Angle X-Ray and Neutron Scattering from Solutions of Biological Macromolecules*. Oxford University Press.

- [49] Bonse, U. & Hart, M. (1966). Small Angle X-Ray Scattering by Spherical Particles of Polystyrene and Polyvinyltoluene. *Zeitschrift für Physik*, 189:151–162.
- [50] Ilavsky, J., Zhang, F., Levine, L., Allen, A., Jemian, P. & Long, G. (2013). Ultra-Small-Angle X-ray Scattering Instrument at the Advanced Photon Source: History, Recent Development, and Current Status. *Metallurgical and Materials Transactions A*, 44:68–76.
- [51] Bouwman, W. G. (2021). Spin-echo small-angle neutron scattering for multiscale structure analysis of food materials. *Food Structure*, 30:100235.
- [52] Rekveldt, M. T., Plomp, J., Bouwman, W. G., Kraan, W. H., Grigoriev, S. & Blaauw, M. (2005). Spin-echo small angle neutron scattering in Delft. *Review of Scientific Instruments*, 76:033901.
- [53] Narayanan, T. (2008). Synchrotron Small-Angle X-Ray Scattering. In Borsali, R. & Pecora, R. (eds.). *Soft Matter Characterization*. Springer, pp. 899–952.
- [54] Schmidt, P. (1995). Some fundamental concepts and techniques useful in small-angle scattering studies of disordered solids. In Brumberger, H. (ed.). *Modern Aspects of Small-Angle Scattering*. Springer, pp. 1–56.
- [55] Guinier, A. & Fournet, G. (1955). *Small-Angle Scattering of X-Rays*. John Wiley and Sons, Inc.
- [56] Teixeira, J. (1988). Small-angle scattering by fractal systems. *Journal of Applied Crystallography*, 21:781–785.
- [57] Gravatt, C. C. & Brady, G. W. (1969). Slit Smearing Effects in the Bonse-Hart Small-Angle X-ray Diffractometer. *Journal of Applied Crystallography*, 2:289–295.
- [58] Schmidt, P. W. & Hight Jr, R. (1960). Slit Height Corrections in Small Angle X-ray Scattering. *Acta Crystallography*, 13:480–483.
- [59] Lake, J. A. (1967). An Iterative Method of Slit-Correcting Small Angle X-ray Data. *Acta Crystallographica*, 23:191–194.
- [60] Pauw, B. R., Smith, A. J., Snow, T., Shebanova, O., Sutter, J. P., Ilavsky, J., Hermida-Merino, D., Smales, G. J., Terrill, N. J., Thünemann, A. F. & Bras, W. (2021). Extending synchrotron SAXS instrument ranges through addition of a portable, inexpensive USAXS module with vertical rotation axes. *Journal of Synchrotron Radiation*, 28(3):824–833.
- [61] Rehm, C., de Campo, L., Brûlé, A., Darmann, F., Bartsch, F. & Berry, A. (2018). Design and performance of the variable-wavelength Bonse-Hart ultra-small-angle neutron scattering diffractometer KOOKABURRA at ANSTO. *Journal of Applied Crystallography*, 51:1–8.
- [62] Narayanan, T., Sztucki, M., Zinn, T., Kieffer, J., Homs-Puron, A., Gorini, J., van Vaerenbergh, P. & Boesecke, P. (2022). Performance of the time-resolved ultra-small-angle X-ray scattering beamline with the Extremely Brilliant Source. *Journal of Applied Crystallography*, 55(1):98–111.

- [63] SasView. (2025). *SasView – Small Angle Scattering Analysis*. <http://www.sasview.org> (Accessed 2026-02-13).
- [64] Barnes, H. A., Hutton, J. F. & Walters, K. (1989). *An Introduction to Rheology*. Elsevier.
- [65] Owens, C. E., Fan, M. R., Hart, A. J. & McKinley, G. H. (2022). On Oreology, the fracture and flow of “milk's favorite cookie®”. *Physics of Fluids*, 34(4):043107.
- [66] Mewis, J. & Wagner, N. J. (2009). Thixotropy. *Advances in Colloid and Interface Science*, 147–148:214–227.
- [67] Panine, P., Gradzielski, M. & Narayanan, T. (2003). Combined rheometry and small-angle x-ray scattering. *Review of Scientific Instruments*, 74(4):2451–2455.
- [68] Wang, Y. & Ewoldt, R. H. (2023). Thixotropy, antithixotropy, and viscoelasticity in hysteresis. *Journal of Rheology*, 67(6):1199–1219.
- [69] Bonn, D., Denn, M. M., Berthier, L., Divoux, T. & Manneville, S. (2017). Yield stress materials in soft condensed matter. *Reviews of Modern Physics*, 89(3):035005.
- [70] Krieger, I. M. & Dougherty, T. J. (1959). A Mechanism for Non-Newtonian Flow in Suspensions of Rigid Spheres. *Transactions of The Society of Rheology*, 3(1):137–152.
- [71] Gaisford, S., Kett, V. & Haines, P. (eds.) (2016). *Principles of Thermal Analysis and Calorimetry*. The Royal Society of Chemistry.
- [72] Tsiptsias, C. (2022). On the latent limit of detection of thermogravimetric analysis. *Measurement*, 204:112136.
- [73] Guido, S., Simeone, M. & Greco, F. (2003). Deformation of a Newtonian drop in a viscoelastic matrix under steady shear flow: Experimental validation of slow flow theory. *Journal of Non-Newtonian Fluid Mechanics*, 114(1):65–82.
- [74] Guo, H., Song, K. & Hilfer, R. (2022). A Brief Review of Capillary Number and its Use in Capillary Desaturation Curves. *Transport in Porous Media*, 144:3–31.
- [75] Nettleton, J. A., Brouwer, I. A., Geleijnse, J. M. and Hornstra, G. (2017). Saturated Fat Consumption and Risk of Coronary Heart Disease and Ischemic Stroke: A Science Update. *Annals of Nutrition and Metabolism*, 70(1):26–33.
- [76] de Souza, R. J., Mente, A., Maroleanu, A., Cozma, A. I., Ha, V., Kishibe, T., Uleryk, E., Budyłowski, P., Schönemann, H., Beyene, J. and Anand, S. S. (2015). Intake of saturated and trans unsaturated fatty acids and risk of all cause mortality, cardiovascular disease, and type 2 diabetes: systematic review and meta-analysis of observational studies. *BMJ*, 351:h3978.

# Appendix A

The steps in the list below describe a general procedure to perform a SAXS measurement, including sample loading, physical instrument setup, measuring parameters, data reduction and data analysis.

## 1. Sample loading

- Determine holder based on the nature of the sample (gel, solid, liquid)
- Evacuate the sample chamber to vacuum

## 2. Sample alignment

- Move the sample holder horizontally and vertically to find the center of the sample and note the positions

## 3. Sample naming, description and data storage

- Define a directory for data storage, create a log file and make a list relating file number to sample and measurement conditions
- If there are multiple samples or different configurations, it is advisable to create a macro file with commands for a series of measurements that can run over long times

## 4. Detector configuration

- Choose the appropriate sample-to-detector distance based on the angles that are relevant to the length scales in the sample
- Determine the regions of interest on the detector
- Specify the detector position with appropriate offset from the centre

## 5. Collimation

- Constrain the beam size and divergence by specifying the slit dimensions

## 6. Measurement

- In addition to measurement of samples, it is highly recommended to always include extra measurements of:
  - Direct beam
  - Background (empty sample holder (Kapton window/capillary), solvent, oil...)

- Calibration reference sample for intensity such as glassy carbon
- Calibration reference sample for  $Q$  such as silver behenate

## 7. Data reduction

- Initial reductions based on for example instrument geometry and choice of region of interest as well as detector corrections
- Mask direct beam intensity, dead regions and noise on the two-dimensional images to evaluate scattering
- Perform an azimuthal average to convert the two-dimensional images to one-dimensional data. This is assuming that the scattering is isotropic
- Put the data on absolute scale by dividing by the direct beam intensity while allowing for the transmission of the sample, and divide by the sample thickness
- Subtract the appropriate background signal (e.g., sample holder, solvent, oil) scaled according to volume fraction, sample thickness and transmission
- If measurements have been performed at multiple sample-to-detector distances, the data sets can be merged over the common  $Q$  range
- Confirm that the intensity and values of  $Q$  are correct based on the measurements of reference samples

## 8. Data analysis

- Performed as either:
  - Model-free analysis of intensity and its gradient at different  $Q$
  - Arbitrary model fits with dimensionless or reduced parameters
  - Physical model fits with parameters describing real structural properties such as object size, shape and density
- More details about fitting and models used in this thesis are described in subsection 3.2.4 in the main text



# Acta Universitatis Upsaliensis

*Digital Comprehensive Summaries of Uppsala Dissertations from the Faculty of Science and Technology 2643*

Editor: The Dean of the Faculty of Science and Technology

A doctoral dissertation from the Faculty of Science and Technology, Uppsala University, is usually a summary of a number of papers. A few copies of the complete dissertation are kept at major Swedish research libraries, while the summary alone is distributed internationally through the series Digital Comprehensive Summaries of Uppsala Dissertations from the Faculty of Science and Technology. (Prior to January, 2005, the series was published under the title “Comprehensive Summaries of Uppsala Dissertations from the Faculty of Science and Technology”.)

